Paleo-hydrogeographical model for the Levant applying 3D supra-regional coastal groundwater modelling approach

Mohammed M. F. Alkurd

MSc Thesis Identifier number: WSE-GW.23.11
Student number: 1077526
August 2023

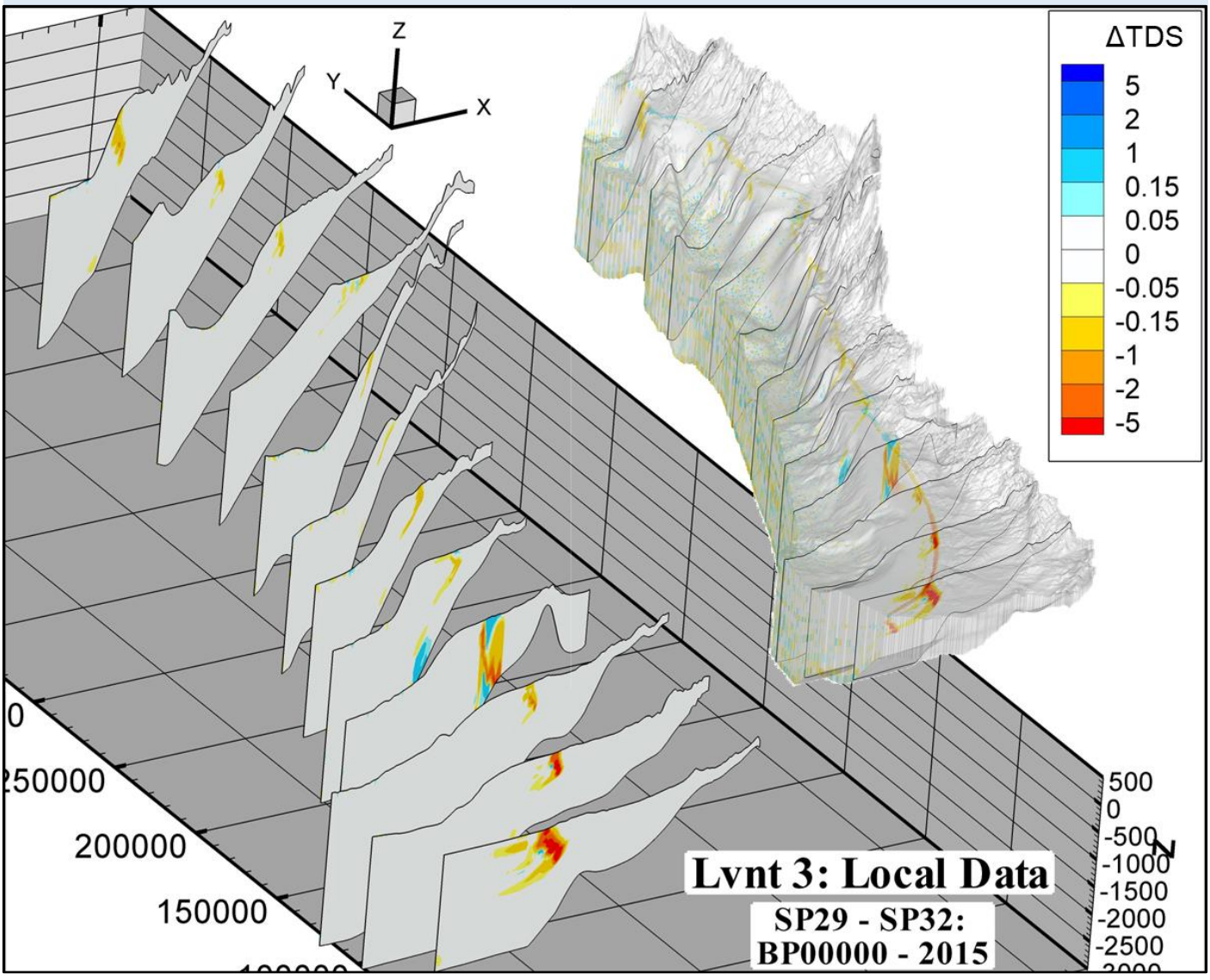

Paleo-hydrogeographical model for the Levant applying 3D supra-regional coastal groundwater modelling approach

Master of Science Thesis
by
Mohammed M. F. Alkurd

Supervisor
Andreja Jonoski

Mentors
Gualbert Oude Essink
Yangxiao Zhou

Examination committee
Chairman: Andreja Jonoski
External committee member: Theodorus Nicholaas Olsthoorn
Committee members:
Gualbert Oude Essink
Yangxiao Zhou

This research is done for the partial fulfilment of requirements for the Master of Science degree at the IHE Delft Institute for Water Education, Delft, the Netherlands.

Delft
28/08/2023

Abstract

Coastal aquifers worldwide are under an accelerating threat from saltwater intrusion and water scarcity due to human activities and climate change. This research aims to comprehensively understand the groundwater system of the Levant coastal region under different stresses. The main objectives include creating a 3D model that integrates variable-density groundwater flow and salt transport. The study investigates both historical and current groundwater conditions, examining indicators such as water budget, paleo fresh groundwater, submarine groundwater discharge (SGD), saltwater intrusion, groundwater depletion, and freshwater groundwater volume (FGV). The paleo-hydrogeographical model assesses the impact of sea-level changes during the last 30 ka, while the current status model represents the present groundwater conditions. Additionally, this research evaluates the reliability of global datasets for creating a supra-regional groundwater model. It examines how complexity features like geology and recharge influence model accuracy. The research continues to work on the development of the fully scripted and reproducible modelling framework to enhance the Global Coastal Groundwater Modelling toolbox (GCGM), initiated by Zamrsky et al. from the Utrecht University. Remarkably, this study presents the first-ever paleo-hydrogeographical model for the Levant region.

This research creates three different models to evaluate the reliability of global hydrogeological data for a supra-regional groundwater model. These models progressively incorporated more local data alongside the existing global data to increase their complexity and accuracy. A Global data based model (Lvnt 1) reasonably represents coastal geology but not in the mountainous areas. The model Lvnt 2, which combines global and a small amount of local hydrogeological data from peer-reviewed articles about the Levent area, does not significantly outperform the global-only data based model (Lvnt 2) in terms of performance. However, building model using global and well distributed and more amount local hydrogeological data (Lvnt 3), yields reliable results. Uniform recharge over diverse areas, like the Negev desert, leads to head overestimation. Data from PCR-GLOBWB global model is promising for recharge, but local data adjustments are key for accurate mountainous modelling. It was concluded that ignoring the ancient trapped salt results in not improved current salinity distribution. The GCGM toolbox enhanced and improved here for regional Levant conditions produces a reproducible groundwater model with about 10-hour runtime.

In the most realistic model (Lvnt 3), during the paleo-reconstruction period (the past 30 ka), the lowest sea-level at BP16000 exhibited the highest SGD. Matching the real situation, the model captures the phenomenon of submarine springs along Syria and Lebanon's coastline. Rising sea-levels increased drainage due to higher groundwater tables. A pattern emerged: higher sea-levels correlated with raised groundwater tables and decreased fresh groundwater volume. A robust linear correlation linked FGV to sea-level rise during the transgression period (BP16000 to BP00000). Delayed FGV response to sea-level changes, especially in the transgression period, resulted from low-permeable layers, preserving groundwater memory. Mountainous areas had stable groundwater levels, while they fluctuate in the coastal zones. Severe saltwater intrusion is observed in BP03000 since the sea-level was 7 msl. Paleo sea-level change has a fingerprint on the current salinity distribution e.g., evidence of paleo fresh groundwater over the last 22 ka persisted in the model and offshore at depths exceeding 1000 m.

The current model of sea-level at 0 msl, using the paleo salinity groundwater distribution, shows drainage exceeding recharge by 10 times in specific rivers and springs locations. Lebanon's mountains suffer a 180-meter groundwater table depletion due to the 2015 abstraction. Similar in the coastal zone (Negev Desert), over 40-meter depletion. 3 ka ago as sea-level reached 7 msl, trapped salt gradually freshened as the present sea-level is 0 msl. In contrast, severe saltwater intrusion in the southern Levant coast is computed due to groundwater abstraction and low groundwater recharge. Notably, Lebanon has the lowest potential for saltwater intrusion. Despite abstraction and constant sea-level, 1900-1977 observes a slight FGV increase, supporting the groundwater memory hypothesis.

Acknowledgments

I begin by expressing my utmost gratitude to Allah for the blessings and guidance that illuminated my path toward the completion of this study and research. I would also like to acknowledge and never forget my homeland, Palestine, the country to which I belong, always and forever.

I am deeply grateful to my parents, who nurtured and educated me, shaping my character to reach the point I have achieved as well as their continuous prayers and unwavering support. I would like to extend my thanks and heartfelt appreciation to my wife and my love for her boundless support, patience, and attentive ear at all times and places. I must not overlook expressing my gratitude to my in-laws for their ongoing prayers. I want to thank my brothers and sisters for their prayers, support, and for always standing by my side.

I am especially thankful to Gualbert Oude Essink for his generosity in sharing knowledge, patience, and guidance in helping me complete this work. I also express my gratitude to the Deltares team, particularly to Jude King for helping in the geological part. I appreciate Deltares for granting me the internship opportunity for six months. I am also thankful to Daniel Zamrsky for providing data, documentation and python tools.

At the IHE Delft, I extend my thanks to Yangxiao Zhou and Andreja Jonoski for their support and advice. I cannot forget to acknowledge the GroundwatCH program coordination team for their kindness and the Erasmus Mundus scholarship for their financial support throughout my master's studies. I am grateful to my professors at TU Lisboa and TU Dresden for their valuable guidance and support. In the end, I thank my colleagues in the GroundwatCH group and at the IHE Delft for their collaboration and for being nice to me.

Table of Contents

List of Figures

List of Tables

1. Introduction

Approximately 25% of the global population resides in coastal areas, relying on fresh groundwater as a key resource (Delsman et al., 2014; Zamrsky et al., 2018). However, the closeness to the sea and high population densities in these regions make them susceptible to salinization and increased freshwater stress due to overexploitation, limited groundwater recharge, and pollution (Ferguson & Gleeson, 2012; Werner et al., 2013). Coastal groundwater in many areas is characterized by salinity due to various factors such as sea water intrusion, upconing by upward flow in confining layers, and historical marine transgressions (Van Pham et al., 2019; Vincent & Violette, 2017). This salinization of coastal aquifers has significant consequences, including the salinization of abstraction wells, reduced agricultural productivity, deterioration of surface water quality, and adverse impacts on vulnerable ecosystems, all of which are expected to worsen in the face of global change (de Louw et al., 2010; Oude Essink et al., 2010).

Climate change, including sea-level rise, increased storminess, and drought (DeConto & Pollard, 2016; IPCC, 2022) are expected to further exacerbate the problem by reducing the available freshwater resources and increasing the risk of saltwater intrusion in coastal aquifers (Haasnoot et al., 2020; Xiao et al., 2021). There is more frequent alarming of sea-level rise forecasting because of climate change, e.g., (DeConto & Pollard, 2016) on the rapid collapse of the Antarctic ice sheets. Meanwhile, the region's rapidly growing population is putting additional and continuous pressure on already strained water resources, especially in semi-arid regions, where extraction may easily surpass the net recharge rate (Abu Ghazleh et al., 2011; Rodell et al., 2009; World Bank, 2009). Between 5% to 20% of the global population is expected to suffer from water scarcity because of population and climate changes (Schewe et al., 2014). In particular, the quick social, economic and industrial changes in addition to climate change (i.e. causing droughts) in the Mediterranean zone increase the water lack (Boithias et al., 2014).

Groundwater is a crucial source of freshwater for the majority of the Levant countries, e.g. 70% of the water use in Palestine is extracted from groundwater (Quba'a et al., 2018). The Levant region is currently experiencing a severe water crisis due to the complex interplay of multiple factors, including groundwater depletion, climate change related droughts, and overexploitation due to population growth. According to (Quba'a et al., 2018), there has been a significant decrease in groundwater storage of 3.08 ± 0.15 BCM per year in the Levant region. For example, approximately 60% of Syria's irrigated sites are dependent on groundwater, which is being used in an unsustainable manner and has led to overexploitation (Salman & Mualla, 2004).

This escalating water crisis in the Levant region presents a significant challenge to sustainable development, with potentially severe implications for agriculture, industry, and human health (Quba'a et al., 2018; Vineis et al., 2011). Urgent action is needed to address this issue, by providing a supra-regional model that quantitively and qualitatively defines the groundwater resources in the coastal area of the Levant under the aforementioned pressures. That should raise decision makers' awareness and help them take the necessary actions in order to sustainably use the groundwater resources.

The Utrecht University (UU) and Deltares are together developing modelling tools to assess these effects on groundwater systems. For instance, the modelling tool iMOD-WQ is a code that is developed for groundwater flow and salt transport that integrates SEAWAT and MT3DMS and is made parallel for the supercomputer to execute massive large-scale high-performance computing facilities for groundwater salinity modelling (Verkaik et al., 2021). iMOD-WQ was successfully used in previous studies (Delsman et al., 2023; Seibert et al., 2023; Van Engelen et al., 2019; van Engelen et al., 2021). At the same time, iMOD-Python (M. Visser & H. Bootsma, 2021) has also been developed to support MODFLOW groundwater modelling by facilitating the conversion of raw data into a completely defined MODFLOW model in order to allow the reproducibility and transparency of workflow, e.g. (Delsman et al., 2023). iMOD-Python can be used for building a simple 2D conceptual model or a complex 3D regional model with millions of grid cells.

The Global Coastal 3D Groundwater Model (GCGM) initiative has been started up in 2022 to aim for providing a toolbox that allows experts around the world to build their own (supra-) regional scale models. That is achieved by building open-source codes, which is a stepwise approach first using global hydrogeological databases while later adding local hydrogeological data and documentation when available. The modelling work cycle (Fig. 1) consists of (i) hydrogeological data preparing, (ii) setting up SEAWAT model in an iMOD-WQ environment, (iii) executing the model (iv) visualization.

The current GCGM (Global Coastal Groundwater Model) toolbox is still under construction and has limitations and uncertainties. Specifically, issues come up when moving from one study area to another, so it still needs development to generalize it for worldwide use, which is done by Deltares and the Utrecht University. The documentation (Zamrsky, 2023) is under progress to guide new users around the world. It is mainly focused on hydrogeological data handling needed for groundwater modelling such as simplified geological input data extracted from global data, and constant recharge value, etc.

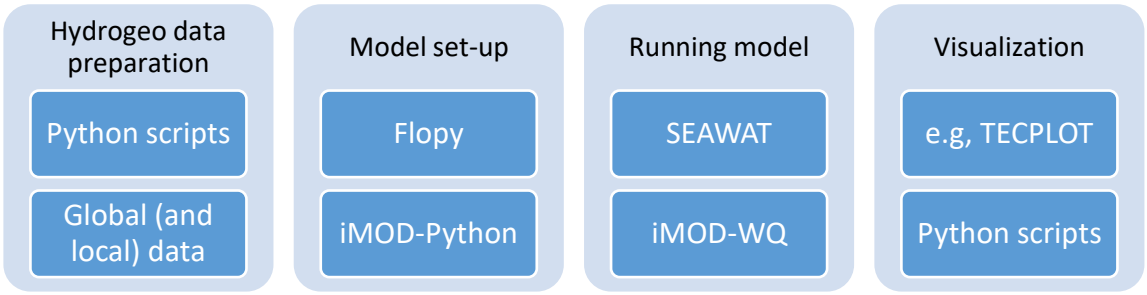

Fig. 1. GCGM flow chart

1.1 Research Objectives

The main objective of this research is to build and apply a 3D variable-density groundwater flow model and coupled salt transport model fully scripted and reproducible (using the GCGM toolbox) to simulate the historical and current quantitative and qualitative conditions of the groundwater system in the Levant coastal region.

The specific research objectives include:

1- **Paleo-Hydrogeographic Modelling:** Achieve a good performance and long-term simulation (last 30 ka) of the historical salinity conditions.
2- **Complex Feature Analysis:** Investigate the influence of complex geological structures and recharge by developing three alternative models and comparing their results to local hydrogeological data, thus identifying the level of detail required for accurately representing the local conditions.
3- **Impact of Environmental Changes:** Examine the impact of dynamic factors such as sea-level changes and human activities on groundwater indicators. These indicators encompass phenomena such as paleo fresh groundwater existence, groundwater depletion, fresh groundwater volume, change in submarine groundwater discharge, and saltwater intrusion.
4- **Improving GCGM Toolbox:** Refine and improve the numerical modelling capabilities of the GCGM toolbox by promoting its performance while using global databases and later incorporating local data.

1.2 Research Questions

1. What is the effect of more local and complex hydrogeological data input on the performance of the model?
2. Can we build a supra-regional groundwater model of the Levant, given predominantly global hydrogeological databases?
3. What is the effect of anthropogenic activities, and sea-level changes (paleo and present) on the groundwater indicators?

2. Literature Review

This chapter provides a review of the Levant (ground)water resources and water demands in addition to previous saltwater intrusion studies. Also, the recent studies of paleo-hydrogeographical modelling are reviewed in this chapter.

2.1 Levant Coastal (Ground)water System

The area of research encompasses the Levant region situated along the eastern coastline of the Mediterranean Sea, which comprises Syria, Lebanon, Palestine, Israel and a part of Egypt (Fig. 2). The entire study region has a total area of 26,771 km^2. The climate in the Levant varies from humid near the coast to dry and desertic inland. The highest water consumer is the agricultural sector in the Levant at 45.2, 57.8, 59.5, and 85.5% in Palestine, Israel, Lebanon, and Syria, respectively (Quba'a et al., 2018; World Bank, 2016). In contrast, the irrigated lands constitute about 20% of the Levant and the majority is urban at about 40% of the total area (Quba'a et al., 2018; Riccardo Biancalani et al., 2013). Water scarcity is a significant issue in the Levant countries. While Lebanon and Syria have limited water resources with renewable water of less than 1000 m^3/capita/year, Israel and Palestine face more severe water scarcity with a total renewable water of 228 and 189 m^3/capita/year respectively (Falkenmark, 1989; FAO, 2014). Groundwater resources are the main source of water for most of the Levant countries, except for Syria which relies on surface water storage through 78 dams at a total capacity of 16.6 BCM (FAO, 2014). Syria's Lake Asad, created by the Tabqa dam, holds about 14.6 BCM of water. Meanwhile, Lebanon only has two small dams that hold 0.22 BCM of water. The Levant also has significant surface water reservoirs such as Lake Tiberias, which can store 4 BCM of water, and the Dead Sea, which has approximately 143 BCM of highly saline water.

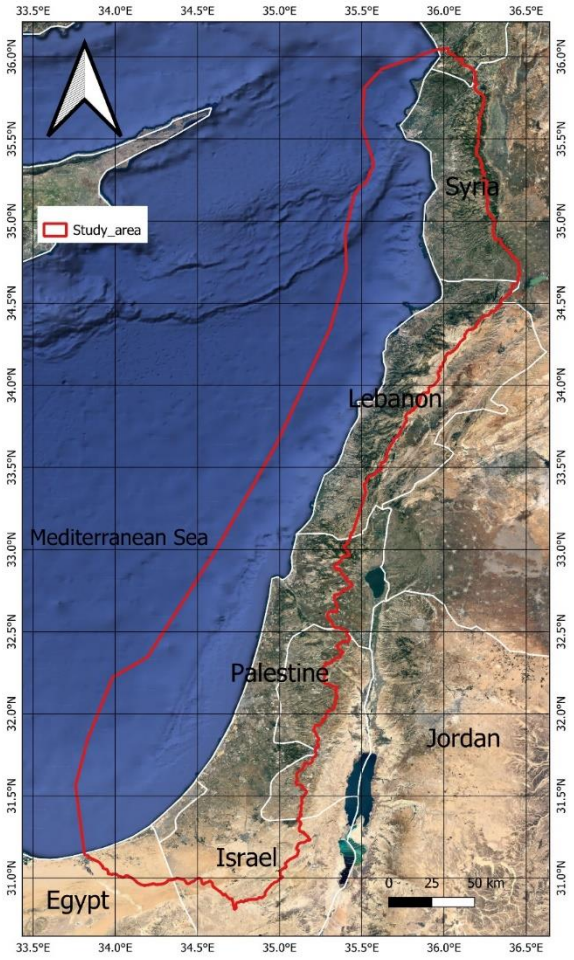

Fig. 2. Location map of the study region. The boundary of the study region (in red) is explained in section 3.2)

The Levant coastal groundwater system has been extensively investigated by numerous researchers. Table 1 provides an overview of previous studies on the Levant region that were utilized in this research. The groundwater situation of the Levant is presented extensively in section 10.

Table 1: Summary of the used previous studies in the Levant

Reference	Country	Overview
(Baba et al., 2021)	Syria	Maps of irrigation area, basins, population and precipitation, water consumption, distribution of groundwater wells, and TDS of groundwater
(Abou Zakhem & Hafez, 2007)	Syria	Groundwater level and EC in 1994 for the shallow coastal aquifers of Latakia and Tartous.
(Allow, 2011)	Syria	Model for the shallow groundwater system of Latakia (depth is less than 40 m). Hydrogeological properties of the layers. Water and salt budget for 1976 to 2020. Recharge data.
(Al-Charideh & Kattaa, 2016)	Syria	Isotope hydrology of deep groundwater in Syria: renewable and non-renewable groundwater and paleoclimate impact. Discharge, EC, Cl of Banyas and Al-sin springs. Map of TDS for the whole of Syria.
(Al-Charideh, 2004)	Syria and Lebanon	Coastal submarine springs in Lebanon and Syria: Geological, geochemical, and radio-isotopic study. Salinity measurements and images of springs in the sea
(Khadra & Stuyfzand, 2018)	Lebanon	Model for the coastal area of Damour. Hydrogeological properties, infiltration coefficient (%). recharge, pumping.
(Khadra & Stuyfzand, 2014)	Lebanon	HydroChemical System Analysis. Precipitation, evapotranspiration, runoff, recharge, pumping. Thickness and lithology (Cross sections).
(MoEW & UNDP, 2014)	Lebanon	Springs map and wells. Precipitation maps for 2008-2012. Recharge value. Water budget. Volume of recharge
(Shaban, 2020)	Lebanon	Annual rainfall 1950-2018. Discharge of springs (1970–2018). Hydraulic properties of aquiferous rock formations. Recharge information.
(Ghannam et al., 2009)	Lebanon	Examining Submarine Springs in Lebanon as a Possible Source of Water Supply
(Kalaoun et al., 2016)	Lebanon	Model of Tripoli (hydrogeological properties) pumping data.
(Halwani et al., 2022)	Lebanon	Quality and water level measurements
(Abu-alnaeem et al., 2018)	Palestine	Contour Maps of salinity and groundwater level.
(Jebreen et al., 2018)	Palestine	Groundwater quality samples from springs
(Qahman & Larabi, 2006)	Palestine	Model for the Gaza Strip. Hydrogeological properties, recharge, abstraction and contour maps of Cl and groundwater level for 1935 and 1969, 2000.
(Abusaada, 2011)	Palestine	Model for the West Bank Aquifer. Hydrogeological properties, recharge estimation, abstraction.
(Vengosh et al., 2005)	Palestine	Groundwater quality measurements and schematic cross section
(Musallam, 2021)	Palestine	Model for the Gaza Strip. Abstraction (2010-2019), hydrogeological properties, population, abstraction, recharge prediction and future scenarios till 2040
(Aish, 2022)	Palestine	Recharge estimation for the Gaza Strip
(Yechieli & Sivan, 2011)	Palestine and Israel	Precipitation, recharge, and schematic cross section of the coastal plain.
(Banusch et al., 2022)	Palestine and Israel	Model for the West Bank Aquifer. Hydrogeological properties, springs drainage modelling.
(Dafny et al., 2010)	Palestine and Israel	Water budget of the West Bank Aquifer, and comparison between models of previous studies.
(Laskow et al., 2011)	Palestine and Israel	Boreloges give the top and bottom elevation of the Deep Cretaceous Aquifer.
(Burg & Gersman, 2016)	Israel	2-point quality measurements and hydraulic properties
(Bresinsky et al., 2023)	Israel	Recharge, springs discharge present and 1959. Hydrogeological parameters. Precipitation and springs discharge 1972 - 2000
(Yechieli et al., 2019)	Israel	Quality measurements. Saltwater intrusion.
(Quba'a et al., 2018)	Levant	A comprehensive study of the groundwater system of the Levant. They computed a trend of groundwater storage depletion at a rate of 3.08 ± 0.15 BCM/year.

Saltwater intrusion is becoming a major hazard to coastal areas across the world. It occurs when saltwater infiltrates freshwater aquifers, resulting in deterioration of drinking water supplies and loss of agricultural land. In recent years, researchers have made considerable progress in understanding the complex mechanisms that cause saltwater intrusion.

Changes in land use, sea-level rise, and over-pumping of groundwater are all causes that can contribute to saltwater intrusion. According to research, climate change is exacerbating the situation by altering precipitation patterns and increasing the frequency of extreme weather events.

In the Levant, many studies have been conducted to deeply understand the phenomena of saltwater intrusion caused by anthropogenic activities and climate change. In Palestine, Abd-Elaty et al. (2020) found saltwater intrusion at 35 g TDS / l reached 3.17 km in the Gaza aquifer in 2010. According to their prediction, the sea-level rise may have restricted saltwater intrusion effect on the aquifer because of the reverse slope of the aquifer bed. Abu Al Naeem et al. (2019) reported that 75% of the Gaza area is under a considerable depression cone, 19 m drop in the groundwater table below msl with a distance equal to 4.3 km from the shoreline due to overexploitation.

Coastal groundwater salinity in Lebanon has risen severely because of saltwater intrusion, rising from 0.1 to 20 g/l since the 1960s (Khair et al., 1994; Lababidi et al., 1987). A study covering 1999 to 2002 found salinity rates of 0.7 dS/m to 5.5 dS/m (Bakalowicz, 2009). Beirut faces increased salinity of over g/l (Saadeh, 2008), and recent samples in Beirut reached about 37.5 g TDS/l (Saadeh et al., 2017) due to urbanization. Chloride concentrations increased from 340 mg/l to more than 4200 mg/l between 1972 and 1985 (Khair et al., 1992).

Paldor et al. (2019) investigated the Deep Cretaceous Aquifer in northern Israel, predicting salinization of groundwater 5 km onshore apart from the shoreline after 190 years due to overexploitation leading to groundwater level decline. Effective confinement results in quicker saltwater intrusion, implying a preference for semi-confined aquifers for groundwater abstraction. Yechieli et al. (2019) estimated the average rate of saltwater intrusion into the Deep Cretaceous Aquifer to be nearly 2 to 3 m/year.

2.2 Paleo-Hydrogeographical Modelling

Paleo-hydrogeographical modelling, utilizing variable-density groundwater flow and salt transport, has become a valuable method for investigating historical boundary effects and overcoming data limitations in present-day studies. This approach acknowledges the influence of paleo-hydrogeographical conditions on groundwater quality in large-scale systems (Edmunds & Milne, 2001; Jasechko et al., 2017). Paleo-hydrogeographical modelling is built based on known salinity distribution from a specific past time as initial conditions, initiating model simulations from a time when the salinity distribution has little impact on the present-day distribution (Delsman et al., 2014).

Paleo-hydrogeographical modelling studies commonly focus on simulation periods from the Late Pleistocene to the present, taking advantage of reliable starting points provided by sea-level lows (<-120 m relative to present sea-level) at the end of the last glacial cycle (Grant et al., 2012; Spratt & Lisiecki, 2016). During this time, coastal groundwater systems were likely predominantly fresh, at least in the top 100-200 m (Zamrsky et al., 2020). Previous studies by Delsman et al. (2014); Larsen et al. (2017); Van Pham et al. (2019); Meyer et al. (2019); Seibert et al. (2023); Van Engelen et al. (2019) adopted this approach, except for Zamrsky et al., (2020), who studied a full glacial-interglacial cycle spanning the last 130 ka.

Delsman et al. (2014) conducted a paleo-hydrogeographical modelling study in the coastal region of the Netherlands, considering sea-level rise and paleogeographic changes over the past 8.5 ka. The study revealed the impact of substantial saltwater intrusion during the Holocene

transgression (via overtopping and overwash) and the system's ongoing recovery, highlighting the absence of a steady-state condition.

Larsen et al. (2017) utilized geophysical data and 2D numerical models to demonstrate the preferential intrusion of saltwater into former river branches in the Red River Delta, Vietnam, during the Holocene transgression. Their groundwater flow simulations revealed that the age, thickness, and permeability of marine sediments play a significant role in the leaching of salty porewater into the freshwater aquifer, with trapped seawater still influencing groundwater salinity in nearby aquifers.

Meyer et al. (2019) utilized 3D paleo-hydrogeographical modelling to investigate the salinization of a low-lying coastal groundwater system in Denmark over the past 4.2 thousand years, incorporating hydrogeological, geophysical, and geochemical data to develop a comprehensive numerical model for understanding the historical and potential future changes in the saltwater affected groundwater system.

Van Pham et al. (2019) developed a paleo-hydrogeographical model for a 2-D cross-section in the Mekong Delta, Vietnam, to investigate regional salinization over the past 60 ka, revealing that the majority of fresh groundwater in the delta was likely recharged during the Pleistocene and is currently declining despite being in a humid climate. The study emphasized the influence of sea-level changes and the preservation of freshwater by the Holocene clay cap in the Mekong Delta groundwater system.

Van Engelen et al. (2019) overcame the lack of salinity and geological data in the Nile Delta groundwater system via 3D paleo-hydrogeographical modelling (variable-density groundwater flow modelling) spanning 32 ka using parallel computation. The paleo modelling tested different conceptual models and assessed the validity of the Holocene-transgression hypothesis in explaining observed salinities.

Zamrsky et al. (2020) constructed a paleo-hydrogeographical model for the groundwater systems around the world including a continental shelf, encompassing the last 130 ka, which represents a complete cycle of interglacial and glacial periods, taking into account sea-level fluctuations and changes in the coastline.

Seibert et al. (2023) conducted a 3D paleo-hydrogeographical modelling study in Northwestern Germany, focusing on the Holocene period (last 9 ka), to reconstruct the evolution of groundwater salinities. Their research incorporated highly detailed time-variant boundary conditions, accounting for factors such as surface elevation changes, sea-level rise, coastline shifts, groundwater abstraction, drainage network development, and quantification of processes influencing salinization.

The aforementioned studies have confirmed the value of paleo-hydrogeographical modelling in determining present-day groundwater salinity distributions in coastal areas, but they have also highlighted the need for significant computational resources and time, which motivates the investigation of techniques to improve efficiency while maintaining reliable results. The goal of this study is to find ways to minimize the computing time necessary for paleo-hydrogeographical modelling in the Levant while maintaining the accuracy of the resulting present-day salinity groundwater distributions. The novelty of this research is the use of global hydrogeological data for supra-regional scale model and the analysis of its effect on the accuracy of the model by comparing the results with observational hydrogeological data.

3. Methods and Materials

3.1 Introduction

The research methodology of (supra-) regional model building can be categorized into six distinct components, as illustrated in Fig. 3.

1. In the learning phase of combining tools such as iMOD-WQ (Verkaik et al., 2021) and Python scripts (Zamrsky et al., 2022) provided by Deltares and Utrecht University, complemented by the Flopy library (Bakker et al., 2016).
2. For data collection, both local and global datasets were gathered, encompassing geology, hydrogeology, recharge, salinity, and groundwater levels.
3. Subsequently, in the model development phase, three paleo-hydrogeographical alternative models were pursued. The first alternative model was built based on global hydrogeological data while the second and third alternative models included different degrees of complexity by incorporating local hydrogeological data, as depicted in Fig. 4.
4. The performances of the three alternative models were tested via comparison with local observational data (head and salinity).
5. The results of the best alternative model were analyzed through different groundwater indicators e.g. paleo-fresh groundwater occurrence, change in fresh groundwater volume, groundwater depletion, saltwater intrusion and submarine groundwater discharge.
6. Recommendation for further developing the GCGM as well as writing the thesis report.

The flowchart in Fig. 4 offers a comprehensive insight into methodology components 3 to 6: the model development process, performance testing results, results and analysis, and reporting.

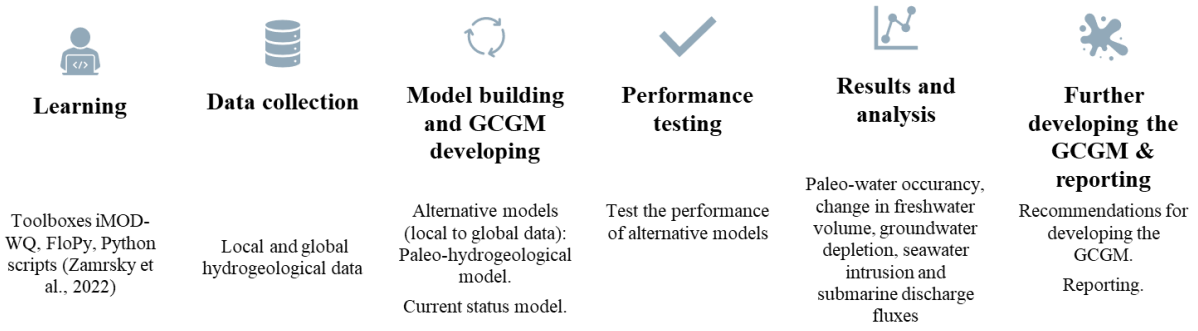

Fig. 3. Methodology framework of the (supra-) regional model building

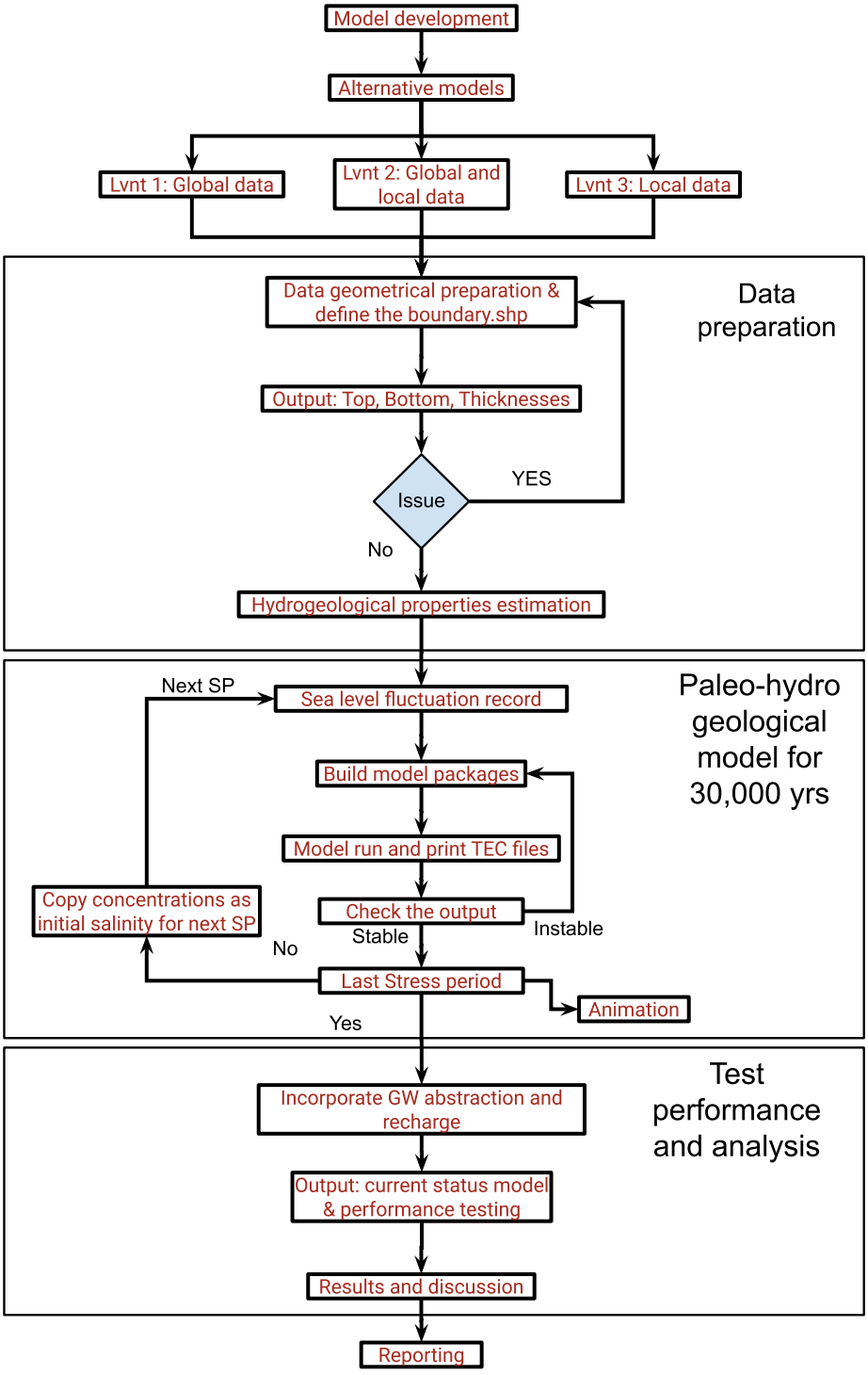

Fig. 4. Flow chart of components 3 to 6: model development, test performance, results, analysis, and reporting.

3.2 Study Region and Conceptual Model

The study region encompasses the eastern coastal aquifer of the Mediterranean Sea, specifically situated within the Levant basin, as illustrated in Fig. 5. This region spans approximately 26,771 km^2 onshore and 22,127 km^2 offshore. To better comprehend the topographic characteristics, Fig. 5 displays the digital elevation model (DEM) of the region.

The topography of the Levant region displays considerable variation, transitioning from sea-level along the Mediterranean coast on the western side to elevations approaching 1000 m, 3000 m, and 1500 m in Palestine, Lebanon, and Syria, respectively, on the eastern side.

Geographically, the Levant onshore domain can be delineated into three distinct longitudinal topographical zones: (1) coastal plain zone, (2) foothill and lower slopes zone, and (3) upper slopes and mountain zone. On the other hand, the offshore domain can be classified into other distinct longitudinal topographical zones: (1) continental shelf (-100 to 0 msl), (2) continental slope (-800 to -100 msl); (3) continental rise (less than -800 msl).

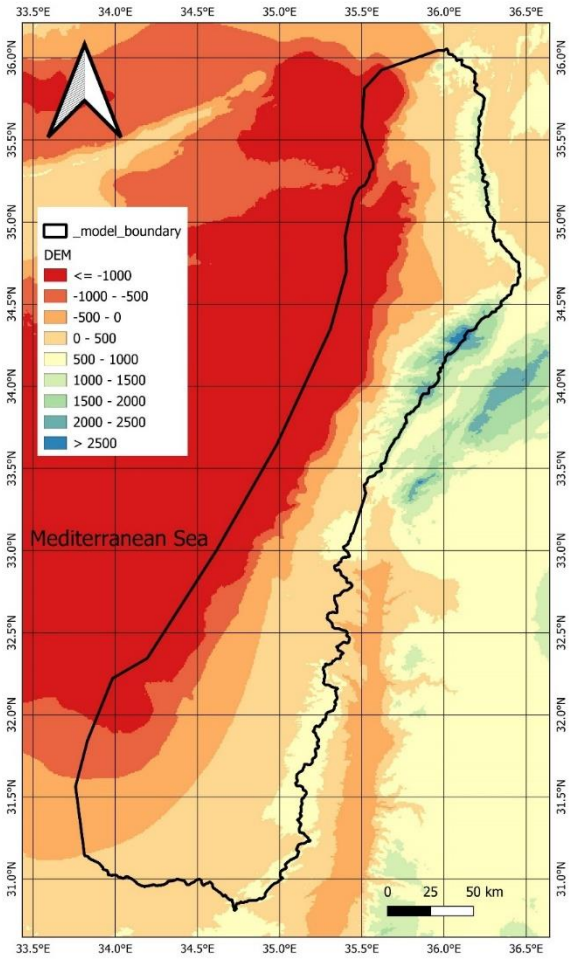

Fig. 5. Model boundary extracted from sub-basin boundaries global database called HydroBASINS (Lehner and Grill, 2013) and DEM (Weatherall et al., 2015)

3.2.1 Geology and Hydrogeological Evolution

The Levant region has witnessed two major tectonic events in history (Abou Zakhem & Hafez, 2007). The late Jurassic to early Cretaceous uplift exposed Jurassic Limestone through erosion and karstification. The early Tertiary closure of the Tethyan Sea formed a collision zone, causing the initial uplift of the Coastal Mountain Range. Sea-level fluctuations led to thick limestone deposition in the early Jurassic, late Jurassic, and middle Cretaceous (Abou Zakhem & Hafez, 2007; Ponikarov, 1966). The coastal mountain range comprises Jurassic, Cretaceous, and Neogene sedimentary rocks, including limestone, dolomite, marl, and chalky marls. The Tertiary contains marls, marly limestone, Neogene marls, limestone, conglomerates, and basalt (Ponikarov, 1966). These structures impact groundwater flow directions as pathways or boundaries (MoEW & UNDP, 2014).

The majority of previous hydrogeological evolution studies have concentrated on the onshore portion of the Levant region, thus the forthcoming details primarily delineate the hydrogeological evolution of this onshore portion. The Regional Deep Cretaceous Aquifer, a crucial component, represents an upper Mesozoic sedimentary sequence (Al-Charideh & Kattaa, 2016). Comprising late Albian - Turonian lithofacies, the aquifer is a shallow-water carbonate platform with limestone, dolomite, terrigenous marl, and chalk, as seen in Table 2 and Fig. 6 (Lewy, 1991; Braun and Hirsch, 1994; Sass and Bein, 1982). Low-permeable layers

of marl, clay, and shale of the Aptian and Lower Albian age underlie the aquifer (Abusaada, 2011, Weinberger et al., 1994). The Cretaceous Aquifer is characterized by a highly karstic nature, with a thickness ranging from 600 to 1000 meters, comprising three distinct lithological layers: the lower and upper sub-aquifers, primarily limestone and dolomite, separated by a lower permeability layer with a thickness of 50 to 90 m (Abusaada, 2011). The upper sub-aquifer, made up of Turonian and Cenomanian age rocks, mainly consists of karstic limestone and dolomite. Westward, it is confined by the confining layer - Senonian chalk and marl with a thickness that could reach 600 m in some areas (SUSMAQ, 2004; Avisar et al., 2003; Dafny et al., 2010; Weinberger et al., 1994). However, eastward, the upper sub-aquifer is not confined allowing water to infiltrate. Impervious chalky marls form a barrier along the western boundary, except for potential connections along the Binyamina fault with the Mediterranean Sea (Guttman et al., 1995). The eastern boundaries were established based on groundwater divides (Abusaada, 2011). Although the southern boundary is adjacent to a saltwater body, its impact on the flow dynamics of the northern region is minimal due to low hydraulic gradients (Bresinsky et al., 2023).

The Levant region exhibits Quaternary sediments along the shoreline, consisting of coastal marine formations and sand dunes of conglomerate and sandstone, overlying impervious marine clays of Pliocene age, as presented in Table 2 and Fig. 6 (Abou Zakhem & Hafez, 2007; Issar, 1968). In the northern part of Syria, these Quaternary formations overlay Pliocene marls, creating a good aquifer with a thickness of 25 meters (Khouri & Droubi, 1981). However, in Lebanon, the shallow coastal Quaternary unit is minimal with an average thickness of about 5 meters compared to other units (Khadra & Stuyfzand, 2018). The Palestinian section of the Mediterranean coastal aquifer also shows a decrease in thickness from about 180 meters near the coastline to a few tens of meters near the eastern boundary (Yechieli & Sivan, 2011). It comprises inter-layered sandstone, calcareous sandstone, siltstone, red loam, and marine and continental clays of the Pleistocene age, with clay interlayers subdividing the aquifer into multiple subaquifers (M. Mushtaha et al., 2019; Musallam, 2021; Nativ & Weisbrod, 1994; Yechieli & Sivan, 2011). The lower subaquifers are confined, while the upper ones are phreatic, and intermediate aquitards separate the aquifer into four subaquifers near the coastline (M. Mushtaha et al., 2019; Musallam, 2021; Yechieli & Sivan, 2011).

Table 2: Properties of the onshore hydrogeological units (HK and VK are the horizontal and vertical hydraulic conductivities, respectively)

Epoch or Age	Layer	Geological deposits	Thickness (m)	HK (m/d)	VK (m/d)	Porosity	Reference
Quaternary	Alternating aquifer and aquitard	Sand, slit and clay.	5, 180	Aquifer: 10 -30 Aquitard: 0.2	Aquifer: 0.1 - 0.3 Aquitard: 0.02	0.2-0.4	(Allow, 2011; Bruce et al., 2007; Khadra & Stuyfzand, 2018; Qahman & Larabi, 2006; Shaban, 2020)
Eocene, Paleocene, Senonian	Aquitard / aquiclude	Chalky to marly limestone	5–590	7.3E-07 - 1.8	-	0.08-0.4	(Banusch et al., 2022; Burg & Gersman, 2016; Dafny et al., 2010; Khadra & Stuyfzand, 2018; Zilberbrand et al., 2014)
Turonian, Cenomanian	Aquifer	Limestone, dolomite	300 - 400	0.02 - 1000	HK/10000 to HK/10	0.08-0.19	(Abusaada, 2011; Al-Charideh & Kattaa, 2016; Banusch et al., 2022; Dafny et al., 2010; Khadra & Stuyfzand, 2018; Shaban, 2020)
Cenomanian	Aquitard	Marl, chalk	50 - 120	-	8.0E-08 - 0.3	0.08	
Late Albian	Aquifer	Limestone, dolomite	80 - 450	0.02 - 1000	1.0E-06 - 16	0.12	

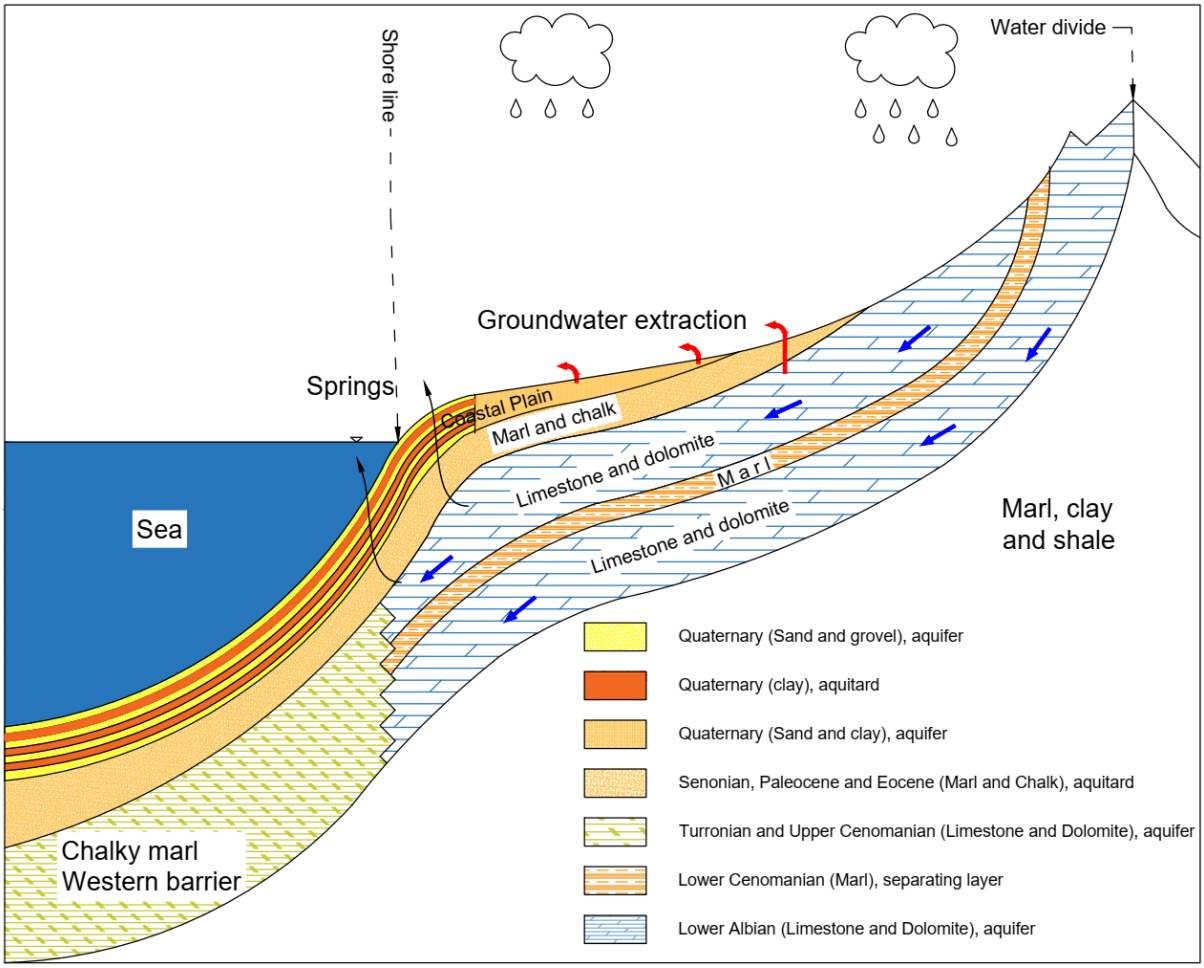

Fig. 6. Hydrogeological conceptual model of the Levant groundwater system showing the geological ages, lithological units, groundwater flow direction, and other hydro(geo)logical components.

3.2.2 Rivers and Springs

The coastal region exhibits a well-developed hydrographic network with numerous westward-flowing springs and rivers (Abou Zakhem & Hafez, 2007; Shaban, 2020). Notable rivers (Fig. 7) in the area include:

1. Al-Kabir Ashamali River: The largest river in the coastal region, with a vast catchment area of 180 km^2. It discharges into the Mediterranean Sea south of Latakia, experiencing significant flow rate increases during flood periods. The Al-Kabir Ashamali dam is situated upstream, 20 km from the coastal line.

2. Al-Kabir River: This river spans 59 km and flows throughout the year, forming the boundary between Lebanon and Syria. Fed by more than 70 major springs, Naba'a Al-Safa Spring (North) is the largest contributor.

3. Ibrahim River (Adounis River): It maintains a year-round flow and has the highest discharge rate among coastal Lebanese rivers, averaging about 495 MCM/year. The river extends approximately 50 km and is mainly fed by Roueisat Spring and Afqa Spring, located near Daher Al-Kadeeb Mountains, in the Qartaba region.

4. Litani River: The largest Lebanese river entirely within Lebanon, stretching 174 km from the Bekaa Plain southward and then diverging seaward in the south. It boasts the largest catchment area, covering about 2110 km^2.

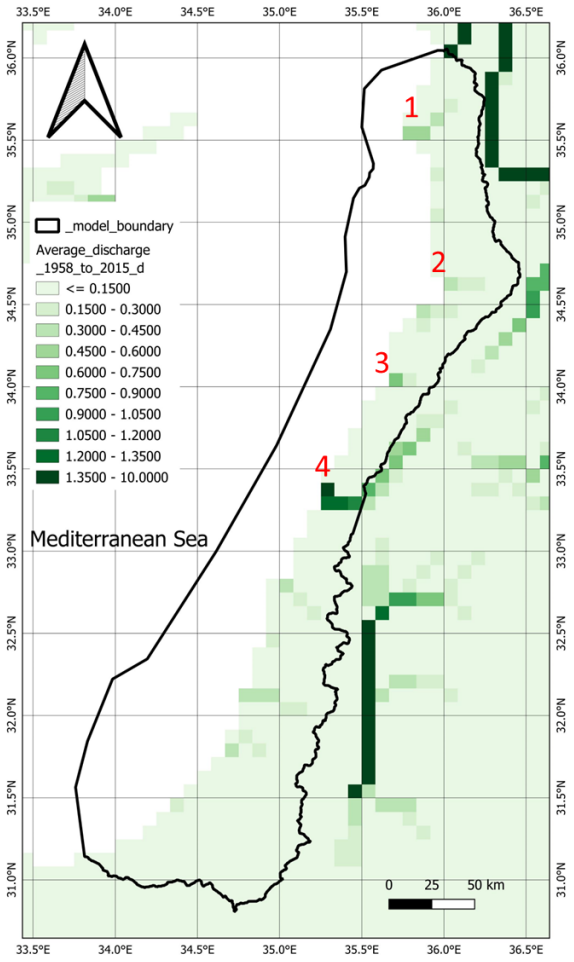

Fig. 7. Average daily surface water discharge (m^3/sec) for the period from 1958 to 2015, after (Sutanudjaja et al., 2018), (1) Al-Kabir Ashamali, (2) Al-Kabir, (3) Ibrahim, and (4) Litani Rivers

Interestingly, despite the presence of these rivers, no deltas are formed at their mouths where they meet the sea (Abou Zakhem & Hafez, 2007). Since the rivers have no significant existence in the study region, their effect on the groundwater will be neglected in this research.

Springs play a vital role in Lebanon's water resources, exhibiting diverse flow rates and regimes due to various hydrogeological mechanisms. Lebanon's complex geology, particularly dominant rock deformations, allows groundwater to emerge on the terrain surface as surface water flows. Despite the hydrogeological linkage between springs, rivers, and groundwater, springs contribute significantly to Lebanon's water budget, discharging approximately 1410 MCM/year. The country hosts around 1800–2000 major springs, primarily karstic and fault springs, as seen in Figure S 5 (MoEW & UNDP, 2014). Many rivers in Lebanon heavily rely on these springs as their primary water source. Snowmelt from the mountainous regions accounts for a substantial portion of water in these springs (Shaban, 2020). However, increasing population and fluctuating climatic conditions have led to the drying up of numerous springs, with some experiencing a discharge rate decline of over 40% in the last five decades (Shaban, 2020).

Lebanon also exhibits a unique hydrogeological phenomenon – submarine springs. These springs are widespread along the Lebanese shoreline, where karstic conduits and faults transmit groundwater into the sea. Along the coast, there are 54 sub-marine springs, including 15 offshore springs, discharging water at various distances from the coast (Shaban, 2020).

3.2.3 Recharge

The recharge varies from close to 0 mm/year in the south of the Levant to 365 mm/year in the north. Table 3 demonstrates the collection of local data of recharge in different locations of the Levant. Fig. 8 shows the recharge data extracted from the global database PCR-GLOBWB (Sutanudjaja et al., 2018).

The PCR-GLOBWB model (Figure S 6) is a global hydrological model that simulates various processes, including moisture storage, water exchange, precipitation, evaporation, snow and glacier melt, and runoff partitioning. It also considers human water use by estimating demands for different sectors and calculating withdrawals from groundwater and surface water sources based on availability and pumping capacity. In their research, the model's global database was utilized, encompassing daily estimations of recharge, abstraction, and channel discharge spanning the period from 1958 to 2015.

Table 3: Local data of recharge in the Levant

Precipitation (mm/yr)	Recharge (mm/yr)	Date	Region	Reference
800-2000	330		Coast, Syria	(Al-Charideh, 2004)
800-1000	365	2012	Latakia, Syria	(Kinan, 2015)
352 and 1,163	219	2004	Damor, Lebanon	(Khadra & Stuyfzand, 2014)
	150 - 250	1965	West Bank, Palestine	(Abusaada, 2011)
327	8.5 - 110	2015-2019	Gaza, Palestine	(Musallam, 2021)
225-579	0-192	2020	Gaza, Palestine	(Aish, 2022)
600	200	Before 2002	Coast Palestine and Israel	(Yechieli & Sivan, 2011)

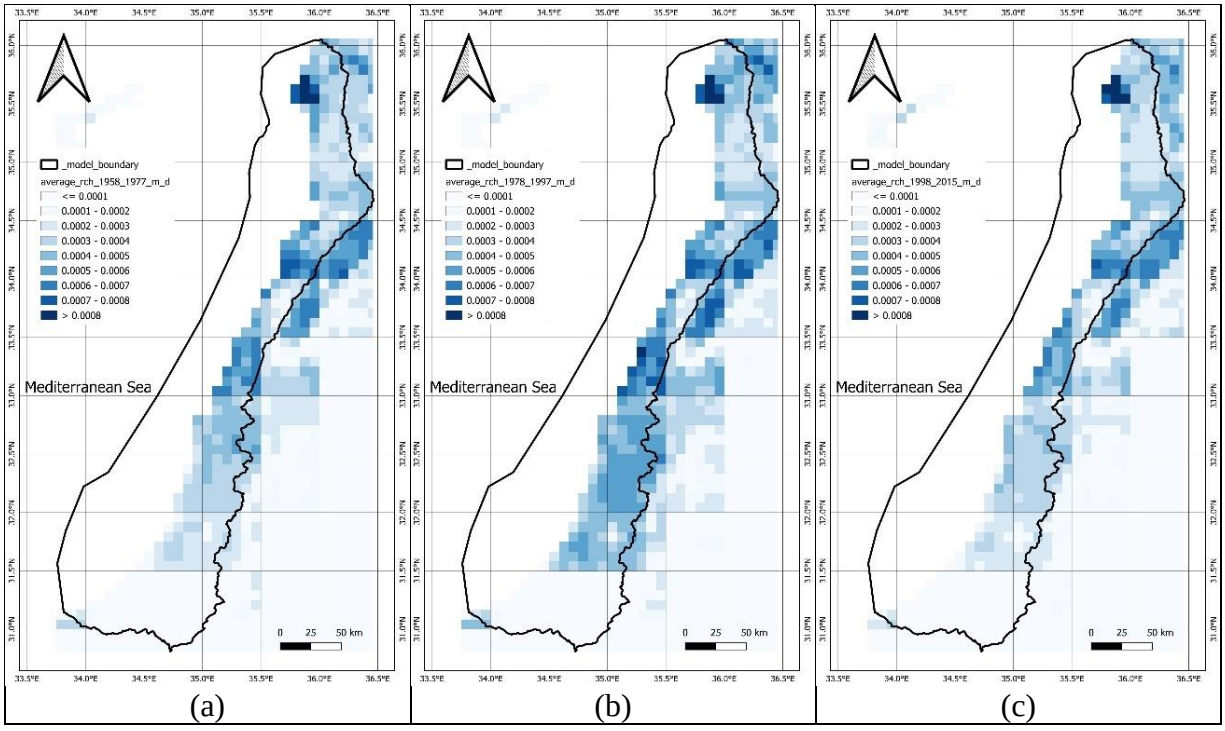

Fig. 8. Average daily groundwater recharge (m/day) for the periods (a) 1958 to 1977, (b) 1978 to 1997 and (c) 1998 to 2015, after (Sutanudjaja et al., 2018).

3.2.4 Groundwater Abstraction

The groundwater abstraction varies among the countries of the study region depending on the country's access to other sources of water. For example, groundwater abstraction forms 72.9 % of the total demand in Palestine since it is the only source of renewable water there. Table 4 exhibits the total groundwater abstraction of each country (for the whole country not only the portion of interest). Fig. 9 shows the groundwater abstraction data extracted from the global database PCR-GLOBWB (Sutanudjaja et al., 2018).

Table 4: Local data of groundwater abstraction in the Levant, after (Quba'a et al., 2018)

Country	Population	Available water (m^3/capita/year)	Groundwater abstraction MCM/year (% of the total consumption)	Groundwater abstraction m^3/day/km^2	Water withdrawal by sectors as a percentage of total demand		
					Agricultural	Municipal	Industrial
Syria	22,158,000	764.1	4811 (35.5%)	71.2	87.5	8.8	3.7
Palestine	4,295,000	188.7	246.3 (72.9%)	112.1	45.2	47.9	6.9
Lebanon	4,547,000	906.8	695 (50.5%)	182.2	59.5	29	11.5
Israel	8,215,000	227.6	1,225 (68.8%)	152.1	57.8	36.4	5.8
			Average	129.4			

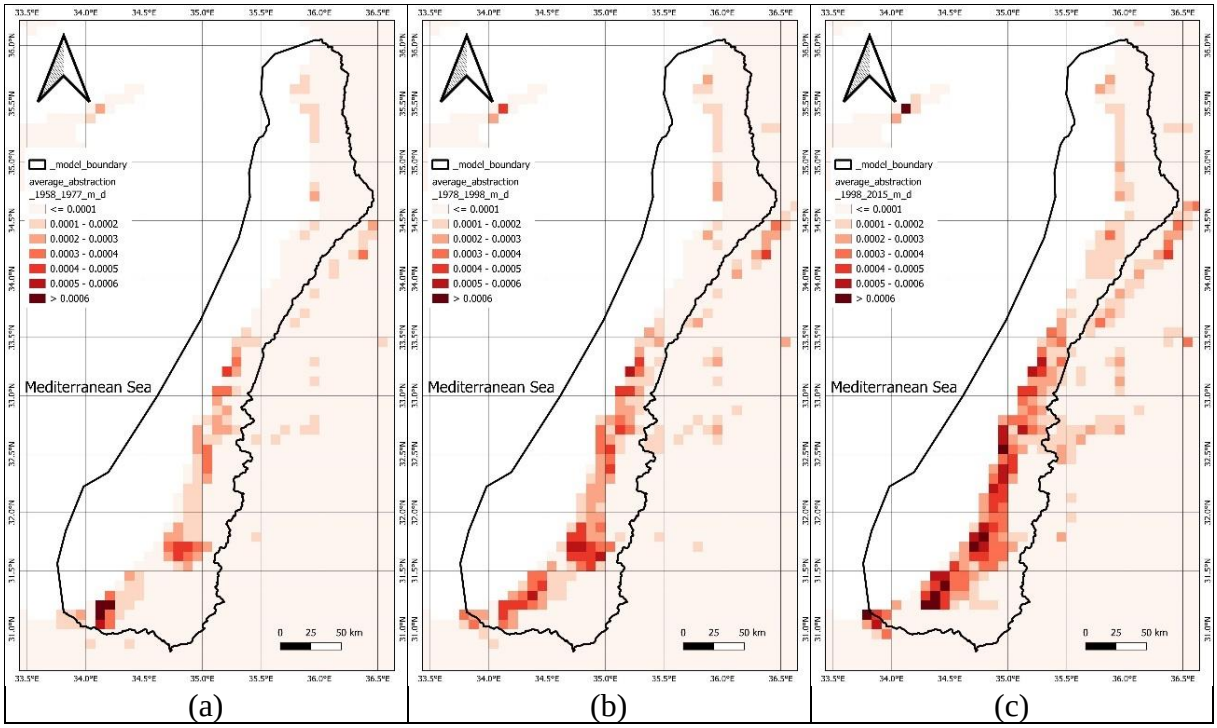

Fig. 9. Average daily groundwater abstraction (m/day) for the periods (a) 1958 to 1977, (b) 1978 to 1997 and (c) 1998 to 2015, after (Sutanudjaja et al., 2018).

3.2.5 Groundwater Quality and Quantity

Unfortunately, the Levant Coastal region exhibits a scarcity of groundwater data both in terms of quantity and quality, particularly in Lebanon and Syria. To evaluate the model's performance, a limited number of observation points and contour maps extracted from reputable published studies were utilized. The collected data can be found in Appendix A.1 and Annex 8.

Analysis of this data reveals that the groundwater level in the Quaternary deposits ranges from 0 to 40 msl. Conversely, in the mountainous regions where the Cretaceous Aquifer is present, the groundwater level exceeds 300 msl in unconfined areas, while it descends to less than 100 msl in confined areas.

In the mountainous regions, the Total Dissolved Solids (TDS) display a range of 0.2 to 1 g/l. This is not only induced due to the evaporation process but because of stems from prolonged water-rock interaction especially evaporate dissolution (Al-Charideh & Kattaa, 2016; Kooi & Groen, 2003; Yangui et al., 2011). Notably, the highest recorded TDS was observed in the Quaternary Aquifer of Palestine, reaching 4 g/l due to saltwater intrusion, while reaching 40 g/l at the edge of the Deep Cretaceous Aquifer. The Senonian deposit has limited water flow and long residence time resulting in brackish to saline water, in some spots ranging from 600 to 11,000 mgCl/l sourced by prolonged water-rock interaction mixed with old seawater trapped in

the system during the Pliocene age (Burg & Gersman, 2016; Livshitz, 1997; Rosenthal et al., 1999; Zilberbrand et al., 2014).

3.3 Thickness of Unconsolidated Coastal Aquifers (Global Datasets)

The cross-sections collected by Zamrsky, (2021) were used as a global dataset to estimate the bottom elevation and the total thickness of the models. The study presents a method for estimating the thickness of unconsolidated coastal aquifers based on available data on the geology, topography, and bathymetry of the coastal area. The authors use a combination of numerical modelling and statistical analysis to estimate the aquifer thickness for multiple coastal areas around the world, covering roughly 20% of the global coastline. The locations of the cross sections within the study area are presented in Fig. 10. The schematization of the cross section estimation is presented in the Appendix, Figure S 4.

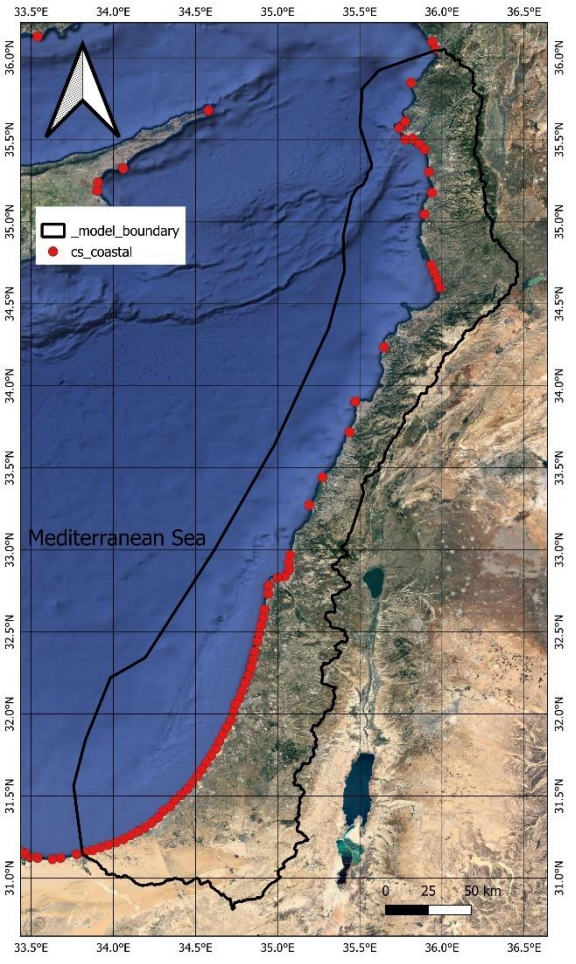

Fig. 10. Location of the cross sections created by Zamrsky, (2021)

In the course of their study, the researchers collected state-of-the-art open-source global datasets (listed in Table S 1) that provided valuable information on various aspects, including topography and bathymetry (Weatherall et al., 2015), regolith thickness estimation (Pelletier et al., 2016), global-scale aquifer thickness (de Graaf et al., 2015), lithology (Hartmann and Moosdorf, 2012), and coastline position (Natural-Earth, NA).

The researchers relied on the combination of topographical and lithological data to estimate the thickness of coastal unconsolidated sediment aquifer systems. Specifically, the aquifer thickness estimation method utilized the topographical slope of outcropping bedrock formations and the extent of the coastal plain. The latter was defined by a low topographical slope (Weatherall et al., 2015), unconsolidated sediment lithology (Hartmann and Moosdorf, 2012), and regolith thickness thicker than 50 m (Pelletier et al., 2016). To capture the bathymetrical and topographical profile, the cross sections spanned 200 km both inland and offshore from the coastal point.

3.4 Numerical Model Setup

3.4.1 Fixed Settings

A supra-regional 3D variable-density groundwater flow coupled with salt transport model was built with the GCGM toolbox. To facilitate the generation of all the essential input files for SEAWAT (Langevin et al., 2008), the FloPy package (Bakker et al., 2016) was employed.

These input files were subsequently inserted in the iMOD-WQ software (Verkaik et al., 2021), which basically is the SEAWAT groundwater modelling compute code (Langevin et al., 2008).

The region of interest covers a total area of 49,785 km^2, and a grid size of 756 m × 940 m (equivalent to 30 arcsec ×30 arcsec) was adopted for the model. The number of the model layers varied between the different alternative models, explained later in section 3.4.2. The model considered the underlying bed as impermeable.

The model boundaries are depicted in Fig. 2. General head boundaries (GHB) with different conductance values were assigned as the boundary condition. Initially, a conductance value of 1,000,000 m^2/day was assumed for the offshore side (sea bed and boundary) to closely resemble a constant head boundary condition, as shown in Fig. 11a. However, this resulted in model instability leading to flow is not converged issues due to the high top elevation differences between neighboring model cells. To mitigate this numeric issue, a systematic approach was followed to reduce the conductance whenever the top elevation difference between a cell and any of its eight surrounding cells exceeded 50 m. By contrast, the onshore side, which mostly represents a water divide, was represented by GHB with zero conductance, therefore representing a no-flow boundary. The water divide location was determined using HydroBASINS (Lehner & Grill, 2013) and DEM (Weatherall et al., 2015). Although the southern part of the onshore side is not strictly a water divide, it was treated as a neglectable flow boundary due to its very low hydraulic gradient (Abusaada, 2011; Bresinsky et al., 2023). The decision to avoid the use of constant head is to avoid the zone of influence model issues when e.g. recharge or extraction are changed, and to better represent the sea- and groundwater interaction.

For paleo-hydrogeographical modelling, the GHB stage was set equal to the corresponding sea-level for each stress period. The specific source and sink mixing (SSM) value for the GHB was 35 g/l, respectively, representing the salinity concentration.

The specific representation of drainage rivers, valleys, and springs, along with their corresponding discharges, could not be fully realized within the scope of this study due to time constraints and the extensive supra-regional scale involved, coupled with data availability limitations. As a result, a simplified approach was employed through the drainage package, wherein surface water extraction was simulated by incorporating all model cells with elevations higher than the sea-level. The determination of drainage conductance was accomplished using the following equation (Harbaugh, 2005) adhering to predefined upper and lower limits of 50000 and 10000 m^2/day, respectively. The drainage stage was assumed to be equivalent to the top elevation minus 1 m. The results chapter incorporates the locations where drainage is active, along with the corresponding drainage quantities.

$$Conductance = \frac{KLW}{M} \ (L^2/T) \quad (1)$$

Where K is the vertical hydraulic conductivity of the model cell (m/day); L is the Length of the model cell (m); W is the width of the model cell (m); M is the thickness of the model cell (m).

The exclusion of the River package from the model was predicated on an assessment of the hydrogeological attributes specific to the coastal region of the Levant (see section 3.2.2). Notably, rivers in this region were found to be of marginal importance with seasonal variance and exerted minimal influence on the supra-regional scale.

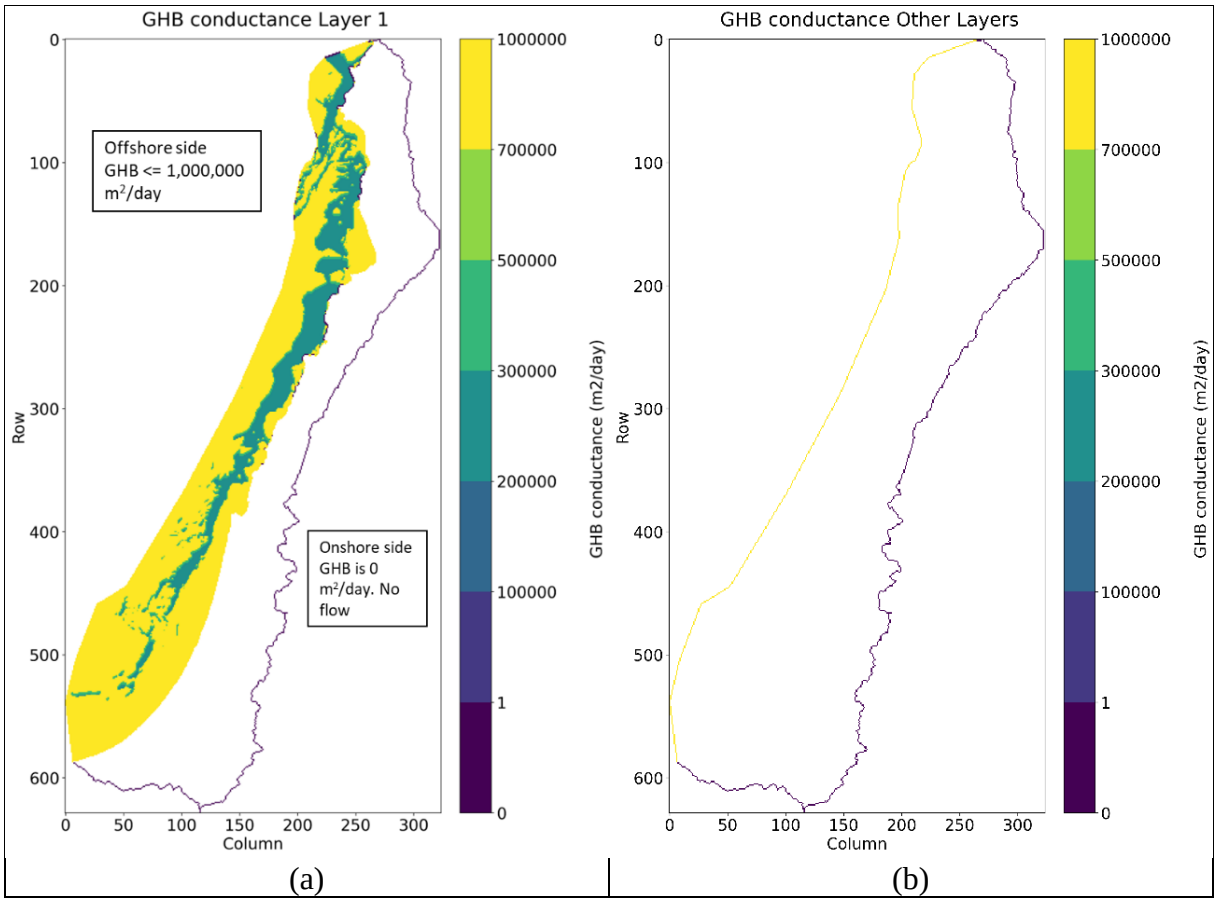

Fig. 11. GHB conductance of (a) the 1st model layer, and (b) the remaining model layers

A Paleo-hydrogoegraphocal reconstruction model was developed to come up with a (initial) groundwater salinity distribution, to address the inherent limitations in groundwater salinity data, as discussed in section 2.2. The model's extensive temporal resolution spanning a period of 30 ka allows for the simulation of past sea-level fluctuations which was estimated by Reeder et al. (2002), shown in Fig. 12. The shoreline position is dependent on the sea-level. Consequently, this approach offers valuable insights into the historical dynamics of freshwater infiltration into subsurface water reservoirs, including aquifers and aquitards as well as sea- and freshwater interaction. The paleo reconstruction period was divided into 30 stress periods, each spanning a duration of 1000 years. The model was designed as a steady-state flow system for groundwater quantity, implying that the initial hydraulic head of each stress period remained constant (assumed to be 1 m) and independent of the preceding stress period. However, with regard to salinity transport, the model was treated as transient, signifying that the initial concentration for each stress period was imported from the final concentration of the previous stress period, as depicted in Fig. 13. This can be conducted by assigning the storage coefficient to be zero while the effective porosity is 0.25.

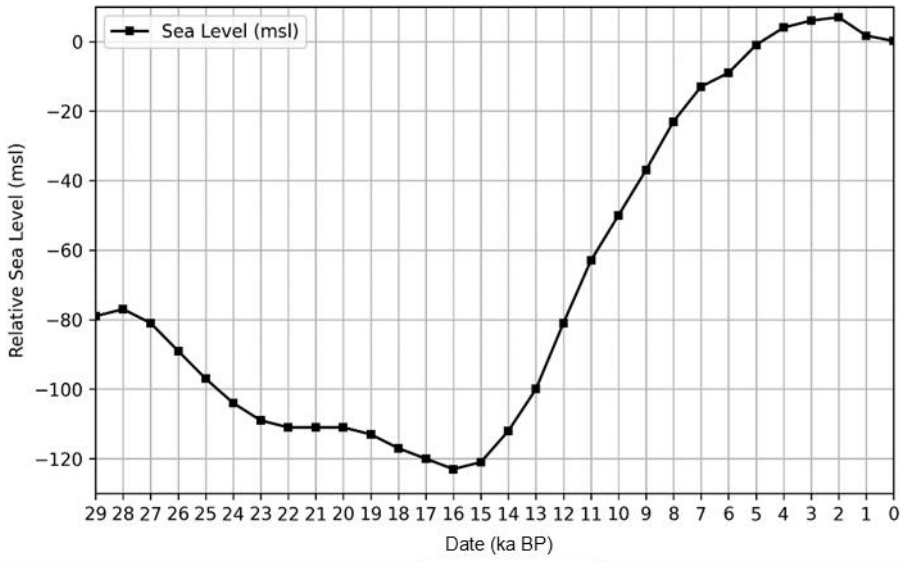

Fig. 12. Sea-level change along the simulation period of the last 30 ka, after (Reeder et al., 2002)

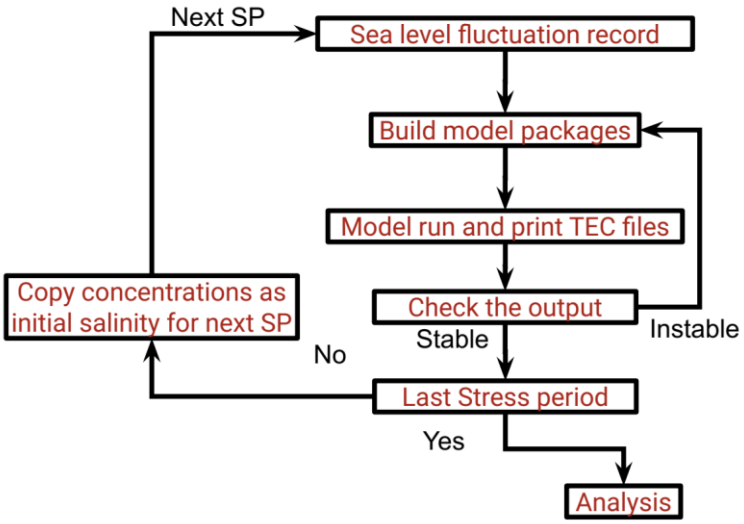

Fig. 13. The loop of paleo-hydrogeographical model simulation

A finite-difference (FD) approach was employed to numerically solve the model's underlying partial differential equations. The selected solver allowed the research to utilize a fixed stepsize of 5 years (1826 days) to shorten the simulation in time. To maintain stability, the properties of the model cells were designed to restrict the stepsize of each iteration, ensuring that particles did not move more than one cell. This constraint proved essential in preventing unrealistic behaviour and ensuring computational stability. By examining intermediate flow velocity findings, insights were gained into parameter adjustments necessary to achieve computational stability, resolve non-convergence issues, and reduce model runtime. For each stress period (SP) in the paleo-reconstruction, the model was divided into five time steps to facilitate accurate and efficient numerical solutions for that specific period.

Total Dissolved Solids (TDS, in g/L) in modelling was used to represent salinity. As the mean sea-level at 30 ka BP was approximately -79 m MSL, the initial fresh-saline groundwater distribution was assumed to be saline (35 TDS g/L, similar to present TDS of sea water) for the zone of top elevation less than -79 m MSL. The zone of top elevation more than -79 m MSL

was assumed to be filled with fresh groundwater with 0.05 TDS g/L. The values of the other used parameters are presented in Table 5.

The simulation of the paleo-hydrogeographical model commenced from historical salinity conditions, and by integrating recent groundwater abstraction and recharge data from the global model (PCR-GlOBWB), it represented the current groundwater quantity and quality. The current status model was simulated over three SPs: 1900-1977, 1978-1997, and 1998-2015.

Table 5: Parameters fixed throughout the simulation

Parameter	Value	Unit
Effective porosity	0.25	-
Storage coefficient	0	-
Sea salinity	35	g TDS /l
Initial freshwater salinity	0.05	g TDS /l
Recharge salinity	0.05	g TDS /l
Longitudinal dispersivity	0.1	m
Horizontal transversal dispersivity	0.01	m
Vertical transversal dispersivity	0.01	m
Molecular diffusion coefficient	8.64×10^{-5}	m^2/day
GHB stage	Sea-level	m
GHB conductance	300,000 – 1,000,000	m^2/day
DRN stage	Surface elevation - 1	m
DRN conductance	1000 – 5000	m^2/day
Duration of paleo stress period	1000	Year
1 year	365.25	days
Number of time steps per stress period	5	-
Cell size	756 × 940	m

3.4.2 Alternative Models

Three different alternative models were built in order to represent different degrees of feature complexities (geology and recharge) using the GCGM toolbox, therefore, testing the capability of global databases in building global and knowing the degree of complexity in the model features (geology and recharge) should be added to represent the reality. As seen in Table 6, the first alternative model (Lvnt 1) was built totally using global databases while the second alternative model (Lvnt 2) was created using global databases and little local hydrogeological data. Lastly, Lvnt 3 was generated using extensive and well-spatial distributed local hydrogeological data in addition to global data.

The methodology involves conducting a paleo reconstruction run (30 ka ago) for the three alternative models, followed by the addition of abstraction to simulate the current status of the groundwater system. The primary focus of this section lies in the comparison of the three alternative models in their current status simulations. By executing a detailed analysis of these models, the study aims to shed light on their respective performances and capabilities in representing the present conditions of the groundwater system.

Table 6: The differences between the alternative models

Parameter	Lvnt 1	Lvnt 2	Lvnt 3
Source of data	Global	Global and little local	Global and Local
Recharge	0.000274 m/d		Modify PCR-GLOBWB, global model using local data
Geological hydrogeological properties	Generated using global data	Changing the global data parameters to get better matching with local	Geological interpolation using only local data from 20 articles
Inland boundary	No flow	No flow	No flow

3.4.2.1 Lvnt 1

Lvnt 1 was built using only global data (Table 7) and following the assumption of the GCGM toolbox.

Table 7: Global datasets that were used in the alternative models using approaches/concepts from (Zamrsky et al., 2018, 2020)

Dataset name	Description	Resolution	References
GEBCO 2014	Global topography and bathymetry	30 arcsec	(Weatherall et al., 2015)
Average soil and sedimentary deposit thickness	Dataset of soil, intact regolith, and sedimentary deposit thicknesses. max. estimated depth is 50m.	30 arcsec	(Pelletier et al., 2016)
ATE	Estimations of Unconsolidated groundwater system thickness	Vector	(Zamrsky et al., 2018)
Recharge, abstraction and discharge	Daily estimation for 1958 to 2015	5 arcmin	(Sutanudjaja et al., 2018)
Aquifer/aquitard combination	Based on mud/sand ratio	-	(Zamrsky et al., 2020)
Recharge estimation	Global recharge maps	-	(Zamrsky et al., 2020)

The bottom elevation and unconsolidated sediment thickness of paleo-hydrogeographical model were computed using global datasets and cross-sections gathered by Zamrsky, (2021).

The scripts initially determine the bottom elevation by subtracting unconsolidated sediment thickness (Pelletier et al., 2016) (Fig. 14a) from the surface elevation (Weatherall et al., 2015). On the other hand, the cross sections (indicated in Fig. 10) contain diverse information, including the estimation of sediment deposit thickness computed by Zamrsky, (2021), as mentioned in section 3.3. Subsequently, a buffer with a predefined offset of 10 km is applied around the cross sections (Fig. 14b).

A grid is employed to define the final aquifer thickness and bottom elevation, linearly interpolating the thickness estimated by Pelletier et al. (2016) and the buffer of cross sections through linear interpolation, as illustrated in Fig. 15a.

Significant elevation spikes can be attributed to the initial estimation of bottom elevation using linear interpolation (Fig. 15a and b). These spikes have the potential to distort the estimates if there are disparities between the cross-sectional points. Despite capturing general trends, such as the presence of deeper sediment in the southern domain of the model, this interpolation method is not suitable for the stability of the groundwater model. To mitigate this issue, a smoothing algorithm is employed, performing a cell-by-cell traversal through the grid and calculating mean values within a specified radius. In this model, a radius of 30 cells, as presented in Fig. 15c and d is utilized.

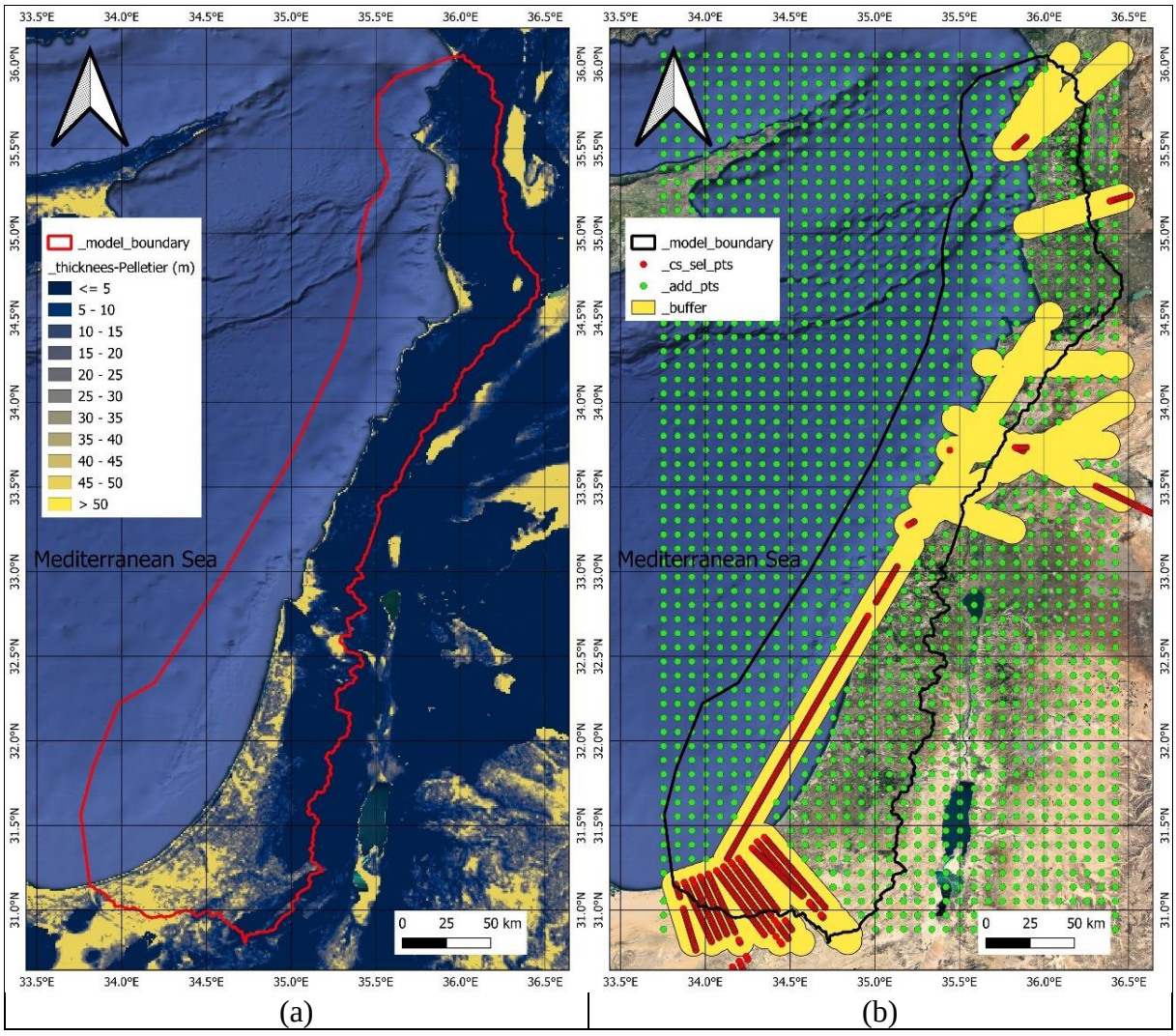

Fig. 14. Lvnt 1: (a) Average soil and sedimentary deposit thickness, after (Pelletier et al., 2016), and (b) grid combination from thickness estimated by Pelletier et al. (2016) and the buffer of cross sections (Zamrsky, 2021)

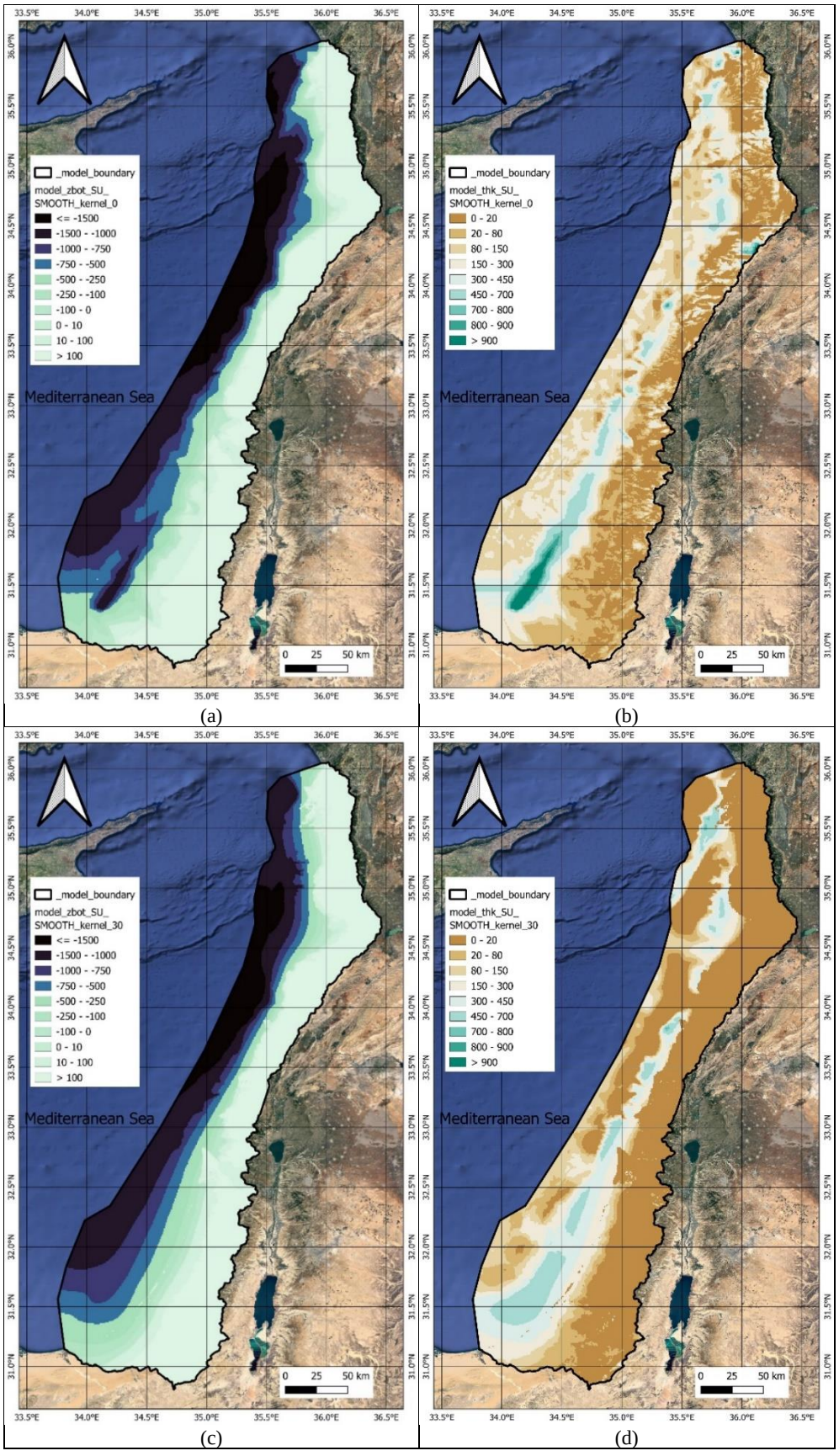

Fig. 15. Lvnt 1: Computed bottom elevation and thickness using the combination of the thickness array (Pelletier et al., 2016) and the cross section (Zamrsky, 2021) (a), (b) initial estimation (linear interpolation) and (c), (d) smoothed estimation with kernel 30

Following the usage of global database, the model layers discretization was estimated using regional-scale geological heterogeneity quantification and simulation algorithms, created by Zamrsky et al. (2020). This quantification process yielded estimates of a sand/mud composition, which were then used to determine the fractions of aquifer and aquitard sediment layers. Subsequently, the aquifer-aquitard layer combinations were randomly assigned, and the thickness of each individual layer was also determined randomly, ensuring that the entire groundwater system thickness was adequately represented.

The model domain was divided into 11 vertical layers (following the topography), with the thicknesses of these layers estimated randomly based on the assumed aquifer-aquitard combination and the sand/mud composition. Specifically, the top layer was set at 5% of the total thickness, while the remaining layers were generated with a maximum limit of 10% of the overall thickness. The aquitard layers' total thickness was calculated based on the mud composition ratio (51%), represented in 5 layers, while the aquifer layers' total thickness was determined by the sand composition ratio (49%), represented in 5 layers.

Similarly, the horizontal hydraulic conductivities of both the aquifer and aquitard layers were assumed, with a mean of 10 m/d and a standard deviation of 2.5 m/d for the aquifers (sand), and a mean of 0.025 m/d and a standard deviation of 0.01 m/d for the aquitards (clay). The uppermost sediment layer was assumed sand when the surface level is more than 0, otherwise, it was assumed clay. In all cases, the vertical hydraulic conductivity was assumed to be 10% of the horizontal hydraulic conductivity.

Table 8: Lvnt 1: Hydrogeological setting of the models

Layer No.	Thickness (%)	Classification	HK mean and standard division (m/d)	VK (m/d)
1	5	Aquitard/Aquifer	If top elevation < 0, HK is Aquitard at 0.025. Else, HK is Aquifer at 0.025	10% HK
2	9.2	Aquifer	10 and 2.5	
3	9.2	Aquifer	10 and 2.5	
4	9.2	Aquifer	10 and 2.5	
5	9.2	Aquifer	10 and 2.5	
6	9.0	Aquitard	0.025 and 0.01	
7	10.0	Aquifer	10 and 2.5	
8	9.8	Aquitard	0.025 and 0.01	
9	9.8	Aquitard	0.025 and 0.01	
10	9.8	Aquitard	0.025 and 0.01	
11	9.8	Aquitard	0.025 and 0.01	

Unfortunately, there is no available historical data spanning the past 30 ka that provides a comprehensive record of recharge in the Levent region. However, Zamrsky (2021) developed a global model based on multiple linear regression to estimate past groundwater recharge rates by incorporating precipitation, potential evapotranspiration, land use, and clay content, allowing for estimations up to 30 ka ago. Based on Zamrsky (2021) the value of recharge in the Levant is considered uniform at 100 mm/year (0.274 mm/d) over the past 30 ka.

Calibration the model was not executed, acknowledging that calibration would only be feasible for recent time periods. Additionally, conducting a thorough sensitivity analysis was not possible due to the extensive computational time required. Nevertheless, the model's accuracy was evaluated by comparing the simulated outcomes with observed groundwater levels and TDS measurements.

After the final stress period of the paleo-hydrogeographical, an estimation of the predevelopment period's (prior to extensive abstraction) concentration has been derived. To simulate the present conditions, the initial concentration is retrieved from the last stress period of the paleo-hydrogeographical model. Additionally, recharge was kept as it is (0.274 mm/d) while the abstraction was extracted from the global model PCR-GLOBWB. These details have been elaborated in Section 3.4.1 (Fig. 9).

3.4.2.2 Lvnt 2

As part of the research objectives, this study aims to assess the integration of local data within the model. Lvnt 2 represents the second version of the model, wherein the assignment of aquifer/aquitard combinations and hydraulic properties is informed by local studies. It is essential to emphasize that Lvnt 2 closely resembles Lvnt 1 in terms of its setup and model development, except for modifications related to the computation of bottom elevation, aquifer/aquitard combinations, and hydraulic properties.

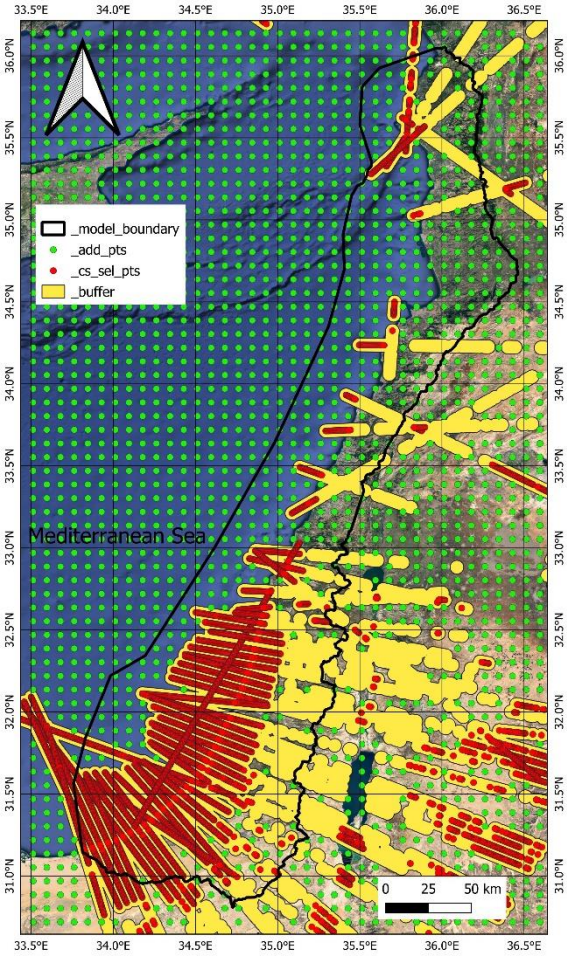

Fig. 16. Lvnt 2: Grid combination from thickness estimated by Pelletier et al. (2016) and the buffer of cross sections

The determination of the bottom elevation followed a comparable approach to that of Lvnt 1, with a notable refinement involving the incorporation of additional estimated points derived from the cross sections presented by Zamrsky, (2021), as depicted in Fig. 16. The model bottom elevation and the total thickness of Lvnt 2 are depicted in Fig. 17.

Furthermore, the estimation of hydrogeological properties in this study draws from the insights of three studies that focused specifically on the coastal groundwater system (Musallam, 2021; Qahman & Larabi, 2006; Yechieli & Sivan, 2011).

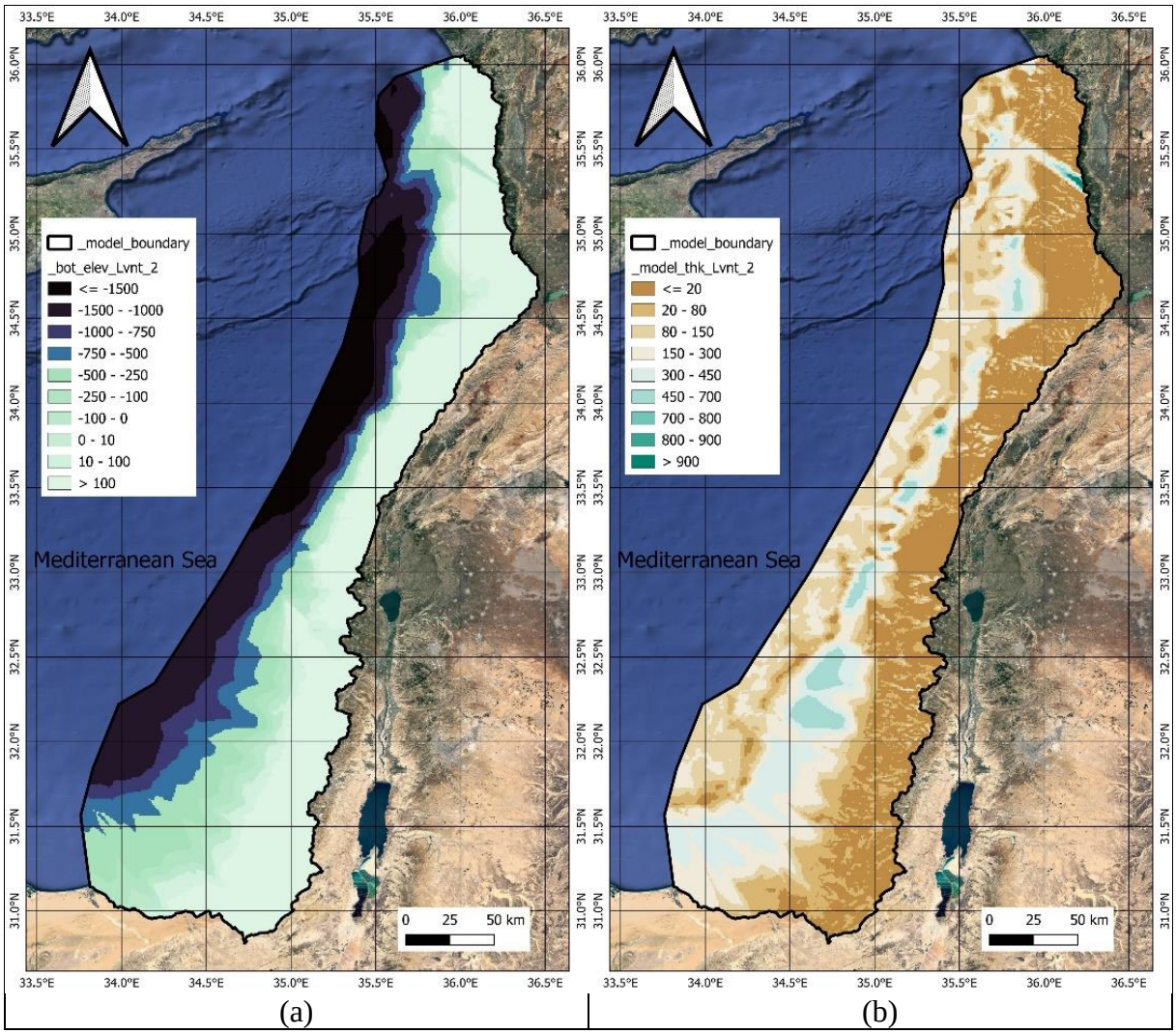

Fig. 17. Lvnt 2: Computed bottom elevation and thickness using the combination of the thickness array (Pelletier et al., 2016) and the cross section (Zamrsky, 2021) (a), (b) initial estimation (linear interpolation)

Table 9: Lvnt 2: Hydrogeological setting of the models

Layer No.	Thickness (%)	Classification	HK mean and standard division (m/d)	VK (m/d)
1	5	Aquitard/Aquifer	If top elevation < 0, HK is Aquitard at 0.2. Else, HK is Aquifer at 30	10% HK
2	8	Aquifer	30 and 5	
3	5	Aquitard	0.2 and 0.02	
4	12	Aquifer	30 and 5	
5	12	Aquifer	30 and 5	
6	4	Aquitard	0.2 and 0.02	
7	8.5	Aquifer	30 and 5	
8	8.5	Aquifer	30 and 5	
9	8	Aquitard	0.2 and 0.02	
10	13	Aquifer	30 and 5	
11	8	Aquitard	0.2 and 0.02	
12	8	Aquitard	0.2 and 0.02	

3.4.2.3 Lvnt 3

The Lvnt 3 model was formulated utilizing localized datasets. The initial phase encompassed the discretization of the model through geological interpolation (section 4.2.1), executed using the Geoscience ANALYST software. The foundational geological data were extracted from a

diverse studies, e.g. (Abusaada, 2011; Al-Charideh & Kattaa, 2016; Allow, 2011; Asfahani, 2021; Bar et al., 2013; Burg & Gersman, 2016; Dafny et al., 2010; Gomez et al., 2007; Gvirtzman et al., 2014; Kalaoun et al., 2016; Khadra & Stuyfzand, 2014; Laskow et al., 2011; MoEW & UNDP, 2014; Nader et al., 2016, 2018; Ponikarov, 1966; Qahman & Larabi, 2006; Shaban, 2020; Shaban & Shaban, 2010; Yechieli et al., 2009, 2019).

The geology of the model was constructed, featuring 15 distinct layers aligned with the conceptual model, as delineated in Fig. 6 and Table 10. The model layers follow the topography; however, the allocation of layer properties was undertaken in accordance with zonal attributes, as indicated by the conceptual model in Fig. 6 and deduced from prior research endeavors. Hydraulic properties corresponding to each layer (as depicted in Table 10) were defined within the parameter range delineated in Table 2. Additional insight into the model's foundation is provided by the presentation of the model's bottom elevation and overall thickness, both illustrated in Fig. 18. Detailed layer-specific bottom elevations and thicknesses can be perused in Appendix A.3, particularly in Figure S 7 and Figure S 8.

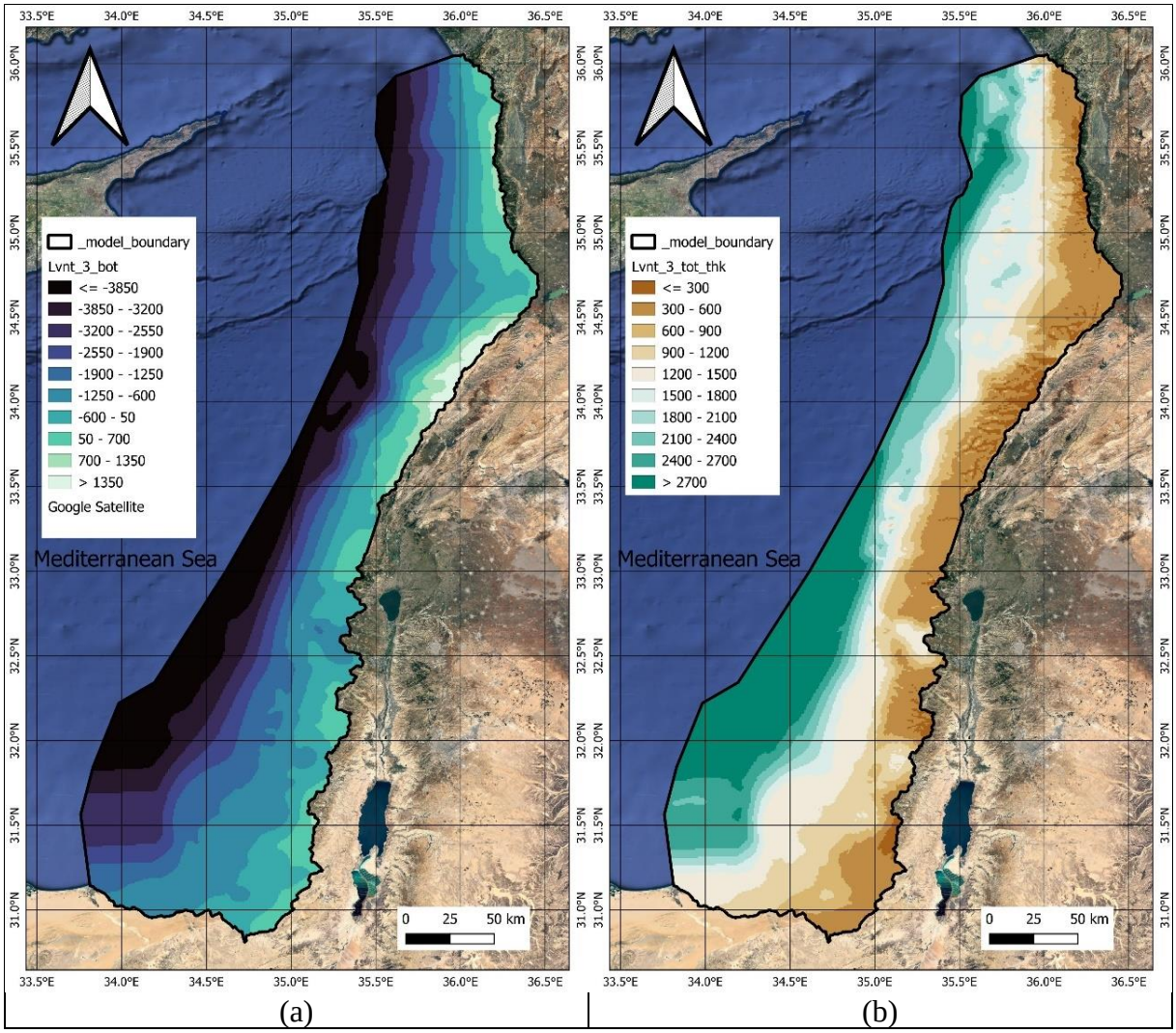

Fig. 18. Lvnt 3: Computed (a) the bottom elevation of the model and (b) the total thickness of the model from the geological interpolation using local data.

Given the utilization of localized data, the calibration of the model is more realistic as more control over the model was acquired. The calibration process was undertaken with a specific focus on the period spanning from 1900 to 1958, which is a stress period stress to the steady state flow conditions. The essential groundwater abstraction data were extracted from the global

dataset, specifically the PCR-GLOBWB, as elucidated in section 3.2.4. It is noteworthy that during the calibration phase, an observation of low hydraulic heads within the mountainous region emerged, even in instances where hydraulic conductivities were significantly reduced. Upon a comprehensive comparison of the global recharge data with the localized zones, disparities encompassing overestimations and underestimations in many zones of the Levant were discerned.

Table 10: Lvnt 3: Hydrogeological setting of the models (the spatial distribution of the parameters is presented in Appendix A.3)

Layer No.	Epoch or Age	Thickness (m)		Classification	HK mean (m/d)	VK (m/d)
		Onshore	Offshore			
1	Quaternary	2 – 30	30 – 115	Aquifer	3 - 15	10% HK
2		2 – 45	45 – 185	Aquifer	3 - 15	
3		2 – 30	30 – 115	Aquitard	0.1 – 0.2	
4		2 –70	70 – 275	Aquifer	3 - 15	
5		2 – 70	70 – 275	Aquifer	3 - 15	
6		2 – 25	25 – 90	Aquitard	0.1 – 0.2	
7		2 – 50	50 – 195	Aquifer	3 - 15	
8		2 – 50	50 – 195	Aquifer	3 - 15	
9		2 – 45	45 – 195	Aquitard	0.1 – 0.2	
10		2 – 75	75 – 300	Aquifer	3 - 15	
11	Eocene, Paleocene, Senonian	25 – 245	50 – 250	Aquitard / Aquiclude	0.001	
12		25 – 240	50 – 250	Aquitard / Aquiclude	0.3 and 0.02	
13	Turonian, Cenomanian	300 – 350	300	Aquifer	a	b
14	Cenomanian	50 – 90	50 – 90	Aquitard	0.4	10% HK
15	Albian	300 - 350	300	Aquifer	a	b

a: high spatial variation (see Figure S 9)
b: high spatial variation (see Figure S 10)

Regrettably, the accessible localized data (as detailed in Table 3) were deemed insufficient to enable comprehensive mapping of the entire study area. As a pragmatic resolution, manual interventions were introduced to adjust the average daily recharge estimations for the interval spanning from 1958 to 2015, drawing from the PCR-GLOBWB dataset. This iterative refinement facilitated a more congruous alignment of the modeled recharge values with localized data (Fig. 19), thereby effectively addressing the conundrum of low hydraulic heads in the mountainous sectors.

Upon the calibration of the model, the determined geological and hydrogeological attributes, as well as the refined recharge estimates, were harnessed as fixed inputs for the subsequent paleo-hydrogeographical modelling, thus culminating in a comprehensive representation encompassing various stress periods, ultimately extending to the current status.

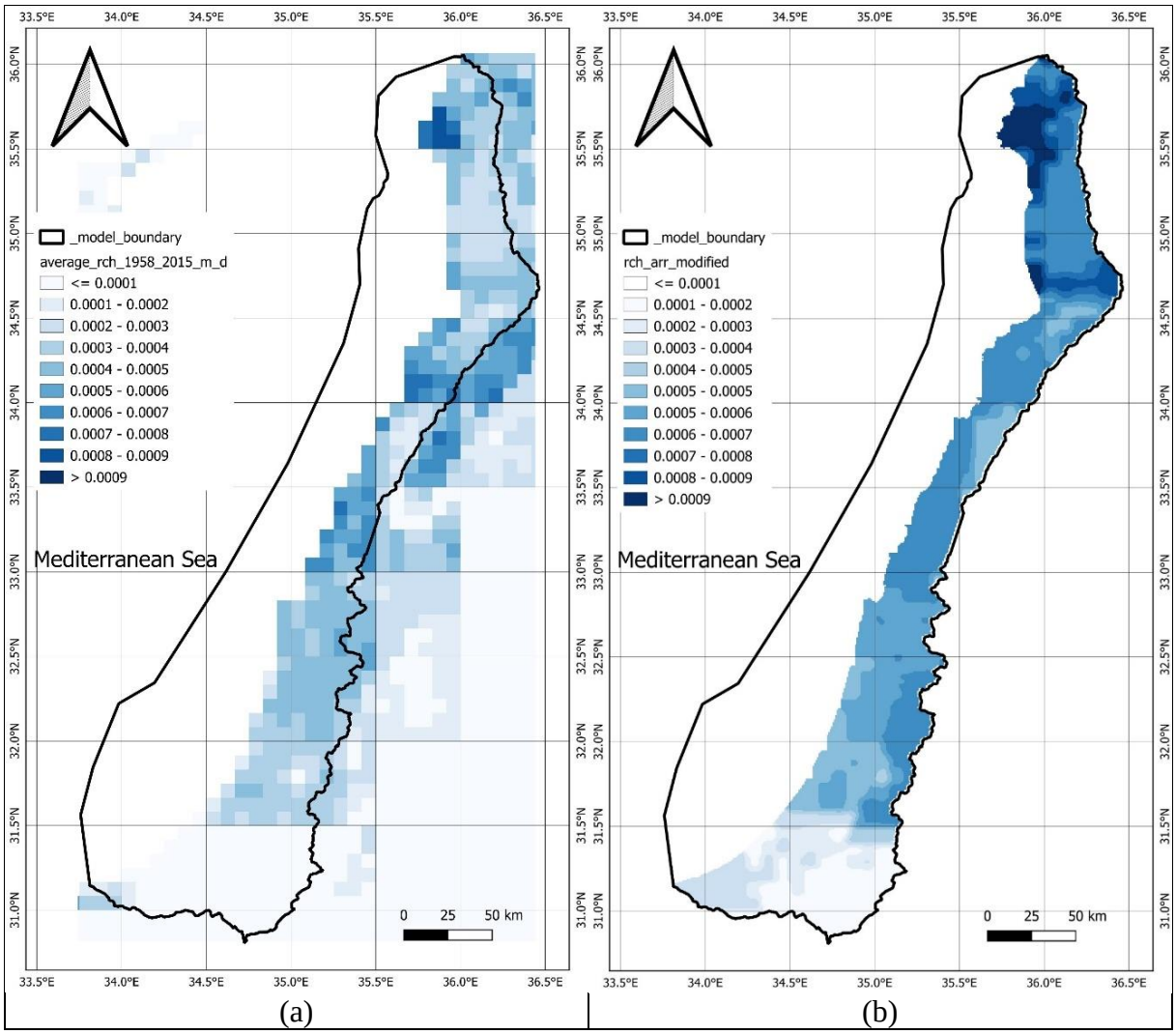

Fig. 19. Average daily recharge for the period 1958 to 2015 (a) PCR-GLOBW global data, and (b) adjusted recharge estimation incorporating some local data

4. Results and Discussion

In this chapter, the results and discussion are presented starting with comparing performances of the alternative models (Lvnt 1, Lvnt 2 and Lvnt 3). Eventually, the results of the best model in terms of accuracy are extensively presented and discussed, in section 4.2.

4.1 Comparison between Alternative Models

In this section of the research, the second and fourth research objectives are fulfilled, while also addressing the first and second research questions. The methodology involves conducting a paleo reconstruction run (30 ka ago) for the three alternative models, followed by the addition of abstraction to simulate the current status of the groundwater system. The primary focus of this section lies in the comparison of the three alternative models in their current status simulations. By executing a detailed analysis of these models, the study aims to shed light on their respective performances and capabilities in representing the present conditions of the groundwater system.

The primary distinction among the three alternative models lies in the LPF (Layer Property Flow) and DIS (Discretization) packages. The Lvnt 1 model was primarily generated using global datasets, as outlined in section 3.4.2.1. The model's vertical domain was segmented into 11 layers based on predetermined percentages, as illustrated in Table 8. Notably, specific cross-sectional views showcasing the hydraulic conductivity distribution across the model layers are depicted in Fig. 20a. Interestingly, this model displays three drops in the model's bottom elevation, leading to an increased model depth. These drops occur when the top elevation corresponds to 0, -150, or -750 meters relative to the present mean sea-level (msl). In terms of hydraulic properties, the first layer of the model exhibits sand-like hydraulic conductivity values (ranging from 2 to 10 meters per day) when the top elevation is above 0 msl, whereas it assumes clay-like properties (ranging from 0.01 to 0.1 m/day) when the elevation is lower than 0 msl.

Considering the LPF and DIS packages of the Lvnt 2 model, a distinct approach was taken. The model's bottom elevation was developed using global datasets, yet adjusted in consideration of local data insights. Unlike Lvnt 1, Lvnt 2 does not exhibit drops in its elevation profile. Instead, the model's depth remains consistent, with a notable emphasis on a thicker representation in the coastal plain zone and the continental shelf, as indicated in Fig. 20b. The model's depth is distributed across 12 layers, structured into four aquifer-aquitard combinations, guided by predetermined percentages, presented in Table 9. This structure yields a strong alignment with local observations, particularly focusing on the coastal zone, as corroborated by Musallam (2021), Qahman & Larabi (2006), and Yechieli & Sivan (2011). The hydraulic conductivity values assigned to these layers are also grounded in local studies.

The LPF and DIS packages of Lvnt 3 were derived from local data, resulting in a model domain divided into 15 layers (sections 3.4.2.3 and 4.2.1). The first 10 layers represent four aquifers separated by three aquitards, characterizing the Quaternary deposit. Additionally, two impermeable layers underlie the initial 10 layers, implying Senonian, Paleocene, and Eocene deposits, while the final three layers represent the Deep Cretaceous Aquifer. Lvnt 3 has significantly greater model depth compared to the other models (up to tenfold offshore). Unlike the other two models, Lvnt 3 encompasses both consolidated and unconsolidated deposits.

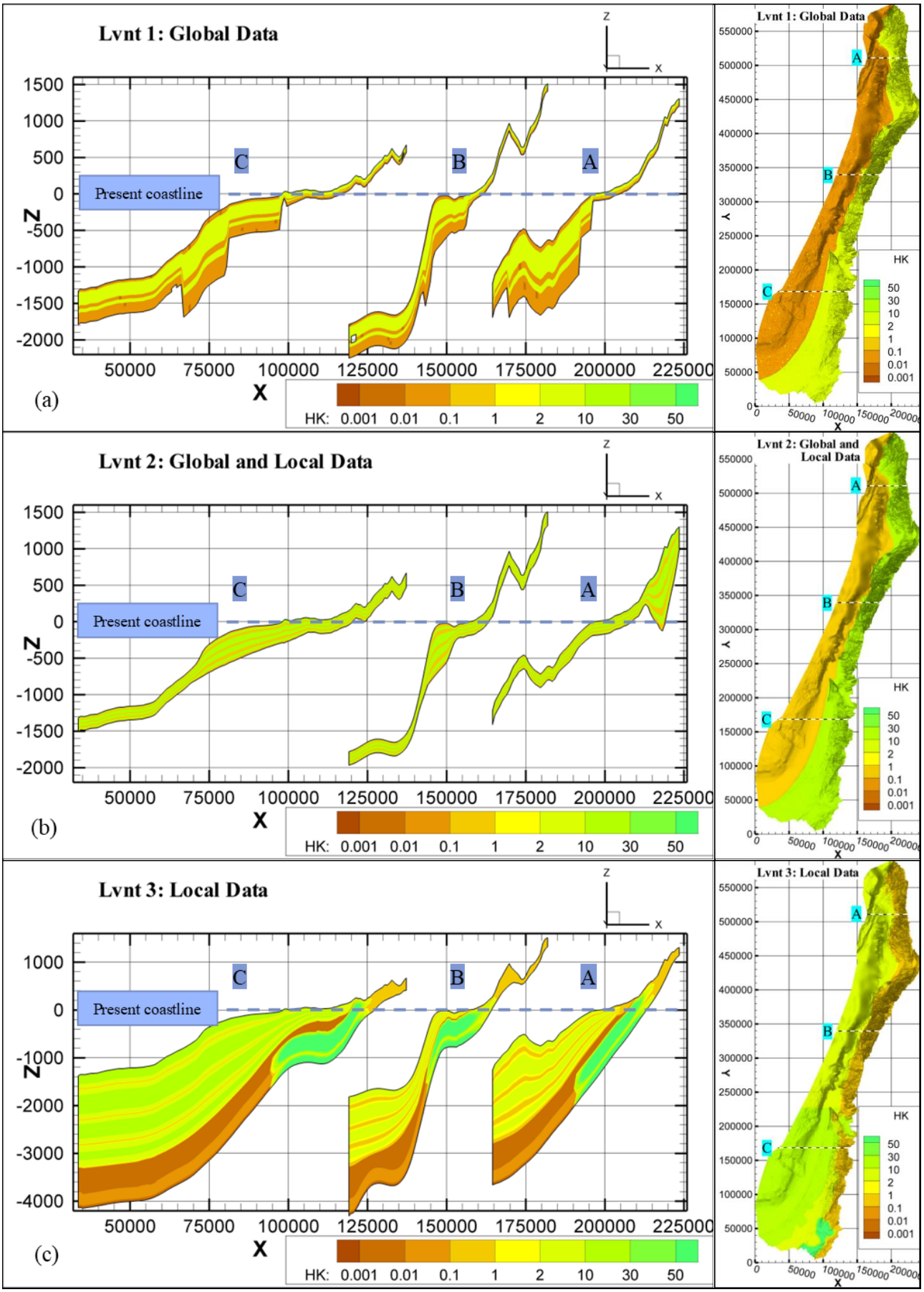

Fig. 20. Hydraulic conductivity and discretization (a) Lvnt 1, (b) Lvnt 2 and (c) Lvnt 3 (notice the scale of z-axis is not the same)

This model's domain discretization is informed by geological interpolation of collected local data, as expounded in section 4.2.1, and the hydraulic properties are computed with reference to local studies as detailed in Table 2. Appendix A.3 provides plan maps of layer thickness and hydraulic conductivities.

Considering the geological and hydrogeological evolution of the study region (as described in section 3.2.1 and depicted in Fig. 6), it is evident that Lvnt 3 exhibits the closest alignment with reality. This conclusion arises from the fact that Lvnt 3 divides the recharge area into two distinct zones. The first zone corresponds to the outcrop of the Deep Cretaceous Aquifer, primarily situated in the mountainous regions and typically occurring when the top elevation surpasses 350 msl. The second zone corresponds to the outcrop of the coastal plain, a characterization applied to the remaining area. Also, in Lvnt 3, there is a thick impermeable aquiclude separating the deep and shallow aquifers. While some alignment, particularly in the coastal plain, can be observed between Lvnt 1 and Lvnt 2 in relation to the hydrogeological conceptual model presented in Fig. 6, the comprehensive and distinct zoning approach of Lvnt 3 positions it as the closest match to the actual geological and hydrogeological conditions.

All the alternative models share the same abstraction rate of approximately 2 million cubic meters per day (MCM/day), as this value is derived from the identical data input sourced from the PCR-GLOBWB global model. However, a notable distinction emerges in terms of recharge between Lvnt 3, and Lvnt 1, and Lvnt 2. This is because the recharge of Lvnt 3 was estimated based on local data as detailed in section 3.4.2.3 whereas Lvnt 1 and Lvnt 2 have constant and uniform recharge value for the whole model area (0.274 mm/day). Remarkably, Lvnt 1 exhibits minimal seawater and freshwater interaction through its IN and OUT GHB, attributed to the presence of drops in bottom elevation, forming hydraulic barriers with low transmissivity along the coastline.

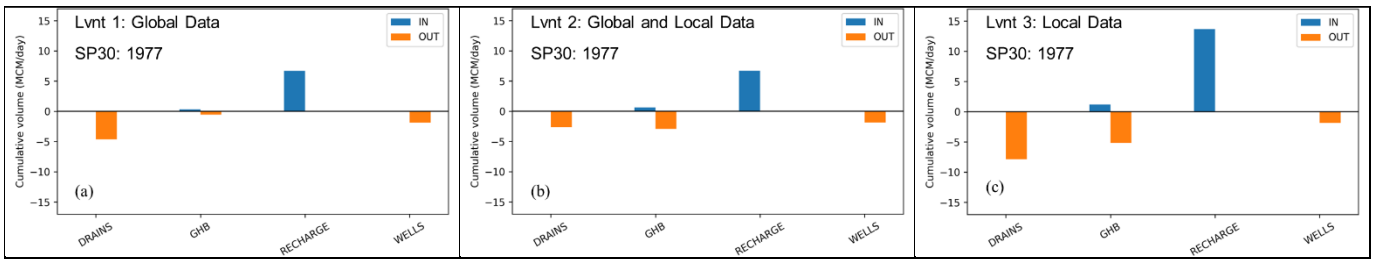

Fig. 21. Water budget for SP30: 1997 of (a) Lvnt 1, (b) Lvnt 2 and (c) Lvnt 3

Notably, a relatively high groundwater table computed in Lvnt 3 (Fig. 22) has the best matching with the observational data (Fig. 24c and Annex 8). In comparison, Lvnt 1 displays elevated groundwater levels in mountainous regions, while Lvnt 2 does not, despite both having the same recharge rate of 0.274 mm/day. This discrepancy suggests relatively higher transmissivity in Lvnt 2, indicative of lower groundwater flow resistance, whereas, in Lvnt 1, the presence of drops in the bottom elevation forms barriers with low transmissive medium.

In Lvnt 1 the highest groundwater table is computed in the southern part which is a desert that has to have low heads but the model receives uniform and constant recharge just like the whole study region and the southern part has the largest area of recharge outcrop. This is where there is overestimation of the head as seen in Fig. 24a. In the coastal plain, Lvnt 1 has the highest estimation for the head due to the existence of the barrier. Lvnt 3 has a significantly high groundwater table gradient, especially in Syria and Lebanon where there is high gradient in the terrains. Although Lvnt 3 has the best matching of observed data (Fig. 24c, observed head between 90 and 250 msl), it underestimated the heads in Latakia Syria in the area where Al-

Kabir Ashamali and Al-Sanobar Rivers feed the groundwater storage (Kinan, 2015). However, the rivers were not simulated in all the alternative models.

Given limited observational data, SP30: 1900 - 1977 was selected as the reference period for evaluating model performances of the alternative models and calibrating Lvnt 3. This choice was motivated by the proximity of available data to that specific time frame, as evident in Annex 8. However, during the calibration process detailed in section 4.2.2, accounting for the temporal variations in data measurements was not feasible due to the computational and time demands for multiple runs of the paleo-reconstruction model. As a result, this variability in data collection timing could not be adequately incorporated into the calibration process.

All the alternative models computed not satisfying TDS (Fig. 23) compared with the observational data (Fig. 24d, e, and f and Table 11). This is because of many causes, as follows:

- Coarse model cell size, e.g. van Engelen et al. (2018) and van Engelen et al. (2021) concluded that it delays the onset of free convection.
- The simplified geology especially the location of the western barrier of the Deep Cretaceous Aquifer as well as not incorporating all the geological major faults.
- The low availability of data observation forced us to consider data from different time domains.
- Initial concentration and boundary conditions, there is salt onshore that has to be considered in the model. Some of it has been there for millions of years produced by evaporation (Hanor, 1994a; Yechieli & Wood, 2002), dissolution of subsurface salts (Hanor, 1994a; Sarkar et al., 1995), fluid convection and hydrodynamic dispersion of salt domes (Hanor, 1994b; Ranganathan & Hanor, 1988), irrigation, and anthropogenic activities (Van Weert et al., 2009).

The assumption of initial freshwater onshore causes the missing agreement with observational data. For example, in the Levant, specifically, the Senonian deposit holds brackish to saline water, ranging from 600 to 11,000 mgCl/l, sourced by prolonged water-rock interaction and paleo seawater trapped during the Pliocene age (Burg & Gersman, 2016; Livshitz, 1997; Rosenthal et al., 1999; Zilberbrand et al., 2014). The presence of ancient intruded salt was reported also in previous groundwater models. For example, Delsman et al. (2014) and Meyer et al. (2019) found pre-Holocene saltwater in Dutch and Danish coastal groundwater systems respectively, originating from prior geological ages, and simulations by Zamrsky et al. (2020) suggested the prospect of trapped saltwater from past interglacial periods.

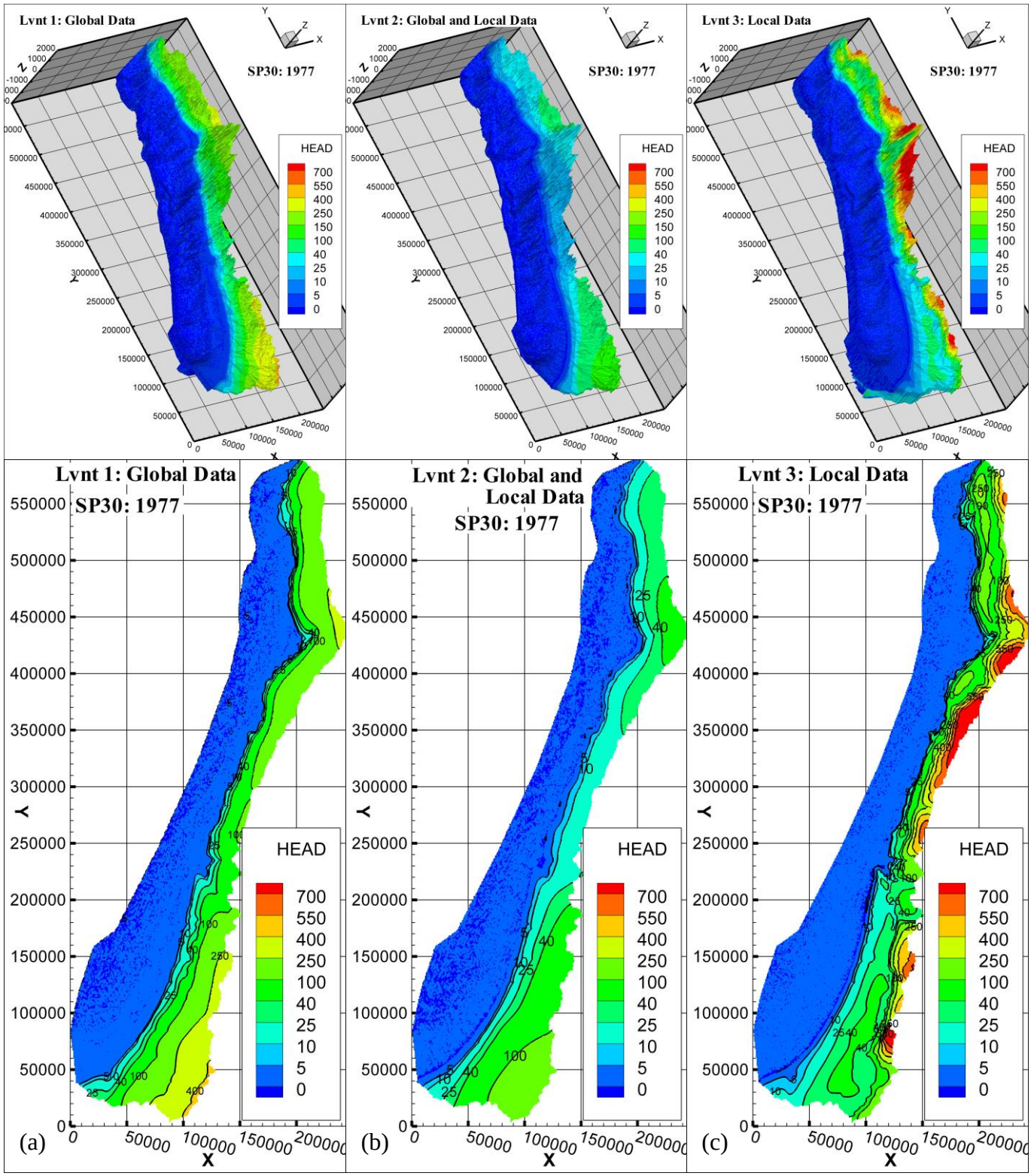

Fig. 22. Modelled groundwater table with the terrain for SP30: 1977 of (a) Lvnt 1, (b) Lvnt 2 and (3) Lvnt 3

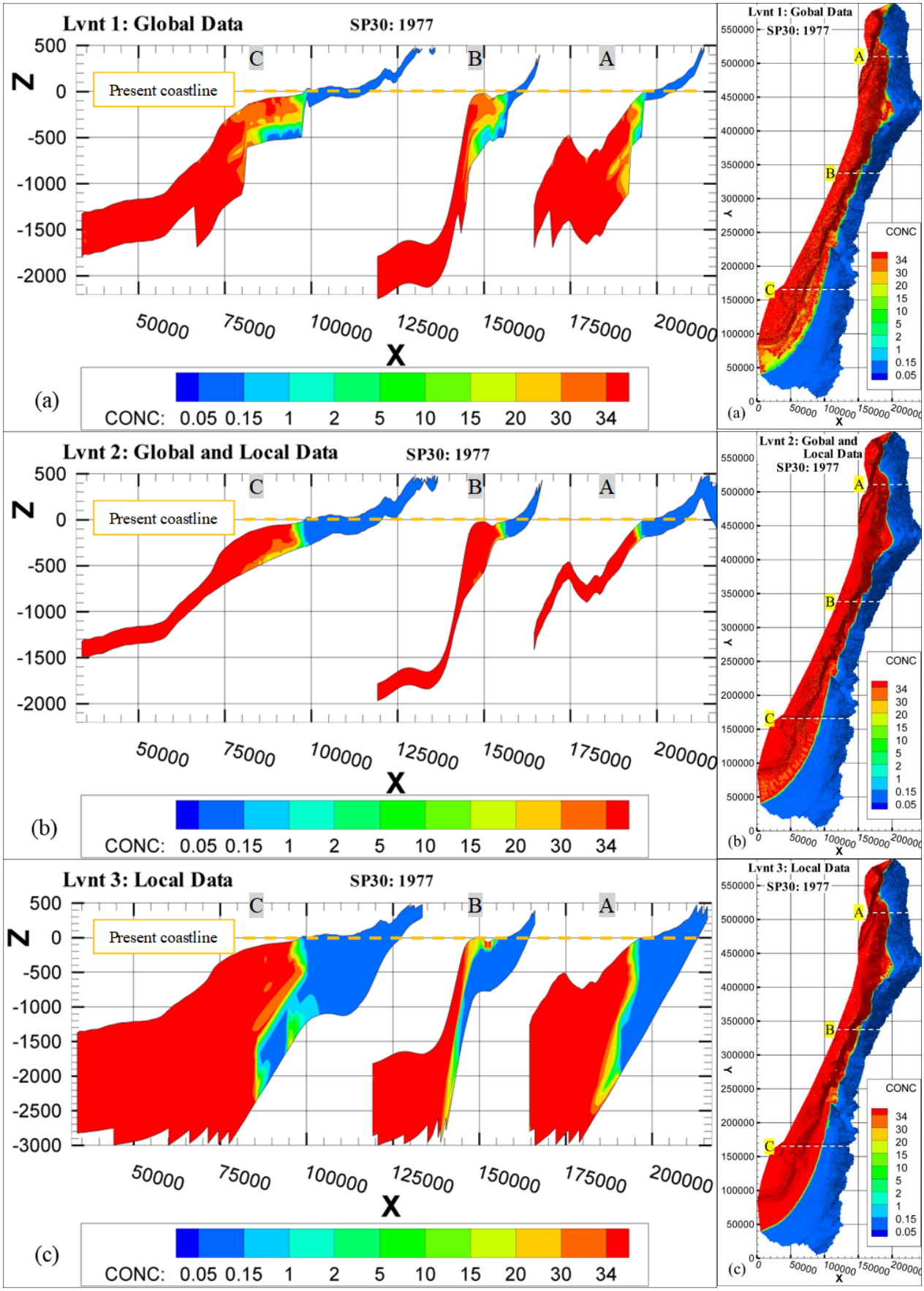

Fig. 23. Cross sections of the modelled TDS for SP30: 1977 of (a) Lvnt 1, (b) Lvnt 2 and (3) Lvnt 3 (notice the scale of z-axis is not the same)

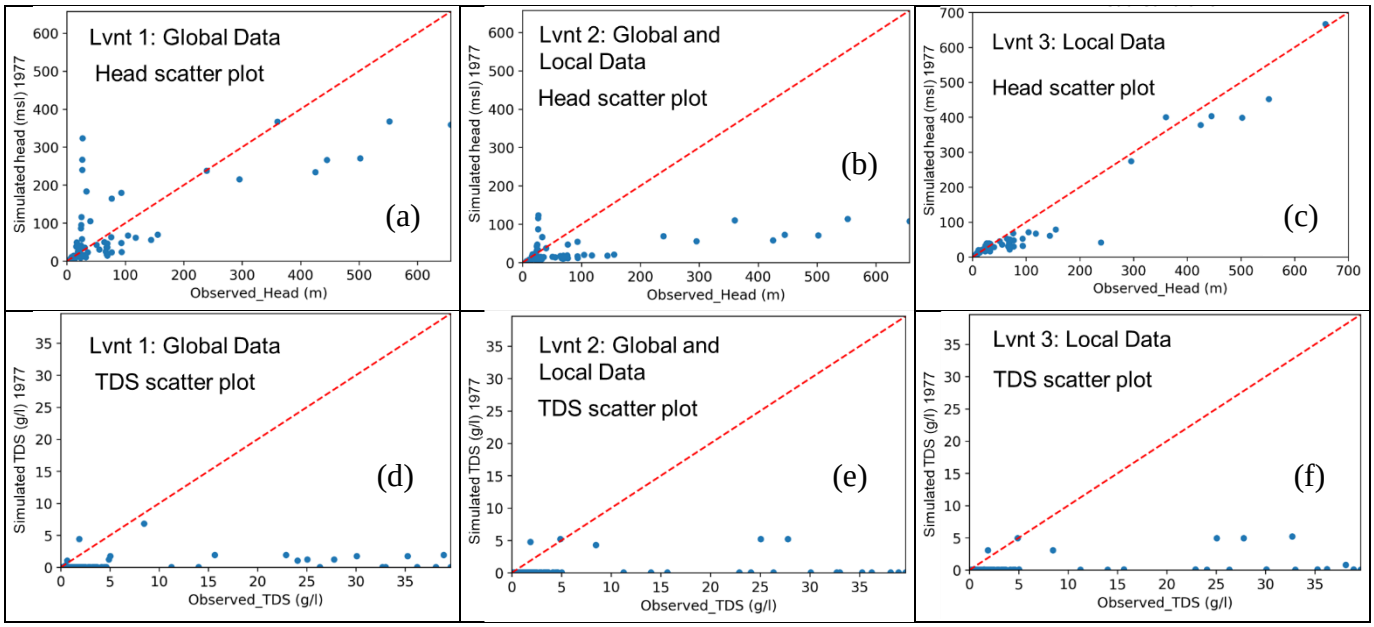

Fig. 24. Scatter plot for observed head vis computed head for (a) Lvnt 1, (b) Lvnt 2 and (c) Lvnt 3 and observed TSD vs computed TDS (location of observational data is attached in Annex 8)

Drawing insights from a limited number of localized studies and applying them across a supra-regional model often leads to unfavourable outcomes, illustrated by Lvnt 2's elevated head RMSE of 133.19 msl, as indicated in Table 11. The importance of incorporating well-distributed spatial studies for improved model accuracy becomes evident in this context. Remarkably, Lvnt 3 stands out as the model with the highest reliability, achieving a head RMSE of 38.78 msl.

The solution of the advection-dispersion equation introduces discretization complexities to adhere to Courant number limitations, elucidated by Oude Essink (2003). The commendable quickness of computation times across all alternative models (ranging from 7.5 to 14.5 hours) can be attributed to the effective integration of scripted procedures. These procedural measures efficiently restrain excessive groundwater flow velocities, thus mitigating the necessity for small numerical time steps that might elongate calculation times. While some manual adjustments are requisite during the model's formulation, the approach markedly expedites the model-building process. Noteworthy is Lvnt 1's reliance on global datasets, resulting in the fastest package creation time, while Lvnt 3 necessitates a longer duration due to the incorporation of geological interpolation within the model.

In terms of reproducibility, the model's construction is entirely scripted within a reproducible workflow enhancing the existing toolbox of the GCGM. This well-defined framework not only streamlines potential future updates to the Levant region's groundwater flow and salt transport model but also ensures the traceability of methodology and results. Finally, based on the findings of this section, it was decided to make further analysis of the results of Lvnt 3 in the next section.

Table 11: Test the performance of the alternative models

Model	Lvnt 1	Lvnt 2	Lvnt 3
Head RMSE (msl)	90.93	133.19	38.78
Concentration RMSE (g TDS/l)	9.33	9.40	9.28
Required time to create packages	Low	Medium	High
Required time for 30 ka paleo running	12 hours	7.5 hours	14.5 hours
Reproducible	Yes	Yes	Yes

4.2 Lvnt 3: Model Analysis

4.2.1 Geological interpolation

There are not 3D geological measurements (borelogs) to build the geological model for the Levant so the researcher relied on collecting information from previous studies and making assumptions in their light. The references of the collected data are mentioned in sections 3.2.1 and 3.4.2.3. The geological interpolation was conducted in 3 stages which are initial interpolation, postprocessing and adaption for the numerical model.

The first stage was conducted using Geoscience ANALYST software, executed by Jude King using his tools (Deltares), using hard georeferenced data that were collected by the researcher. Unfortunately, the interpolation did not have the best matching with the real situation because of the spareness of data in such a supra-regional scale and lack of data e.g., there is only one borelog in the Syrian part and no borelogs in the mountain area of Lebanon. The outcome of the first stage of the geological interpolation is presented in Fig. 25a.

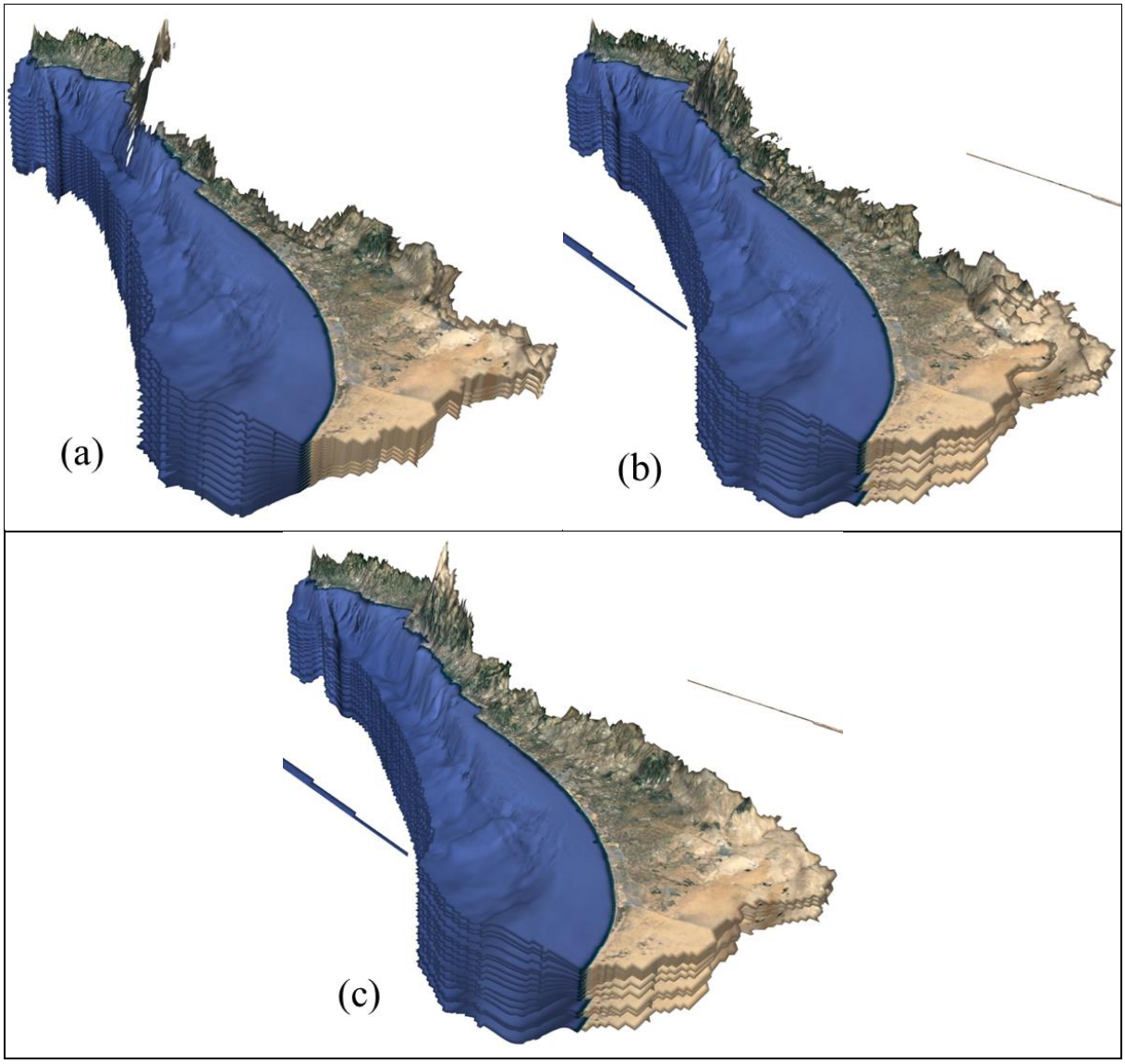

Fig. 25. 3D view of the geological interpolation of (a) first (b) second and (c) third stages

At the end of the first stage, it was concluded that the postprocessing stage is necessary using soft data to guide the interpolation. The main focus was correcting the model bottom elevation and then correcting the other layers relative to it. This stage started with filling the no-data cells (Fig. 26a) inside the model boundary to get model total thickness equal to 350 m. The total thickness of the model was restricted to between 350 and 3000 m. Gradual reduction of the total model thickness was performed in the mountainous area to reach 100 m in the summits. Next, local corrections were conducted using the soft data e.g. overestimation of the total thickness was observed in Syria so it was reduced gradually to reach realistic thickness as well as underestimation was observed in Lebanon the model was too thin. After correcting the model bottom elevation (total thickness), the other layers were added according to the estimated thickness in the first stage with minimum and maximum limits based on the soft data. Exposing the recharge outcrop of the Deep Cretaceous Aquifer was also taken into account. The outcome of the second stage is shown in Fig. 25b and Fig. 26b.

The third stage was performed for numerical modelling purposes. Since the layers discretization following the topograph approach was used, MODFLOW does not accept zero thickness layers, it causes model convergence issues. Thus, a thin thickness (2 to 5 m) was fabricated for each layer in the area where the Deep Cretaceous Aquifer is exposed (Fig. 25c). Later, the fabricated thicknesses were given the original layer hydraulic properties as seen in Fig. 20c.

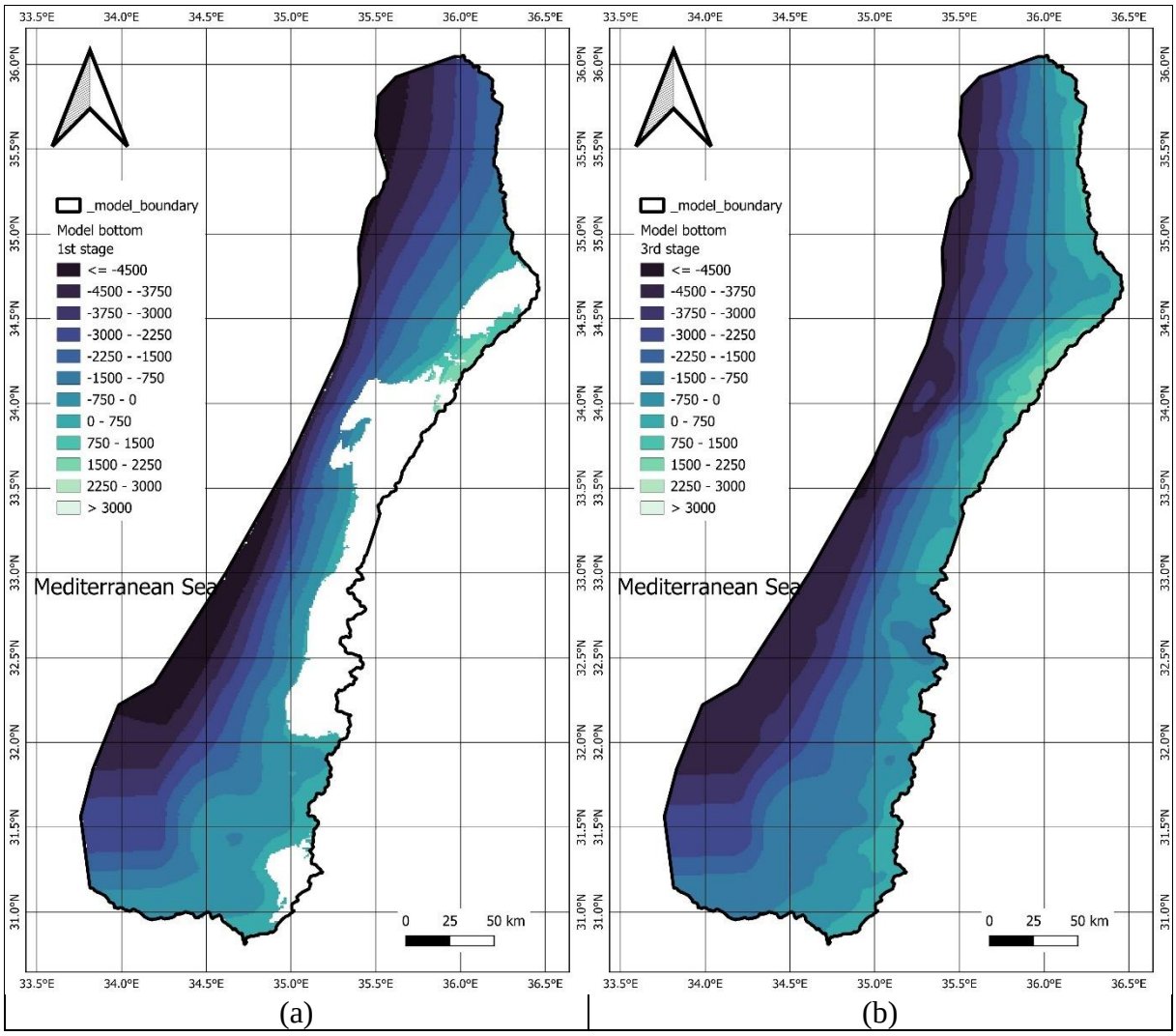

Fig. 26. Model bottom elevation of (a) the first stage and (b) the second and third stages of the geological interpolation

4.2.2 Model Calibration

The parameters of hydraulic conductivity and recharge were considered during the calibration of Lvnt 3. Hydraulic conductivity was calibrated using data from local studies as summarized in Table 2. The resulting hydraulic conductivity values for each layer are illustrated in Figure S 9 and Figure S 10. Initially, recharge was assigned based on estimates from the PCR-GLOBWB global model (Fig. 19a). However, it was concluded that this estimation led to low head values, particularly in mountainous regions. To address this, adjustments were performed using available local data from Table 3. Given that these local data span a limited time frame, an assumption was made to generalize the local recharge data across the entire current status model period spanning from 1900 to 2015, assuming constant recharge in terms of time variation. The adjusted recharge estimation is presented in Fig. 19b. During the calibration process, a comparison with observational data was conducted through scatter charts (Fig. 24c and f), with the primary focus on calibrating the groundwater head. However, due to the limitations discussed in section 4.1, the calibration of concentration was not executed effectively.

The data availability in Syria and Lebanon, particularly regarding hydrogeological properties, groundwater head, and concentrations, is notably limited, especially in mountainous areas. Consequently, during this phase of the study, certain assumptions were necessary, including borrowing calibrated parameters from the Palestinian mountainous region. For the coastal plain of the Levant, observation data for groundwater heads at specified depths were scarce, with only 25 points concentrated in Latakia and 8 points in Tripoli. In response, soft data such as head contour maps were utilized in other areas (Appendix A.1 and Annex 8). Ultimately, RMSE for Lvnt 3 is 38.78 meters msl for groundwater head and 9.28 g TDS/l for concentration.

4.2.3 Paleo-Hydrogeographical Model

The paleo-hydrogeographical model was developed in order to investigate the effect of sea-level change over 30,000 years ago on the present groundwater conditions using the groundwater indicators (change in submarine groundwater discharge, water budget, paleowater, saltwater intrusion, groundwater depletion, and fresh groundwater volume). In addition, the purpose of the paleo-hydrogeographical model is to generate the initial salinity distribution of the current status model with the addition of groundwater abstraction.

The water budget components of the paleo reconstruction period are drainage, GHB (sea) and recharge (Fig. 27). The water budget of all stress periods is attached in Figure S 11. The lowest recharge record coincides with the most recent sea-level of 0 msl which is the highest sea-level throughout the reconstruction period (transgression process) leading to less land (surface area) that receives recharge. On the other hand, the highest recharge record corresponds to the lowest sea-level BP16000 at sea-level -120 msl. The lower the sea-level, the higher OUT GHB due to the increasing hydraulic gradient and the geological nature (Fig. 20c). Hence, the same stress period also exhibits the lowest drainage record. In all stress periods, the IN GHB remains relatively very low because of the high recharge with no abstraction as well as the low permeability of the deep layers in the offshore part (Fig. 20c).

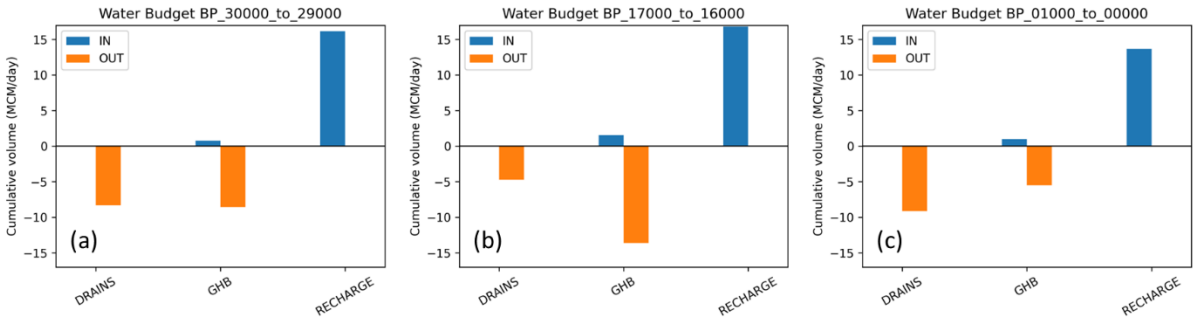

Fig. 27. Water budget of paleo-hydrogeographical model (Lvnt3), for (a) SP0: BP29000, (b) SP13: BP16000, and (c) SP29: BP00000

Fig. 28 exhibits the submarine groundwater discharge in the offshore part (seabed) in red while the blue color refers to saltwater intrusion. The concentrated red color along the coastline represents the submarine springs phenomena in the Levant, mentioned in section 3.2.2 and shown in Fig. 29. The cause of this discharge is the geological nature as seen in Fig. 29 and the sharp slope of the seabed bathymetry (Shaban, 2020). In accordance with the water budget, the highest and most dense submarine groundwater discharge is observed in SP13 when sea-level was -120 msl since it records the highest OUT GHB.

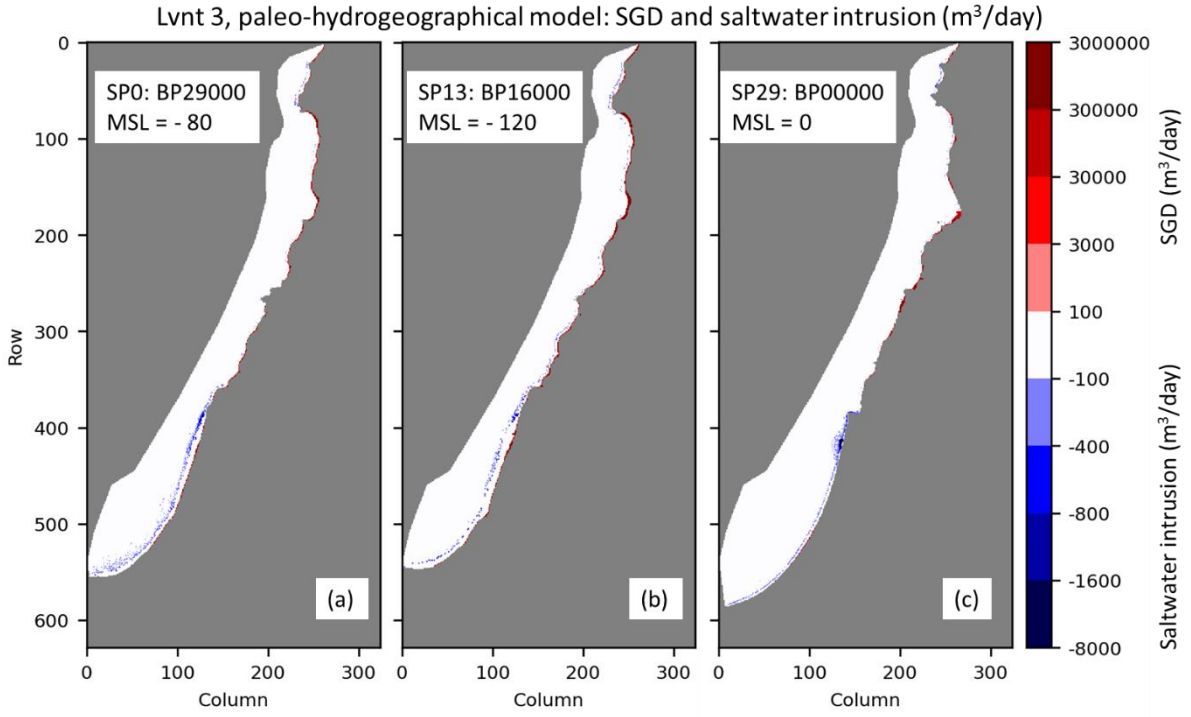

Fig. 28. Submarine groundwater discharge (SGD) and saltwater intrusion (m^3/day) for (a) SP0: BP29000, (b) SP13: BP16000, and (c) SP29: BP00000. SGD = GHB conductance × (computed head – sea-level) when computed concentration ≤ 1 g/l and computed head > sea-level. Saltwater intrusion = GHB conductance × (computed head – sea-level) when computed head < sea-level

Fig. 29. Schematization of the submarine springs phenomena in the Levant (clipped part of Fig. 6)

Fig. 30 displays the fraction of drainage over recharge which represents the surface water extraction from groundwater. This extraction may happen in the form of springs or river feeding, occasional springs. The highest and densest drainage network is noticed in SP29: BP00000 which is along with the low submarine groundwater discharge due to the low hydraulic gradient.

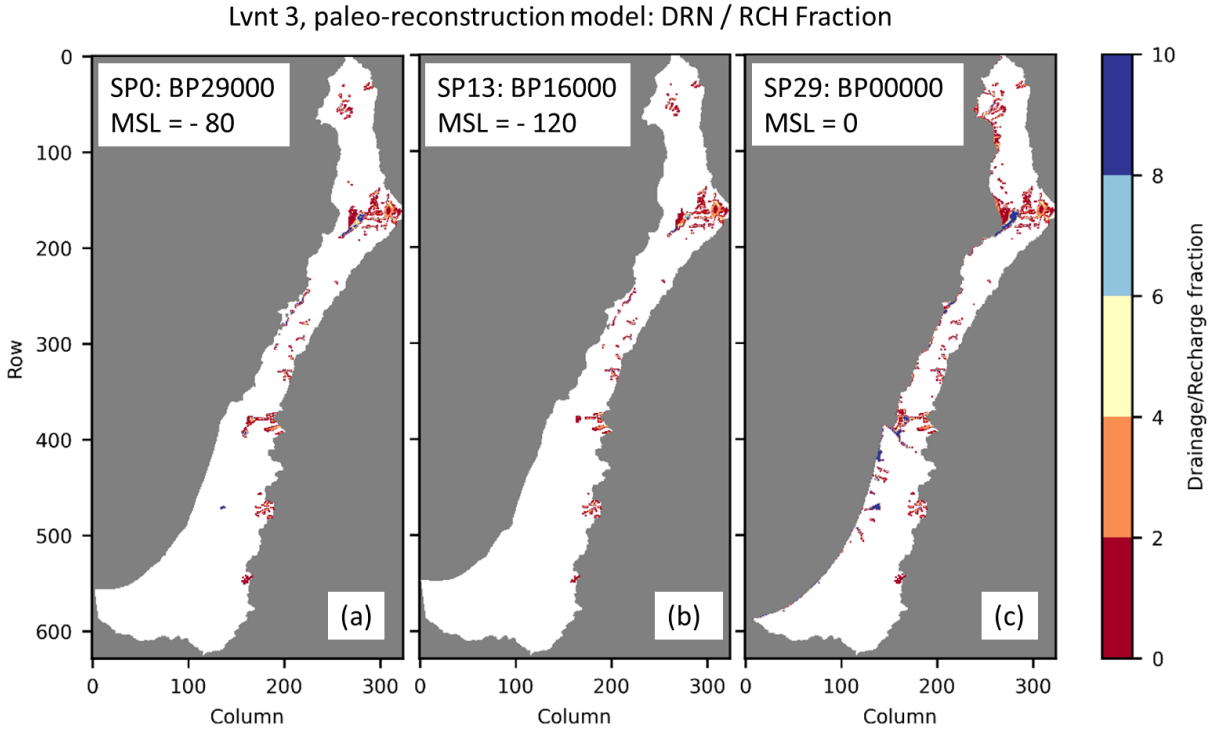

Fig. 30. Drainage / recharge (Fig. 19b) fraction for (a) SP0: BP29000, (b) SP13: BP16000, and (c) SP29: BP00000 (white colour means zero drainage)

The modeled groundwater head reveals distinct observations. The most significant head gradient is seen during BP16000, corresponding to a sea-level of -120 meters below mean sea-level (msl). Moreover, lower heads are evident during BP30000 and BP16000 in coastal regions compared to the more recent head of BP00000. This lower head is attributed to the reduced sea-level, reinforcing the relatively elevated submarine groundwater discharge (Fig. 28). The increased submarine groundwater discharge is not solely due to the heightened hydraulic gradient but also stems from the enhanced transmissivity linked to the greater depth of the groundwater system, leading to a larger saline-freshwater interface. This expanded interface is a result of geological interpolation (Fig. 20c). On the contrary, in mountainous areas, little

difference across the three stress periods is observed (Fig. 34), as the groundwater head remains consistently above 250 msl. This could be due to the distance from the coastline, where the only varying parameter among the different periods in the paleo-hydrogeographical modeling is the changing sea-level over time.

Regarding the modelled concentration (g TDS/l), a relatively thin transition zone is detected in BP29000 (Fig. 32a cross section A and C) due to the initial salinity characteristics of this stress period, which marks the onset of the warming up period. As explained in section 3.4.1, during this period, when the top elevation is higher than the sea-level, all model cells are considered freshwater and vice versa. However, Fig. 32a cross section B shows an opposite result, the thick transition zone may be related to the very thin two overlaying impermeable layers which are marl and chalk (Fig. 20c) with a total thickness of about 10 m. On the other hand, the thickness of the Deep Cretaceous Aquifer is about 800 m with hydraulic conductivity reaching 250 m/d facilitating significant advection and dispersion processes in this zone. Additionally, the relatively steep slope of the continental shelf could contribute to this phenomenon.

In contrast, following a sea-level decrease of 80 to 120 meters below present msl over a span of 13,000 years, the transition zone exhibited increased thickness (Fig. 32b). This occurrence could be attributed to the previously mentioned high submarine groundwater discharge. Another factor contributing to the expansion of the transition zone is the combination of seawater and freshening due to sea-level reduction, leading to the entrapment of saltwater in this area along with the influence of diffusion processes.

Focusing on the most recent stress period BP00000, paleowater can be observed in Fig. 32c where the water remains fresh after the increase of the sea-level to 0 msl. In Fig. 33, Point 3 maintains its freshwater concentration for the whole modelling period whereas point 1 and 2 starts with seawater concentration (29 ka ago) but experience freshening process because of the sea-level decrease till eventually, they transit to freshwater from 21 ka ago to the present. Cells like point 1, 2 and 3 could be considered paleowater since it maintains freshwater for thousands of years even after the sea-level rise despite being situated in the offshore part.

Fig. 32c section C displays an unusual shape of the transition zone, with freshwater underlying saltwater. This phenomenon is primarily attributed to the significant influence of advection and dispersion processes caused by the Binyamina fault, as elaborated upon in section 3.2.1. The saltwater intrusion is seen in Fig. 28, particularly in the fault location (visualized in red), notably in SP29: BP00000. The Binyamina fault was incorporated into the model by designating certain cells with high hydraulic conductivity (reaching up to 250 m/day) (Figure S 9), enabling extensive interaction between seawater and freshwater, resulting in saltwater intrusion. Point 4 in Fig. 33 exhibits a severe saltwater intrusion when the sea-level exceeds 0 msl. However, the underlying freshwater remains unaffected as it is considered paleowater situated within a medium characterized by very low hydraulic conductivity (0.001 m/day), as evident in Fig. 33, point 3. Similar findings have been reported by Bar Yosef (1978), Mandell et al. (2003) and Mercado, (1980). However, Paster et al. (2006) hold a different viewpoint, contending that the deep aquifer and the sea are not interconnected due to their observation that the head of the saline water is lower than the sea-level.

As sea-levels rise, a clockwise rotation of the sea-freshwater interface is observed, leading to an odd positioning of the saltwater wedge, as depicted in Fig. 32c. Contrary to the expected behavior dictated by the Badon Ghijben-Herzberg principle (Badon-Ghyben & Drabbe, 1889; Herzberg, 1901), the lateral encroachment of fresh water extends further towards the sea with increasing depth. This could be attributed to the relatively high hydraulic conductivity (10

m/day) of the coastal plain aquifers, which allows for faster saltwater intrusion compared to the slower-moving low hydraulic conductivity deep layers (0.001 m/day), where freshwater remains as paleowater, see Fig. 20c. Additionally, the presence of submarine groundwater discharge, particularly in cross sections A and B, may contribute to this occurrence. The existence of thick layers with low hydraulic conductivities within the geological model results in a decelerated movement of saltwater, necessitating more time for saltwater to permeate the deeper parts of the groundwater system through diffusion processes (Kooi et al., 2000; V. E. A. Post et al., 2013).

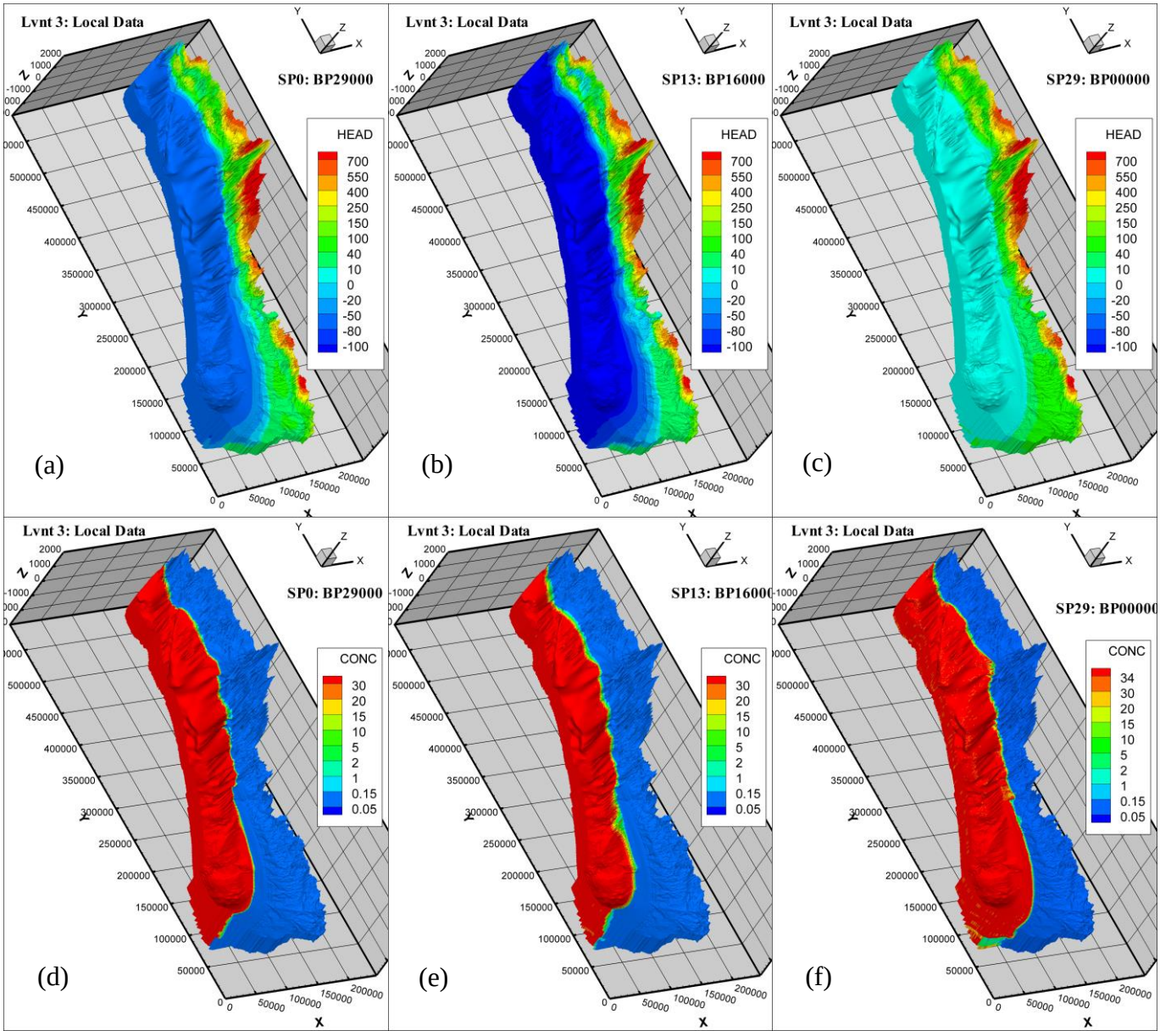

Fig. 31. Modelled head for (a) SP0: BP29000, (b) SP13: BP16000, and (c) SP29: BP00000, and modelled concentration (TDS) (d), (e), and (f) for the same stress periods

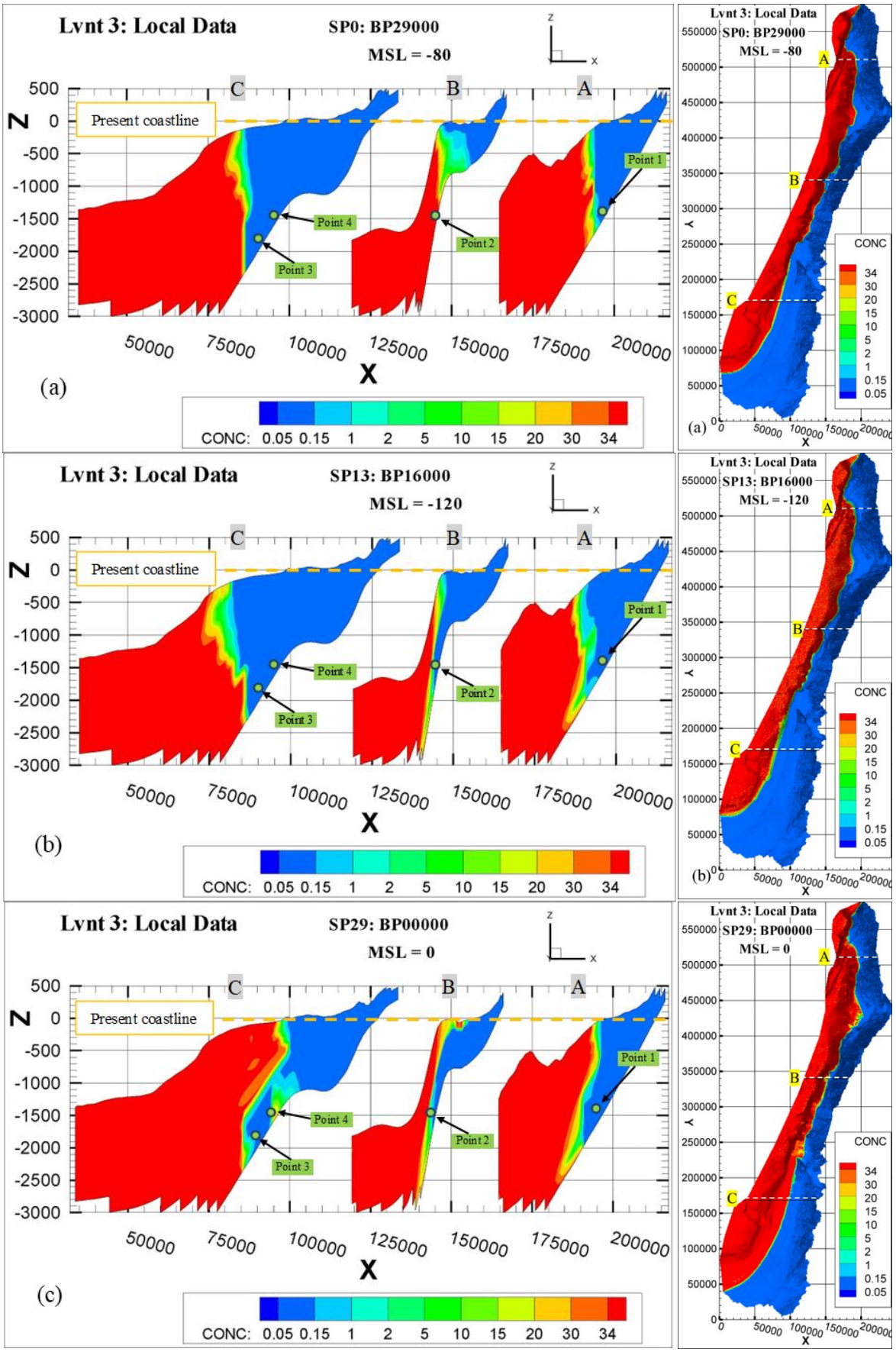

Fig. 32. Cross sections of the modelled concentrations (g TDS/l) for (a) SP0: BP29000, (b) SP13: BP16000, and (c) SP29: BP00000

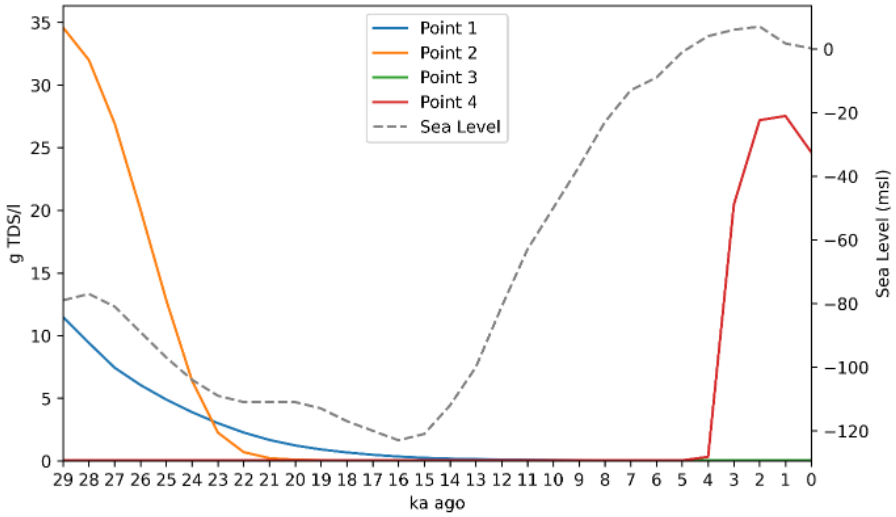

Fig. 33. Modelled TDS of selected cells with sea-level change, locations are indicated in Fig. 32a

Fig. 34 presents the groundwater table depletion through a comparison between SP0 and SP13 as well as SP0 and SP29. Positive values (red) signify depletion, indicating a decrease in the groundwater table and vice versa. Despite the substantial increase in fresh groundwater volume due to the decrease in sea-level during BP16000 (Fig. 35), this period experiences the most severe groundwater table depletion, notably exceeding 40 meters in the coastal zone. By contrast, the lowest fresh groundwater volume is recorded in BP00000 coinciding with the highest water table rise reaching more than 80 m higher than the groundwater table in BP16000. The low groundwater table in BP16000 explains its lowest drainage discharge in Fig. 30b and Fig. 27b.

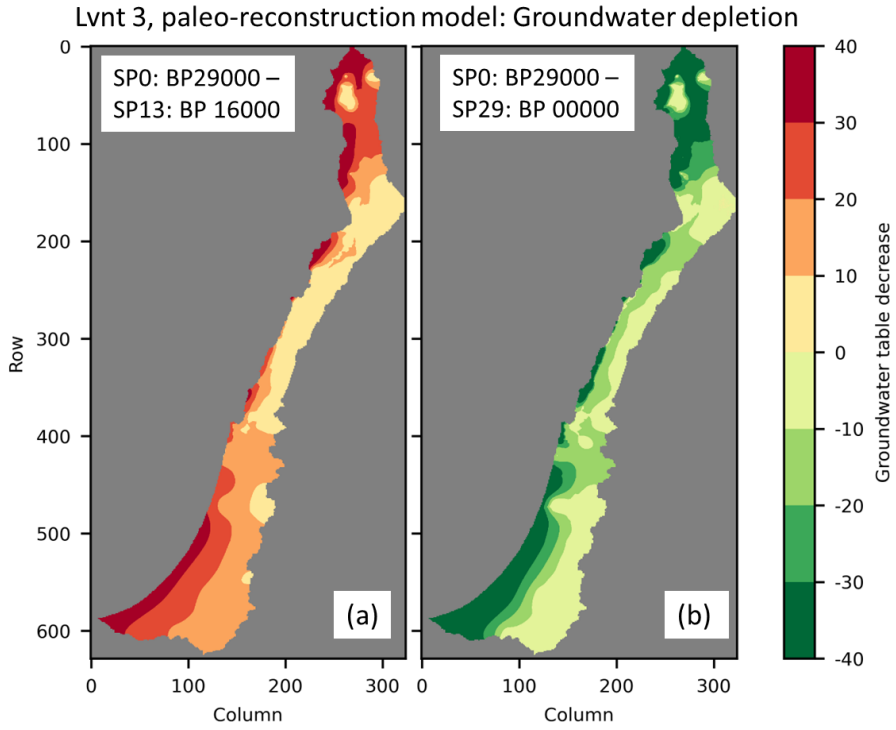

Fig. 34. Groundwater depletion represented in groundwater table decrease for (a) SP0: BP29000 – SP13: BP 16000, and (b) SP0: BP29000 – SP29: BP 00000

During the regression period, a gradual process of freshening is observed, resulting in a steady increase in the volume of freshwater (TDS ≤ 1 g/l) from 9 (10^{12} m^3) to its peak at 9.7 (10^{12} m^3). In contrast, the transgression period witnesses a notable reduction in fresh groundwater volume, nearly halving to less than 4.7 (10^{12} m^3) at the recent sea-level. This decline in fresh groundwater volume is attributed to the horizontal landward shift of the sea-freshwater transition zone, coupled with the salinization caused by various vertical downward salt movements from the sea floor (V. E. A. Post et al., 2013). Comparing the freshening and salinization processes, the volume of freshwater during the regression period is significantly less compared to the transgression period. For instance, the fresh groundwater volume when the sea-level is -81 msl BP27000 (regression) amounted to 8.7 (10^{12} m^3), whereas it is 9.4 (10^{12} m^3) when the sea-level is -81 msl BP12000 (transgression), as seen in Fig. 35a. This is maybe attributed to the initial salinity distribution of the model (which is a warming up period) in addition to the high recharge with high hydraulic conductivity in the shallower system resulting in huge OUT GHB as well as the special condition of geology which led to reserving paleowater. OUT GHB exhibited a similar pattern, with 8.5 (10^6 m^3/day) during the sea-level of -81 msl BP27000 (regression) and 10.1 (10^6 m^3/day) during the sea-level of -81 msl BP12000 (transgression), as seen in Fig. 27.

The fresh groundwater volume follows the pattern of sea-level with more than thousands of years delay (lag) especially during the transgression period as shown in Fig. 35a. The delay is mainly related to the low-permeable layers in the deepest parts of the Levant which have groundwater memory of several thousands of years (Kooi et al., 2000; Post & Kooi, 2003). Similar findings were reported by Van Pham et al. (2019) and Goofers (2020). A linear correlation between the sea-level rise and the fresh groundwater volume during the transgression period is shown in Fig. 35b. The R^2 is 0.99 indicating a strong linear correlation which helps in the further application of predicting the effect of future sea-level changes on fresh groundwater volume in the Levant. Overall, achieving dynamic equilibrium is relatively more feasible during transgression compared to regression, aided by the time it takes for this equilibrium to be established (Mulder, 2018).

The solute mass (in kg TDS) is the cumulative sum of solutes present in all active cells. The solute content experiences a rapid escalation during the sea-level rise in the transgression period. This increase in solute content follows a similar delayed pattern as observed in the decline of fresh groundwater volume, stemming from the factors mentioned earlier. An interesting observation is the inverse relationship between the solute content pattern depicted in Fig. 35a and the pattern of fresh groundwater volume in response to sea-level changes.

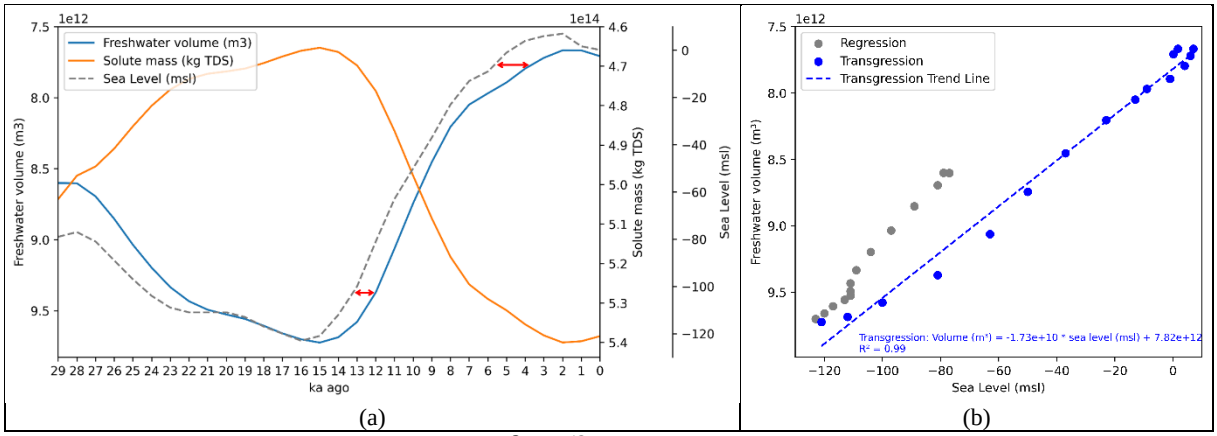

Fig. 35. (a) Fresh groundwater volume (m^3× 10^{12}) and solute mass (kg TDS) of Lvnt 3 along the paleo reconstruction period (30,000 years) in comparison with sea-level change, and (b) Correlation between sea-level change and fresh groundwater volume

4.2.4 Current Status Model

The current status model was established using the result of salinity distribution obtained from the final stress period of the paleo-reconstruction model (BP00000), serving as a reference model in the analysis. In this model, the groundwater abstraction was incorporated for the period 1900 to 2015 using the PCR-GLOBWB global model, detailed in 3.2.4. The simulation period was divided into 3 stress periods (1900 to 1977, 1978 to 1997 and 1998 to 2015).

The water budget analysis (depicted in Fig. 36) reveals consistent recharge patterns over time, while groundwater abstraction shows gradual growth to reach about 4 MCM/day which has a good match with (Quba'a et al., 2018) estimated the abstraction to be 3.3 MCM/day. This trend resulted in a minor decrease in OUT GHB and drainage. Consequently, OUT GHB values for the seabed in the stress periods 1900 to 1977, 1978 to 1997, and 1998 to 2015 appear relatively similar in Fig. 37. However, slight differences can be observed between these stress periods, particularly with regard to drainage (illustrated in Fig. 40), primarily in the mountainous areas of Syria and Lebanon.

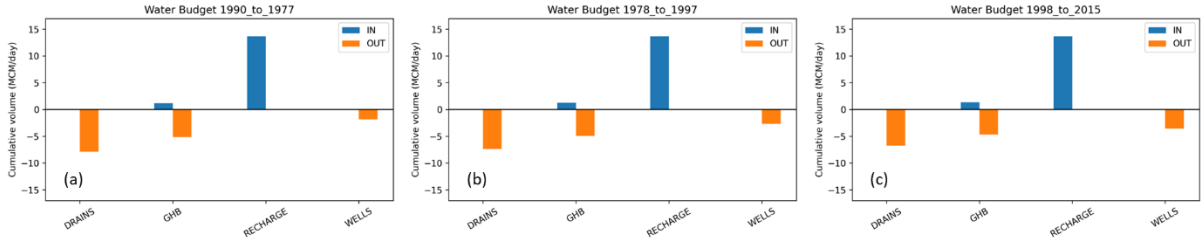

Fig. 36. Water budget of current status model (Lvnt3), for (a) SP30: 1977, (b) SP31: 1997, and (c) SP32: 2015

In general, the southern coast of the Levant experiences relatively reduced submarine groundwater discharge and elevated saltwater intrusion compared to the northern coast, as depicted in Fig. 37. This is attributed to the lower recharge (Fig. 19) and higher abstraction (Fig. 9) in the southern onshore region of the Levant as well as the existence of Binyamina fault and the hydrogeological properties of the model layers (Figure S 9).

A considerable portion of the submarine groundwater discharge is released in the continental shelf of Lebanon and Syria in the shape of submarine springs as freshwater. This is attributed to the seabed bathymetry, hydraulic gradient and geological nature as detailed in section 4.2.3 and Fig. 29. The complexity of karstification results in high variation in the interaction between the groundwater and surface water (Al-Charideh, 2004). Thus, quantitative comparison between the observation and modelled data may not be feasible, in particular in such a coarse cell size model. However, good spatial matching can be concluded from the observation in Fig. 38, Fig. 39, and Figure S 5b.

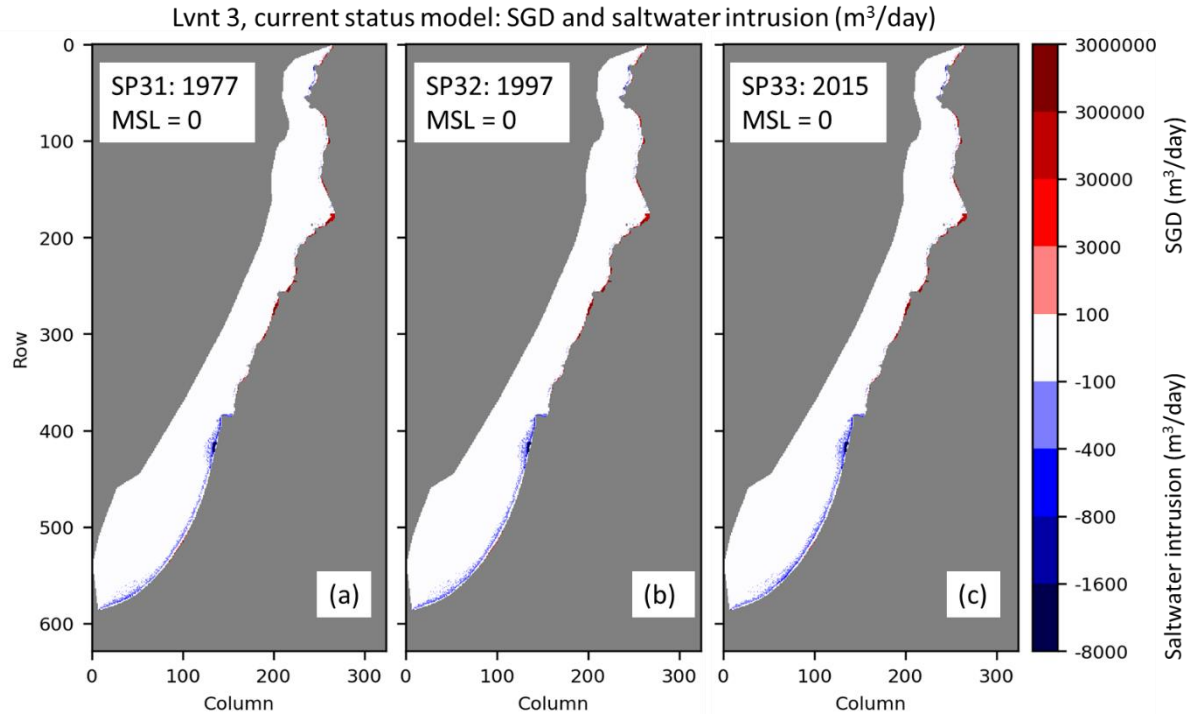

Fig. 37. Submarine groundwater discharge (SGD) and saltwater intrusion (m^3/day) for (a) SP30: 1977, (b) SP31: 1997, and (c) SP32: 2015. SGD = GHB conductance × (computed head – sea-level) when computed concentration ≤ 1 g/l and computed head > sea-level. Saltwater intrusion = GHB conductance × (computed head – sea-level) when computed head < sea-level

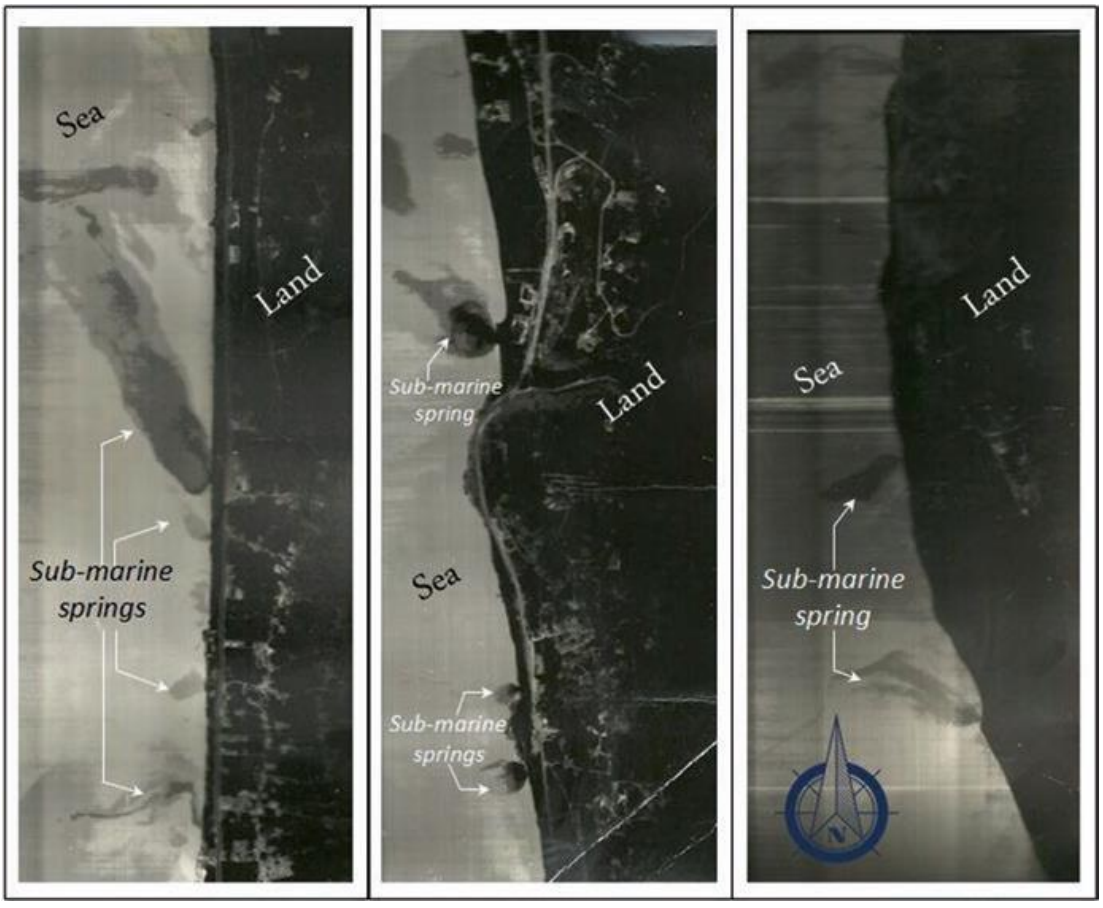

Fig. 38. Thermal maps of example submarine springs in Lebanon (Shaban, 2020)

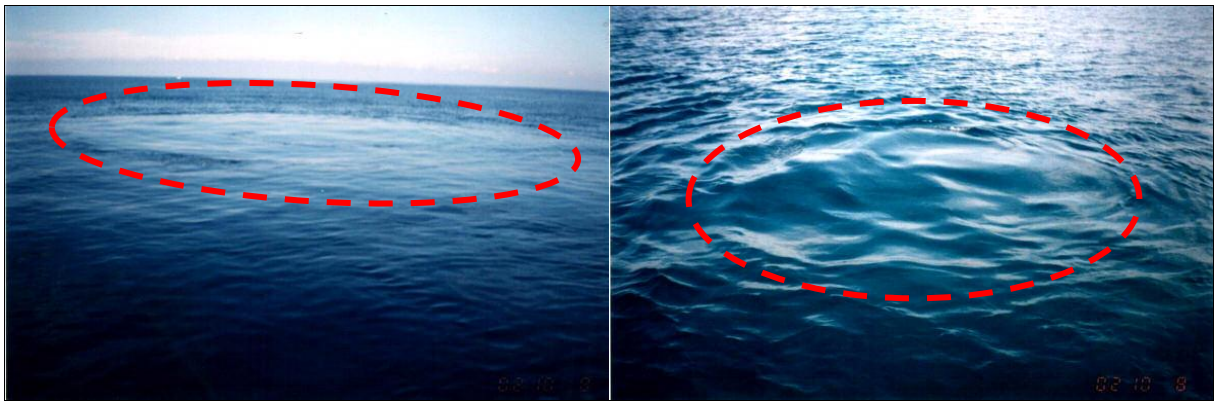

Fig. 39. Image of submarine springs in Syria (Al-Charideh, 2004)

In general, the occurrences of drainage in the model (Fig. 40) have a good spatial matching with the estimation of surface water discharge by PCR-GLOBWB global model (Fig. 7) knowing that most of the surface water discharge in the Levant is fed by springs except Litani River (4) which is mostly formed in Bekaa Plain (outside the model boundary) (Abou Zakhem & Hafez, 2007). For, example, the most popular drainage occurrence in the borders between Syria and Lebanon which is corresponding to the location of Al-Kabir which is fed by 70 major springs (Abou Zakhem & Hafez, 2007). In the zone of rows 400 to 500 and columns 120 to 150 (Fig. 40), significant drainage occurrence is modelled which is assembled to the location of Timsah and Ras Al Ain springs.

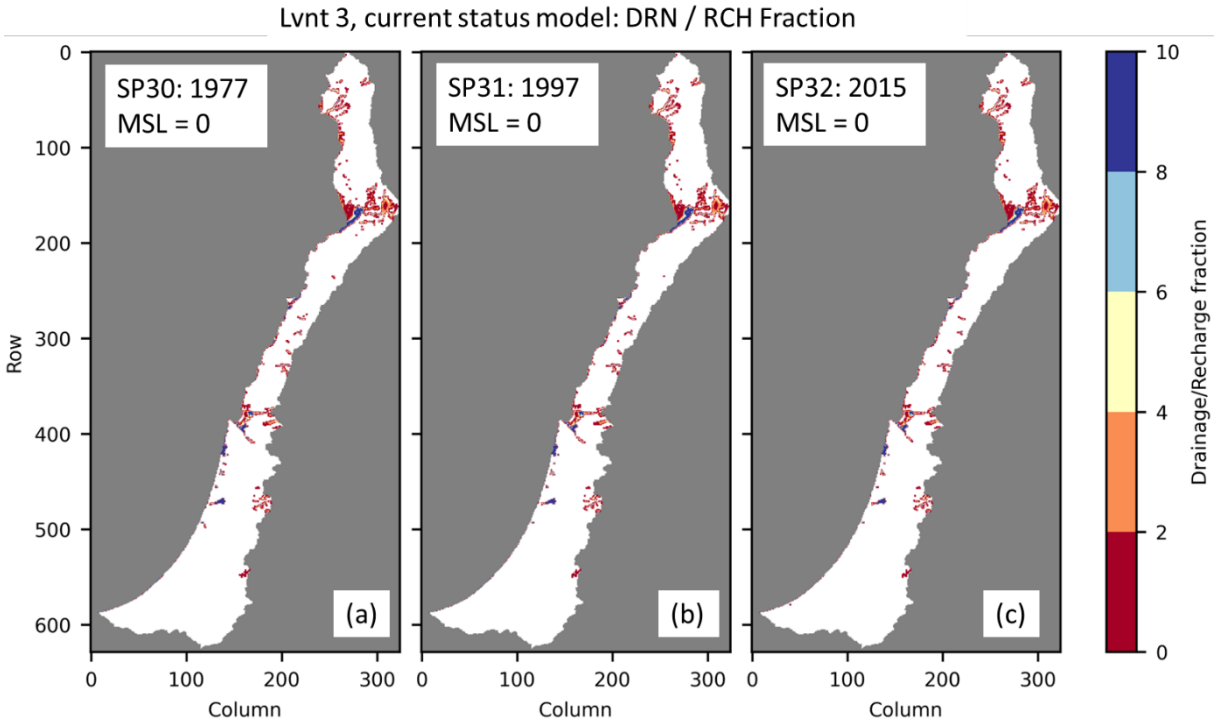

Fig. 40. Drainage / recharge (Fig. 19b) fraction for (a) SP30: 1977, (b) SP31: 1997, and (c) SP32: 2015

Subtracting the computed head of the current status stress periods (SP30, 31, and 32) from the reference model which is the final paleo reconstruction stress period (SP29), significant growing groundwater table depletion is observed in the elevated land of Lebanon reaching more than 180 meters. This is because of the high surface elevation which in the mountain reaches 3000 meters resulting in lower retention of groundwater especially with the incorporation of human activities, i.e., abstraction. Thus, the mountainous groundwater (situated in no flow boundary area) continuously substitutes the abstracted water from the coastal plain. That is why

approximately no depletion is noticed in the coastal plain in no significant change in the submarine groundwater discharge is observed along the coastline of Lebanon. On the other hand, flat land in the southern part of the Levant also experiences considerable depletion due to the relatively huge abstraction meeting low recharge in semi-arid to arid region. The growing groundwater table depletion in 115 years (Fig. 41) is an alert for decision-makers warning of more probable and severe depletion in the future under the pressing global change stresses.

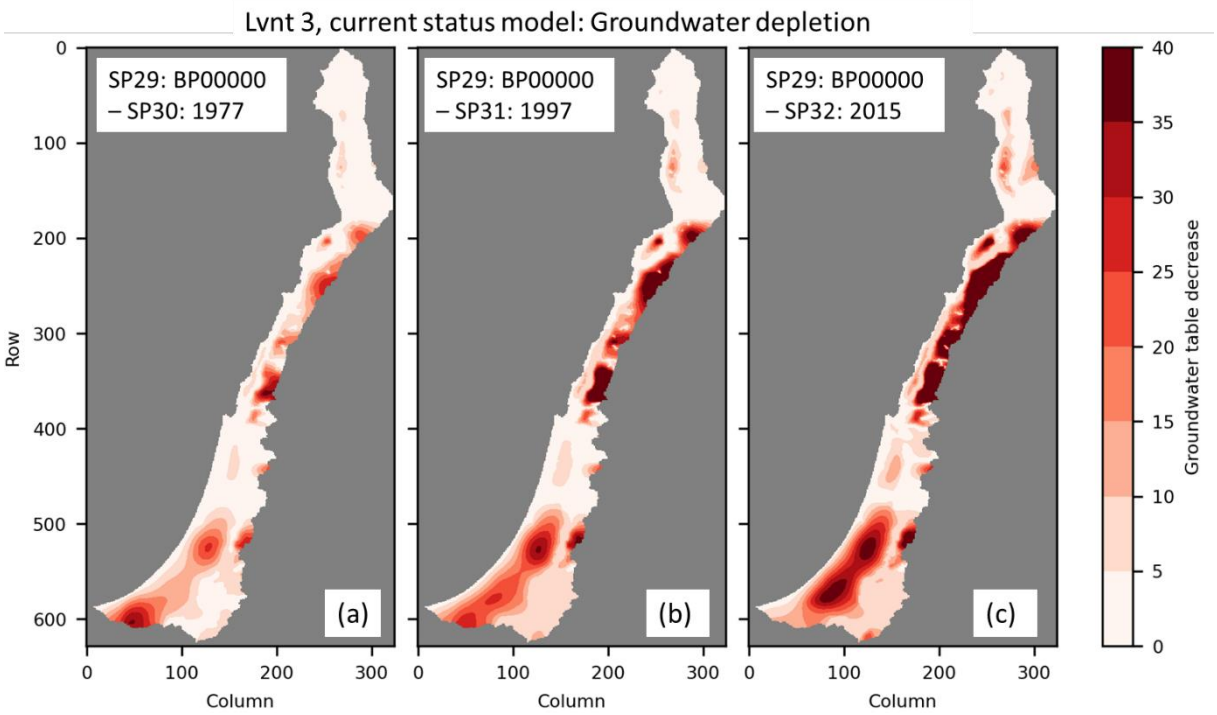

Fig. 41. Groundwater depletion represented in the groundwater table decrease for (a) SP29: BP 00000 – SP30: 1977, and (b) SP29: BP 00000 – SP31: 1997, and (c) SP29: BP 00000 - SP32: 2015

The same cross-sections that were presented for the paleo-hydrogeographical model are presented here for the current statues. Notable differences in concentration are not visually evident among the current status model's cross sections (Fig. 42a, b, and c). However, when the computed concentration of the current status stress periods (SP30, 31, and 32) is subtracted from the reference model (final paleo-reconstruction stress period - SP29), changes in TDS become apparent, particularly in cross section C. This section demonstrates an increasing freshening process of the previously saltwater introduced through Binyamina fault when the sea-level exceeded 0 msl. As anticipated, cross section C exhibits the most pronounced saltwater intrusion when compared to cross sections A and B.

A more detailed understanding of model salinity is obtained through 12 cross sections across the model domain (Fig. 43), showcasing concentration changes by subtracting the computed concentration of the current status (SP32: 2015) from the reference model (final paleo reconstruction stress period - SP29: BP00000). The southern part of the Levant (sections 9, 10, 11, and 12) exhibits active freshwater-seawater interaction, causing TDS changes of up to 5 g/l. This is attributed to the region's flatter terrain, thicker Quaternary deposit, higher abstraction, and lower recharge rates. Saltwater intrusion primarily occurs in the upper groundwater system (Quaternary), influenced by abstraction, particularly in the southern part (e.g., Gaza) corresponding to observed data (section 3.2.5). Intrusion mainly affects the upper aquifer due to simulated abstraction in the 5th layer of the Quaternary deposit, separate from the Regional Deep Cretaceous Aquifer. The deep aquifer typically experiences little intrusion, except in the

9th cross section where Binyamina fault contributes to severe intrusion which agrees with findings of Bar Yosef (1978), Mandell et al. (2003) and Mercado, (1980). Generally, little influence of abstraction on saltwater intrusion is observed which may be attributed to time-variant rates of abstraction (Seibert et al., 2023; van Engelen et al., 2021). The hydraulic conductivity highly affects saltwater intrusion but the longitudinal dispersivity has slight influence (Meyer et al., 2019; Van Pham et al., 2019).

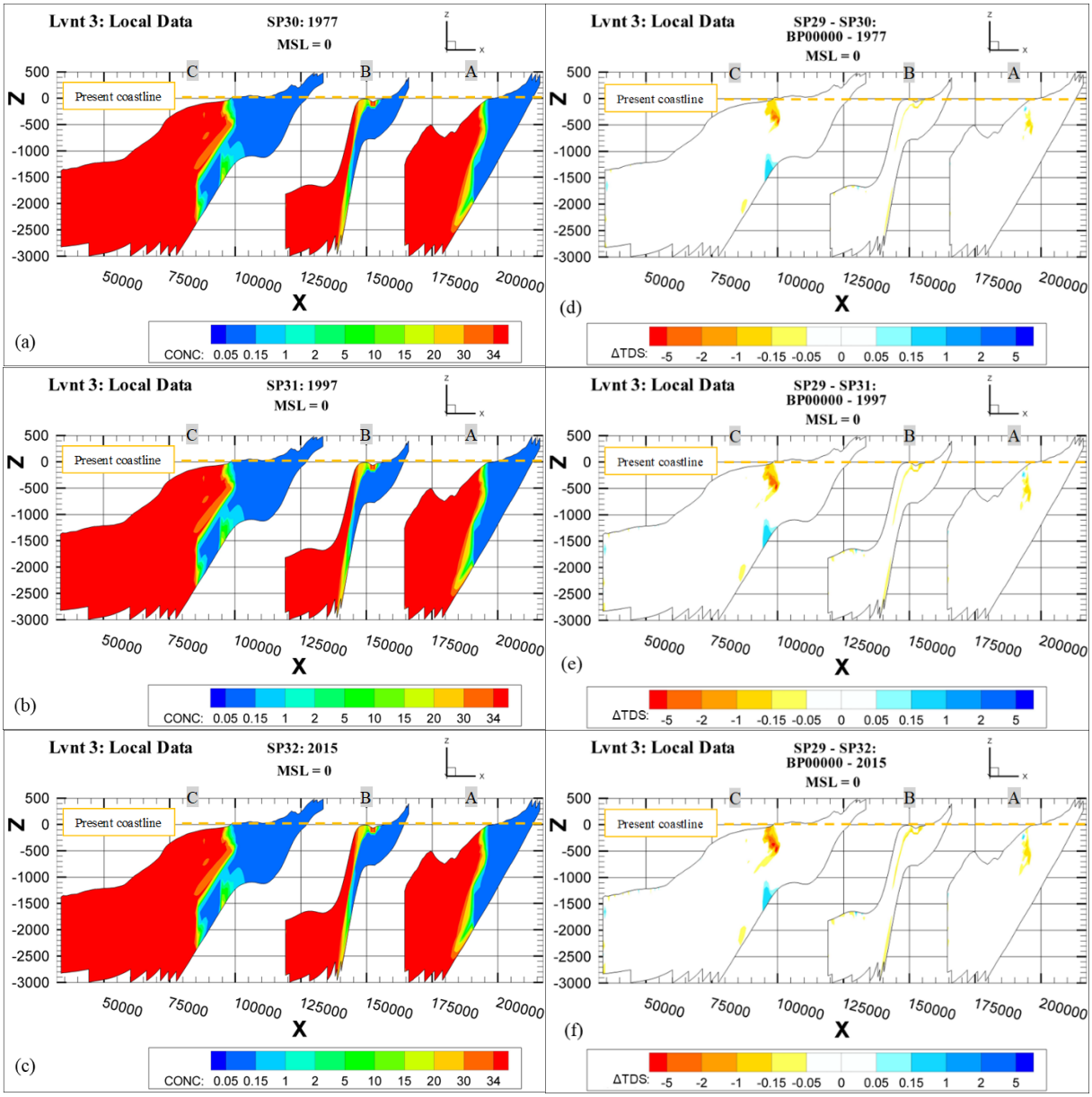

Fig. 42. Cross sections of the modelled concentrations (g TDS/l) for (a) SP30: 1977, (b) SP31: 1997, and (c) SP32: 2015 and change in TDS (g/l) for (d) SP29: BP 00000 – SP30: 1977, and (e) SP29: BP 00000 – SP31: 1997, and (f) SP29: BP 00000 - SP32: 2015

Some freshening is observed in cross section 4th, 8th, 9th, 11th, and 12th, the TDS of the SP32: 2015 is 2 g/l lower than how it is in the SP29: 00000. This may be attributed to the higher sea-level in the period between BP05000 to BP01000 reaching 7 msl. That intruded some salt to the transition zone so this salt is under diffusion process after the sea-level decreased to 0 msl. In Lebanon, regional saltwater intrusion is limited due to the elevated inland heights, high

hydraulic gradient, and thin coastal plain (5 m thickness), despite experiencing the highest groundwater table depletion (Fig. 41).

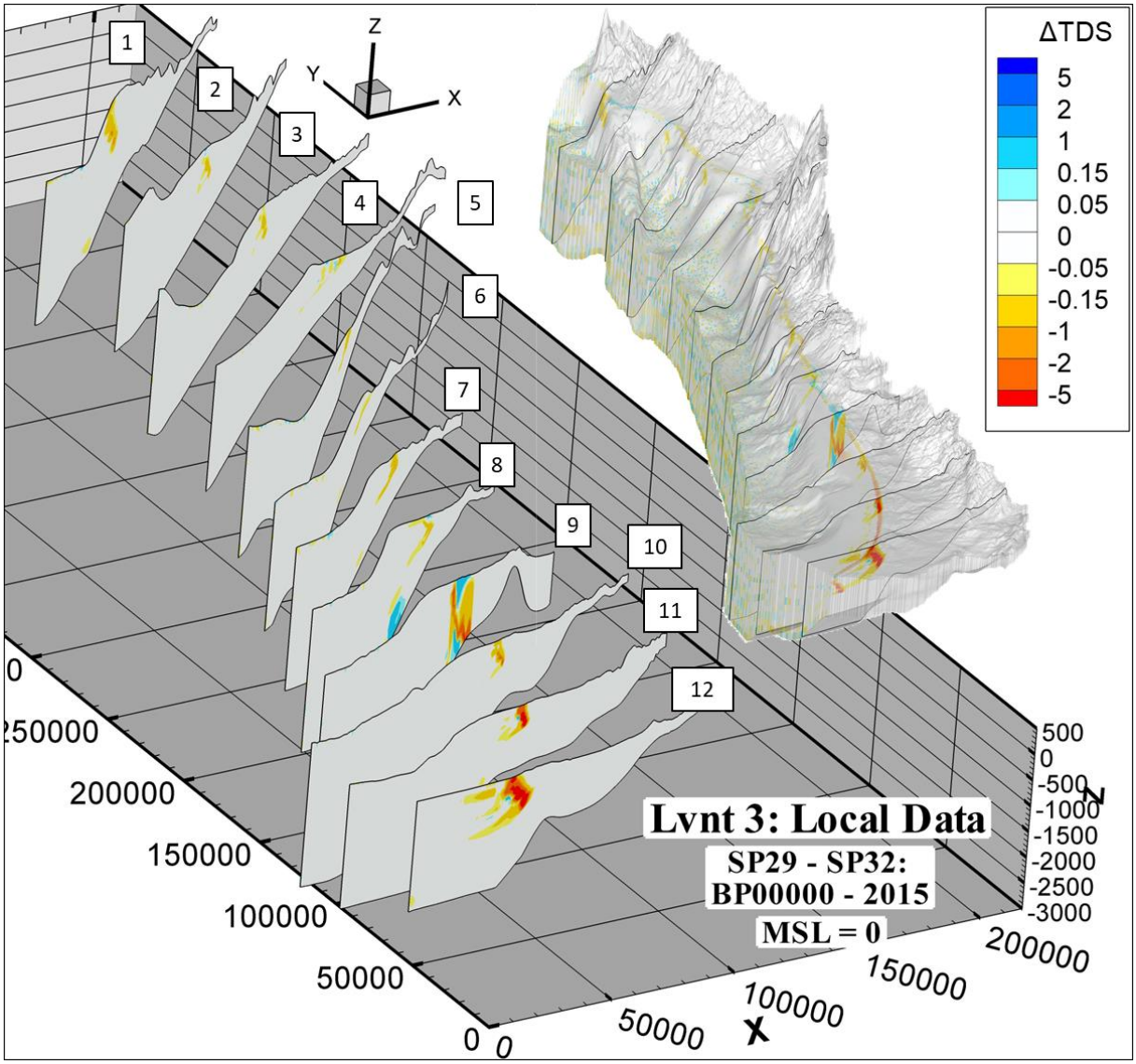

Fig. 43. Cross section of the change in TDS for Lvnt 3, the locations of the cross sections are shown in the upper-right of the figure

Despite the active abstraction and constant sea-level, the fresh groundwater volume between 1900 and 1977 is increasing (Fig. 44). This is related to the groundwater memory (lag) since the sea-level 3000 years ago was about 7 msl (Kooi et al., 2000; Post & Kooi, 2003). In contrast, a reduction in the fresh groundwater volume can be observed between 1978 and 2015 due to the growing groundwater abstraction. The solute mas has a typical opposite pattern of fresh groundwater volume.

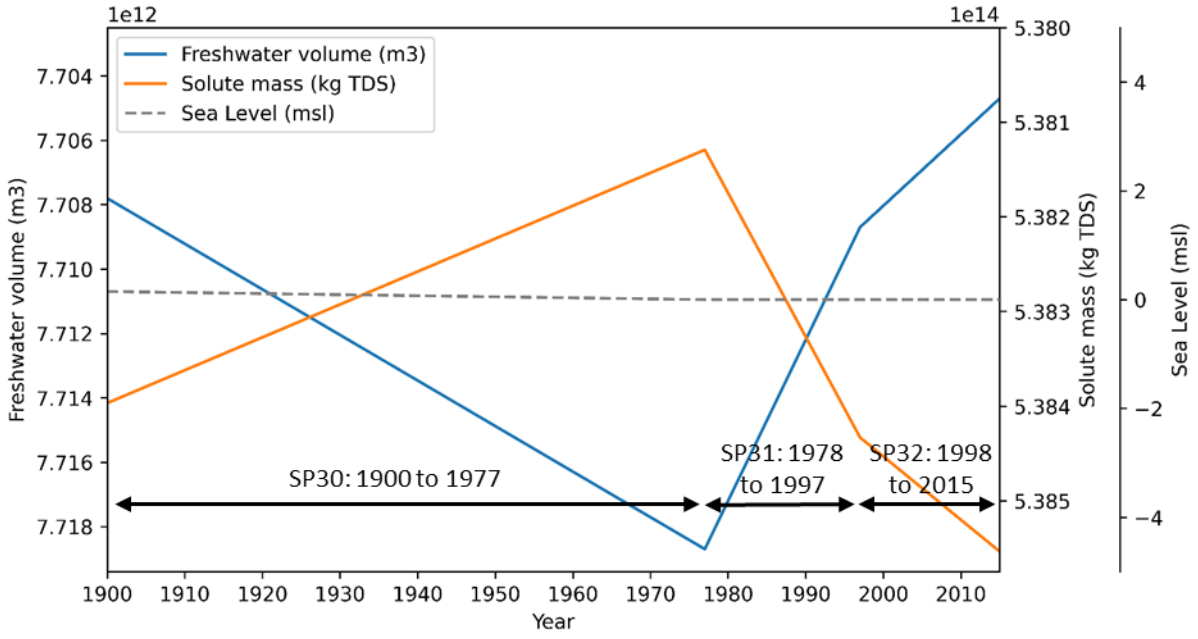

Fig. 44. Fresh groundwater volume ($m^3 \times 10^{12}$) and solute mass (kg TDS) of Lvnt 3 along the current status periods

4.3 Model Simplifications and Limitations

While the paleo-hydogeographical modelling approach presented here is complex, it remains considerably simplified due to two main reasons. First, limited data constrains boundary and initial conditions, a challenge more pronounced when considering past millennia. Second, numerical models simulation salt transport involves coarse grid discretization, and computational power constraints (Konikow, 2011). This simplification particularly impacts local-scale accuracy in paleo groundwater salinity reconstructions.

Salinity distribution is heavily influenced by hydraulic conductivities and effective porosities, key parameters shaped by geological models (Meyer et al., 2019; van Engelen et al., 2021). Consequently, inaccuracies in the simplified geological model, such as assuming uniform geology in the offshore part or spare input data in geological models, as well as ignoring fine-scale details, directly impact the accuracy of salinity distribution. For example, geological simplifications, including disregarding interactions among layers and geological faults (Beydoun, n.d.; Brew et al., 2001; Gardosh et al., 2008; Gomez et al., 2007; Hawie et al., 2013; Laskow et al., 2011; Nader et al., 2016; Petrolink et al., 2001; Shaban & Shaban, 2010), and the positioning of the western barrier of the Deep Cretaceous Aquifer and karstification modelling (Abusaada, 2011; Banusch et al., 2022; Bresinsky et al., 2023; Dafny et al., 2010; Dvory et al., 2016; Laskow et al., 2011; Weinberger et al., 1994; Yechieli et al., 2019; Zilberbrand et al., 2014), contribute to these uncertainties.

The numerical model's simplifications involve coarse cell size and time stepping (SP = 1000 years) due to computational demands of the supra-regional groundwater model. With a horizontal resolution of 765 × 940 m and vertical up to 400 m, it cannot precisely simulate local aspects like topography, abstraction, recharge, drainage, and upconing processes potentially impacting local salinization distribution (Pauw et al., 2016; Post & Kooi, 2003). The effective porosity was assumed 0.25 for the whole model domain but it will probably decrease in deep groundwater system (Verweij, 2003). During the calibration process, springs discharge and transient model calibration were not taken into account. The rivers were not modelled which

has a proven effect on the head modelling in Syria as well as constant recharge was considered for both paleo and current status models. Since the global data model for abstraction lacks layer specification, all groundwater demand was abstracted from the second Quaternary aquifer.

Therefore, the modelling methodology employed in this study should be regarded as a conceptual instrument for enhancing insights into coastal groundwater salinization attributes, instead of anticipating precise local representation (Delsman et al., 2014; Konikow, 2011; Seibert et al., 2023).

5. Conclusions and Recommendations

5.1 Conclusions

This research endeavours to understand the groundwater system of the Levant coastal region, aiming to construct a 3D model of variable-density groundwater flow coupled with salt transport. The study delves into both paleo and current groundwater conditions, exploring indicators like submarine groundwater discharge, water budget, paleo fresh groundwater, saltwater intrusion, groundwater depletion, and freshwater groundwater volume. The paleo-hydrogeographical model investigates the influence of sea-level changes 30 ka, while the current status model depicts the present groundwater state. Additionally, the research aims at analyzing the reliability of global datasets in building a supra-regional groundwater model, analyzing the effect of complex features, e.g. geology and recharge, on the model accuracy, developing fully scripted and reproducible modelling framework for the Levant improving the Global Coastal Groundwater Modelling toolbox (GCGM).

The analysis of complex features indicates that using global data (Lvnt 1) to create a supra-regional groundwater model focused solely on unconsolidated sediments provides a reasonable representation of coastal geology but falls short in mountainous areas (RMSE for head 90.93 msl). Constructing a supra-regional model with global and limited local data (Lvnt 2) yields poorer results (RMSE for head 133.19 msl). Conversely, employing spatially distributed local data to guide the utilization of global databases, incorporating both consolidated and unconsolidated sediments, results in a reliable groundwater model at RMSE for head 38.78 msl. Using constant recharge across the entire study area, characterized by high climatic variation, leads to head overestimation in certain regions like the Negev desert. While PCR-GLOBWB is a promising recharge tool, adjustments based on local data are crucial for accurate mountainous area head matching.

The use of GCGM with global datasets results in model bottom elevation with drops, limiting sea-groundwater interaction. All alternative models show unsatisfactory salinity modelling performance (RMSEs range from 9.28 to 9.40 g TDS/l), possibly due to oversimplified model discretization, scarce observational data, boundary conditions, a probable erroneous initial groundwater salinity discounting the ancient trapped salt results in not realistic current salinity distribution. The refined and fully scripted GCGM toolbox in this research yields a reproducible groundwater model with acceptable hours of runtime. Generally, global data based models (Lvnt 1) can offer realism in coastal zones where there is high similarity between cases around the world but not in the mountain areas where there is high complexity in the geology. However, to achieve this goal, some modelling features have to be solved such as boundary conditions.

In Lvnt 3, the most realistic model, the paleo-reconstruction period (30 ka ago) reveals that the lowest sea-level (-120 msl) at BP16000 exhibited the highest submarine groundwater discharge. As sea-level rises, drainage increases to 8 MCM/day due to elevated groundwater table levels. Generally, saltwater intrusion during the reconstruction period remains relatively low. Matching the real situation, the model captures the phenomenon of submarine springs along Syria and Lebanon's coastline.

Despite having the highest fresh groundwater volume, BP16000 (sea-level -120 msl) records the most significant groundwater table depletion (reaching 80 m below the current groundwater table). Conversely, the most recent stress period exhibits the lowest fresh groundwater volume

despite having the highest groundwater table. A distinct pattern emerges: higher sea-levels correspond to elevated groundwater tables and decreased fresh groundwater volume, and vice versa. Mountainous areas exhibit low groundwater table dynamicity, while coastal zones show significant fluctuations due to sea-level change. Evidence of paleo freshwater existence spans over 22,000 years, maintained in the model and offshore at depths exceeding 1000 m. Inland saltwater is trapped as seawater at 1000 m depths due to extensive saltwater intrusion via the Binyamina fault 3 ka ago during a sea-level increase to 7 msl. A robust linear correlation (R^2 of 0.99) is evident between fresh groundwater volume and sea-level rise during the transgression period (BP16000 to BP00000). The fresh groundwater volume's lagged response to sea-level changes, especially during the transgression period, is tied to low-permeable layers in the Levant's deepest regions, preserving groundwater memory for millennia.

In the current status model of sea-level at 0 msl, initiated with computed paleo salinity distribution, notable findings include drainage reaching up to 10 times recharge in Ibrahim River, Al-Kabir River, Timsah, and Ras Al Ain springs. The model indicates severe groundwater table depletion in Lebanon's mountains, with levels dropping up to 180 meters due to groundwater abstraction implemented in 2015. Similar severe depletion is observed in the southern coastal zone, where groundwater tables drop by over 40 meters. Over the past 3,000 years, a gradual freshening process for salt that was trapped within the system when the sea-level reached 7 msl. Conversely, the most severe saltwater intrusion is observed in the southern Levant coast, with an increase of groundwater salinity by more than 5 g TDS/l. Lebanon exhibits the lowest potential for saltwater intrusion. Despite active abstraction and a constant sea-level, the period between 1900 and 1977 sees a slight increase in fresh groundwater volume, supporting the groundwater memory hypothesis.

5.2 Recommendations

In order to enhance future modelling endeavours, several key considerations should be taken into account. Firstly, the incorporation of extra data concerning paleo-hydrogeology is crucial. This entails obtaining spatially distributed information about paleo-groundwater recharge rates, as well as integrating data on historical storm floods and rivers. Additionally, it is recommended to simulate sea-level changes during interglacial periods when sea-levels matched or exceeded the current levels which probably delivered salt onshore (Zamrsky et al., 2020). Thirdly, the collection of more comprehensive observational data is essential. This should encompass not only river, spring, and drainage properties, but also geological data, with a specific emphasis on regions like Syria. Refining the geological model is advised, necessitating the inclusion of complex geological features such as faults. The assessment of groundwater abstraction from a global model using local studies shows acceptable results in the water budget. However, a limitation lies in the global model's (PCR-GLOBWB) lack of detail regarding abstraction. Introducing a logical distribution of abstraction across aquifers within could potentially enhance the modelling performance.

To enhance the precision and reliability of the numerical modelling approach of salt transport, several recommendations are proposed. Firstly, it is advised to implement a higher degree of temporal and spatial discretization within the numerical models. This involves employing finer cell sizes, particularly along coastal areas, to provide a more accurate representation of transition zones as well as historical and present groundwater recharge patterns. Secondly, the calibration process may give a better representation of reality by the implementation of transient calibration and the inclusion of spring discharge. Thirdly, conducting sensitivity analyses might

offer insights into the significance of factors like recharge and hydraulic properties in the model and their effect on the computational demand, previous investigation was performed by van Engelen et al. (2021) as well as the effect of the stepsizes on groundwater salinity distribution. Additionally, enhancing the final salinity distribution of paleo reconstruction via incorporating ancient trapped onshore salt could improve the model's realism, e.g., including the current salinity distribution of the Senonian deposit ranged between 600 and 11,000 mgCl/l (Burg & Gersman, 2016; Livshitz, 1997; Rosenthal et al., 1999; Zilberbrand et al., 2014). A similar approach was conducted by van Engelen et al. (2021) by assigning a fixed concentration for Pleistocene deposit at 120 g TDS / l. Lastly, reducing uncertainties related to salt transport parameters, such as dispersivity parameters (e.g., higher longitudinal dispersivity) and molecular diffusion coefficients, could contribute to more accurate salt transport.

The Global Coastal Groundwater Modelling (GCGM) toolbox could also be improved. Firstly, for getting reasonable accuracy from a model built using only global datasets, excluding the mountainous areas is necessary because it has complex geology, and topography, unlike the coastal zones. Coastal zones are easier to simulate and generalize because of their high similarity around the world. This can be achieved by creating a function that defines the model boundary depending on a maximum surface elevation of inclusive (e.g. 400 m) during the process of extracting the boundary from HydroBASINS (Lehner & Grill, 2013). Secondly, develop the toolbox by including rivers using global databases such as PCR-GLOBWB (Sutanudjaja et al., 2018) and HydroRIVERS (Lehner & Grill, 2013). Thirdly, create a function to include global datasets providing estimation of the hydraulic conductivity (Gleeson et al., 2014; Hartmann & Moosdorf, 2012). Fourthly, automatically define the model discretization component (mud/sand ratio) (Zamrsky et al., 2020) by determining the ID of the COSCAT area using its location. Fifthly, build algorithm to calibrate the model using tools like PEST. Sixthly, use data mining to collect head, and groundwater salinity data for model calibration and for local input data such as recharge, abstraction, and geology. Lastly, develop a graphical user interface (GUI) to allow experts around the world to use the GCGM toolbox even if they do not know Python or provide extensive documentation.

6. References

Abd-Elaty, I., Abd-Elhamid, H. F., & Qahman, K. (2020). Coastal Aquifer Protection from Saltwater Intrusion Using Abstraction of Brackish Water and Recharge of Treated Wastewater: Case Study of the Gaza Aquifer. *Journal of Hydrologic Engineering*, *25*(7), 05020012. https://doi.org/10.1061/(ASCE)HE.1943-5584.0001927

Abou Zakhem, B., & Hafez, R. (2007). Environmental isotope study of seawater intrusion in the coastal aquifer (Syria). *Environmental Geology*, *51*(8), 1329–1339. https://doi.org/10.1007/S00254-006-0431-X/FIGURES/10

Abu Al Naeem, M. F., Yusoff, I., Ng, T. F., Maity, J. P., Alias, Y., May, R., & Alborsh, H. (2019). A study on the impact of anthropogenic and geogenic factors on groundwater salinization and seawater intrusion in Gaza coastal aquifer, Palestine: An integrated multi-techniques approach. *Journal of African Earth Sciences*, *156*, 75–93. https://doi.org/10.1016/j.jafrearsci.2019.05.006

Abu Ghazleh, S., Abed, A. M., & Kempe, S. (2011). The Dramatic Drop of the Dead Sea: Background, Rates, Impacts and Solutions. *Environmental Science and Engineering*, 77–105. https://doi.org/10.1007/978-3-642-14779-1_4/COVER

Abu-alnaeem, M. F., Yusoff, I., Ng, T. F., Alias, Y., & Raksmey, M. (2018). Assessment of groundwater salinity and quality in Gaza coastal aquifer, Gaza Strip, Palestine: An integrated statistical, geostatistical and hydrogeochemical approaches study. *Science of The Total Environment*, *615*, 972–989. https://doi.org/10.1016/j.scitotenv.2017.09.320

Abusaada, M. J. (2011). *Flow dynamics and management options in stressed carbonate aquifer system, the Western Aquifer Basin, Palestine*.

Aish, A. M. (2022). Estimation of Spatial Groundwater Recharge and Surface Runoff in the Gaza Coastal Aquifer Using GIS-Based WetSpass Model. *International Journal of Geoinformatics*, *18*(6), 25–32. https://doi.org/10.52939/ijg.v18i6.2457

Al-Charideh. (2004). *Coastal submarine springs in Lebanon and Syria: Geological, geochemical, and radio-isotopic study*. https://doi.org/https://doi.org/

Al-Charideh, A., & Kattaa, B. (2016). Isotope hydrology of deep groundwater in Syria: renewable and non-renewable groundwater and paleoclimate impact. *Hydrogeology Journal*, *24*(1), 79–98. https://doi.org/10.1007/S10040-015-1324-4/FIGURES/11

Allow, K. A. (2011). Seawater intrusion in Syrian coastal aquifers, past, present and future, case study. *Arabian Journal of Geosciences*, *4*(3–4), 645–653. https://doi.org/10.1007/S12517-010-0261-8/FIGURES/7

Asfahani, J. (2021). Classification of the transmissivity spatial variations of Quaternary aquifer in the semi-arid Region Khanasser Valley, Northern Syria. *Journal of African Earth Sciences*, *182*, 104269. https://doi.org/10.1016/J.JAFREARSCI.2021.104269

Baba, A., Karem, R. AL, & Yazdani, H. (2021). Groundwater resources and quality in Syria. *Groundwater for Sustainable Development*, *14*, 100617. https://doi.org/10.1016/J.GSD.2021.100617

Badon-Ghyben, W., & Drabbe, J. (1889). Nota in verband met de voogenomen put boring nabij Amsterdam (Notes on the probable results of the proposed well drilling near Amsterdam). *Tijdschr. Kon. Inst. Ing.*, 8–22.

Bakalowicz, M. (2009). Assessment and management of water resources with an emphasis on prospects of climate change. *GWP. MED/EUWI, 46p*.

Bakker, M., Post, V., Langevin, C. D., Hughes, J. D., White, J. T., Starn, J. J., & Fienen, M. N. (2016). Scripting MODFLOW Model Development Using Python and FloPy. *Groundwater*, *54*(5), 733–739. https://doi.org/https://doi.org/10.1111/gwat.12413

Banusch, S., Somogyvári, M., Sauter, M., Renard, P., & Engelhardt, I. (2022). Stochastic Modeling Approach to Identify Uncertainties of Karst Conduit Networks in Carbonate Aquifers. *Water Resources Research*, *58*(8), e2021WR031710. https://doi.org/https://doi.org/10.1029/2021WR031710

Bar, O., Gvirtzman, Z., Feinstein, S., & Zilberman, E. (2013). Accelerated subsidence and sedimentation in the Levant Basin during the Late Tertiary and concurrent uplift of the Arabian platform: Tectonic versus counteracting sedimentary loading effects. *Tectonics*, *32*(3), 334–350. https://doi.org/10.1002/TECT.20026

Bar Yosef, Y. (1978). *The Taninim Deep borehole: a further investigation of the salinization processes in the Yarkon Taninim aquifer. Tahal, Water Planning for Israel, Rep*.

Barlow, P. M., & Reichard, E. G. (2010). Saltwater intrusion in coastal regions of North America. *Hydrogeology Journal*, *18*(1), 247–260. https://doi.org/10.1007/S10040-009-0514-3/FIGURES/7

Beydoun, Z. R. (n.d.). *THE LEVANTINE COUNTRIES: THE GEOLOGY OF SYRIA AND LEBANON (MARITIME REGIONS)*.

Bresinsky, L., Kordilla, J., Engelhardt, I., Livshitz, Y., & Sauter, M. (2023). Variably saturated dual-permeability flow modeling to assess distributed infiltration and vadose storage dynamics of a karst aquifer – The Western Mountain Aquifer in Israel and the West Bank. *Journal of Hydrology X*, *18*, 100143. https://doi.org/https://doi.org/10.1016/j.hydroa.2022.100143

Brew, G., Lupa, J., Barazangi, M., Sawaf, T., Al-Imam, A., & Zaza, T. (2001). Structure and tectonic development of the Ghab basin and the Dead Sea fault system, Syria The Dead Sea fault system. In *Journal of the Geological Society* (Vol. 158).

Bruce, D. L., Yechieli, Y., Zilberbrand, M., Kaufman, A., & Friedman, G. M. (2007). Delineation of the coastal aquifer of Israel based on repetitive analysis of 14C and tritium. *Journal of Hydrology*, *343*(1), 56–70. https://doi.org/https://doi.org/10.1016/j.jhydrol.2007.05.031

Burg, A., & Gersman, R. (2016). Hydrogeology and geochemistry of low-permeability oil-shales – Case study from HaShfela sub-basin, Israel. *Journal of Hydrology*, *540*, 1105–1121. https://doi.org/10.1016/J.JHYDROL.2016.07.026

Custodio, E. (2002). Aquifer overexploitation: What does it mean? *Hydrogeology Journal*, *10*(2), 254–277. https://doi.org/10.1007/S10040-002-0188-6/METRICS

Custodio Gimena, E., & Bruggeman, G. A. (1987). *Groundwater problems in coastal areas*. https://unesdoc.unesco.org/notice?id=p::usmarcdef_0000074510

Dafny, E., Burg, A., & Gvirtzman, H. (2010). Effects of Karst and geological structure on groundwater flow: The case of Yarqon-Taninim Aquifer, Israel. *Journal of Hydrology*, *389*(3), 260–275. https://doi.org/https://doi.org/10.1016/j.jhydrol.2010.05.038

De Louw, P. G. B., Eeman, S., Siemon, B., Voortman, B. R., Gunnink, J., Van Baaren, E. S., & Oude Essink, G. H. P. (2011). Shallow rainwater lenses in deltaic areas with saline seepage. *Hydrology and Earth System Sciences*, *15*(12), 3659–3678. https://doi.org/10.5194/HESS-15-3659-2011

de Louw, P. G. B., Oude Essink, G. H. P., Stuyfzand, P. J., & van der Zee, S. E. A. T. M. (2010). Upward groundwater flow in boils as the dominant mechanism of salinization in deep polders, The Netherlands. *Journal of Hydrology*, *394*(3–4), 494–506. https://doi.org/10.1016/J.JHYDROL.2010.10.009

DeConto, R. M., & Pollard, D. (2016). Contribution of Antarctica to past and future sea-level rise. *Nature 2016 531:7596*, *531*(7596), 591–597. https://doi.org/10.1038/nature17145

Delsman, J. R., Hu-A-Ng, K. R. M., Vos, P. C., De Louw, P. G. B., Oude Essink, G. H. P., Stuyfzand, P. J., & Bierkens, M. F. P. (2014). Paleo-modeling of coastal saltwater intrusion during the Holocene: An application to the Netherlands. *Hydrology and Earth System Sciences*, *18*(10), 3891–3905. https://doi.org/10.5194/HESS-18-3891-2014

Delsman, J. R., Mulder, T., Verastegui, B. R., Bootsma, H., Huizer, S., Essink, G. H. P. O., Zitman, P., Huizer, S., & Oude Essink, G. H. P. (2023). Reproducible construction of a high-resolution national variable-density groundwater salinity model for the Netherlands. *Environmental Modelling & Software*, *164*, 105683. https://doi.org/10.1016/J.ENVSOFT.2023.105683

Dvory, N. Z., Livshitz, Y., Kuznetsov, M., Adar, E., & Yakirevich, A. (2016). The effect of hydrogeological conditions on variability and dynamic of groundwater recharge in a carbonate aquifer at local scale. *Journal of Hydrology*, *535*, 480–494. https://doi.org/https://doi.org/10.1016/j.jhydrol.2016.02.011

Edmunds, W. M., & Milne, C. J. (2001). Palaeowaters in Coastal Europe: Evolution of Groundwater since the Late Pleistocene. *Geological Society, London, Special Publications*, *189*(1). https://doi.org/10.1144/GSL.SP.2001.189

Falkenmark, M. (1989). Middle East Hydropolitics: Water Scarcity and Conflicts in the Middle East. *Ambio*, *18*(6), 350–352. http://www.jstor.org/stable/4313608

FAO. (2014). *AQUASTAT*.

Ferguson, G., & Gleeson, T. (2012). Vulnerability of coastal aquifers to groundwater use and climate change. *Nature Climate Change 2012 2:5*, *2*(5), 342–345. https://doi.org/10.1038/nclimate1413

Frem, M., & Saad, S. (2021). *Spatially Distributed Groundwater Recharge Estimation through the Application of a Long Term Regional Water Balance using Geographic Information Systems: A Case Study for Lebanon*.

Gardosh, M., Druckman, Y., Buchbinder, B., & Rybakov, M. (2008). *The Levant Basin offshore Israel: stratigraphy, structure, tectonic evolution and implications for hydrocarbon exploration*. Geophysical Institute of Israel Lod, Israel.

Ghannam, J., Ayoub, G. M., & Acra, A. (2009). A Profile of the Submarine Springs in Lebanon as a Potential Water Resource. *Http://Dx.Doi.Org/10.1080/02508069808686783*, *23*(4), 278–286. https://doi.org/10.1080/02508069808686783

Gleeson, T., Moosdorf, N., Hartmann, J., & Van Beek, L. P. H. (2014). A glimpse beneath earth's surface: GLobal HYdrogeology MaPS (GLHYMPS) of permeability and porosity. *Geophysical Research Letters*, *41*(11), 3891–3898. https://doi.org/10.1002/2014GL059856

Gomez, F., Nemer, T., Tabet, C., Khawlie, M., Meghraoui, M., & Barazangi, M. (2007). Strain partitioning of active transpression within the Lebanese restraining bend of the Dead Sea Fault (Lebanon and SW Syria). *Geological Society Special Publication*, *290*, 285–303. https://doi.org/10.1144/290.10/ASSET/EBFCF3DC-2568-4DC5-95A7-AA796CCA8255/ASSETS/IMAGES/LARGE/1322CH10F10.JPG

Goofers, W. S. (2020). *Paleo-hydrogeographic reconstruction of the groundwater salinity in the Ayeyarwady Delta, Myanmar, using a 3D variable-density groundwater model*. Utrecht University.

Grant, K. M., Rohling, E. J., Bar-Matthews, M., Ayalon, A., Medina-Elizalde, M., Ramsey, C. B., Satow, C., & Roberts, A. P. (2012). Rapid coupling between ice volume and polar temperature over the past 150,000 years. *Nature 2012 491:7426*, *491*(7426), 744–747. https://doi.org/10.1038/nature11593

Gvirtzman, Z., Csato, I., & Granjeon, D. (2014). Constraining sediment transport to deep marine basins through submarine channels: The Levant margin in the Late Cenozoic. *Marine Geology*, *347*, 12–26. https://doi.org/10.1016/J.MARGEO.2013.10.010

Haasnoot, M., Kwadijk, J., Van Alphen, J., Le Bars, D., Van Den Hurk, B., Diermanse, F., Van Der Spek, A., Oude Essink, G., Delsman, J., & Mens, M. (2020). Adaptation to uncertain sea-level rise; how uncertainty in Antarctic mass-loss impacts the coastal adaptation strategy of the Netherlands. *Environmental Research Letters*, *15*(3), 034007. https://doi.org/10.1088/1748-9326/AB666C

Halwani, J., El-Hajj, A., & Halwani, B. (2022). Hydro-geochemical Study of the Coastal Aquifer in Tripoli (Lebanon). *Research Journal of Ecology and Environmental Sciences*, *2*(4), 103–117. https://doi.org/10.31586/RJEES.2022.212

Hanor, J. S. (1994a). Origin of saline fluids in sedimentary basins. *Geolo~zicalSociety Special Publication*, *78*, 151–174. http://sp.lyellcollection.org/

Hanor, J. S. (1994b). Physical and chemical controls on the composition of waters in sedimentary basins. *Marine and Petroleum Geology*, *11*(1), 31–45. https://doi.org/10.1016/0264-8172(94)90007-8

Harbaugh, A. W. (2005). MODFLOW-2005 : the U.S. Geological Survey modular ground-water model--the ground-water flow process. *Techniques and Methods*. https://doi.org/10.3133/TM6A16

Hartmann, J., & Moosdorf, N. (2012). The new global lithological map database GLiM: A representation of rock properties at the Earth surface. *Geochemistry, Geophysics, Geosystems*, *13*(12). https://doi.org/https://doi.org/10.1029/2012GC004370

Hawie, N., Gorini, C., Deschamps, R., Nader, F. H., Montadert, L., Granjeon, D., & Baudin, F. (2013). Tectono-stratigraphic evolution of the northern Levant Basin (offshore Lebanon).

Marine and Petroleum Geology, *48*, 392–410. https://doi.org/10.1016/j.marpetgeo.2013.08.004

Herzberg, A. (1901). *Die Wasserversorgung einiger Nordseebäder: Journal für Gasbeleuchtung und Wasserversorgung*, *v. 44*. and.

IPCC. (2022). Sea Level Rise and Implications for Low-Lying Islands, Coasts and Communities. In C. Intergovernmental Panel on Climate (Ed.), *The Ocean and Cryosphere in a Changing Climate: Special Report of the Intergovernmental Panel on Climate Change* (pp. 321–446). Cambridge University Press. https://doi.org/DOI: 10.1017/9781009157964.006

Issar, A. (1968). Geology of the central coastal plain of Israel. *Israel Journal of Earth Sciences*, *17*, 16–29.

Jasechko, S., Perrone, D., Befus, K. M., Bayani Cardenas, M., Ferguson, G., Gleeson, T., Luijendijk, E., McDonnell, J. J., Taylor, R. G., Wada, Y., & Kirchner, J. W. (2017). Global aquifers dominated by fossil groundwaters but wells vulnerable to modern contamination. *Nature Geoscience 2017 10:6*, *10*(6), 425–429. https://doi.org/10.1038/ngeo2943

Jebreen, H., Wohnlich, S., Banning, A., Wisotzky, F., Niedermayr, A., & Ghanem, M. (2018). Recharge, geochemical processes and water quality in karst aquifers: Central West Bank, Palestine. *Environmental Earth Sciences*, *77*(6), 1–16. https://doi.org/10.1007/S12665-018-7440-4/TABLES/3

Kalaoun, O., Al Bitar, A., Gastellu-Etchegorry, J. P., & Jazar, M. (2016). Impact of Demographic Growth on Seawater Intrusion: Case of the Tripoli Aquifer, Lebanon. *Water 2016, Vol. 8, Page 104*, *8*(3), 104. https://doi.org/10.3390/W8030104

Khadra, W. M., & Stuyfzand, P. J. (2014). Separating baseline conditions from anthropogenic impacts: example of the Damour coastal aquifer (Lebanon). *Https://Doi.Org/10.1080/02626667.2013.841912*, *59*(10), 1872–1893. https://doi.org/10.1080/02626667.2013.841912

Khadra, W. M., & Stuyfzand, P. J. (2018). Simulation of saltwater intrusion in a poorly karstified coastal aquifer in Lebanon (Eastern Mediterranean). *Hydrogeology Journal*, *26*(6), 1839–1856. https://doi.org/10.1007/S10040-018-1752-Z/TABLES/5

Khair, K., Aker, N., Haddad, F., Jurdi, M., & Hachach, A. (1994). The environmental impacts of humans on groundwater in Lebanon. *Water, Air, & Soil Pollution*, *78*(1–2), 37–49. https://doi.org/10.1007/BF00475666/METRICS

Khair, K., Aker, N., & Zahruddine, K. (1992). Hydrogeologic Units Of Lebanon. *Applied Hydrogeology*, *1*(2), 34–49. https://doi.org/10.1007/S100400050024/METRICS

Khouri, J., & Droubi, A. (1981). Groundwater movement in the fissured karstic rocks (Eastern of Mediterranean Sea). *ACSAD/Dm*, *10*, 58.

Kinan, G. (2015). Mathematical model to simulate the hydrogeological conditions for aquifers in the area that is located between ALKABIR ALSHIMALI and ALSNOBAR rivers and evaluating their available resources. *Syria, Tishreen University*.

Konikow, L. F. (2011). The Secret to Successful Solute-Transport Modeling. *Groundwater*, *49*(2), 144–159. https://doi.org/10.1111/J.1745-6584.2010.00764.X

Kooi, H., & Groen, J. (2003). Geological processes and the management of groundwater resources in coastal areas. *Netherlands Journal of Geosciences*, *82*(1), 31–40. https://doi.org/10.1017/S0016774600022770

Kooi, H., Groen, J., & Leijnse, A. (2000). Modes of seawater intrusion during transgressions. *Water Resources Research*, *36*(12), 3581–3589. https://doi.org/10.1029/2000WR900243

Kundzewicz, Z. W., Mata, L. J., Arnell, N. W., DÖLL, P., Jimenez, B., Miller, K., Oki, T., ŞEN, Z., & Shiklomanov, I. (2009). The implications of projected climate change for freshwater resources and their management. *Https://Doi.Org/10.1623/Hysj.53.1.3*, *53*(1), 3–10. https://doi.org/10.1623/HYSJ.53.1.3

Lababidi, H., Shatila, A., & Acra, A. (1987). The progressive salination of groundwater in Beirut, Lebanon. *International Journal of Environmental Studies*, *30*(2–3), 203–208.

Larsen, F., Tran, L. V., Van Hoang, H., Tran, L. T., Christiansen, A. V., & Pham, N. Q. (2017). Groundwater salinity influenced by Holocene seawater trapped in incised valleys in the Red River delta plain. *Nature Geoscience 2017 10:5*, *10*(5), 376–381. https://doi.org/10.1038/ngeo2938

Laskow, M., Gendler, M., Goldberg, I., Gvirtzman, H., & Frumkin, A. (2011). Deep confined karst detection, analysis and paleo-hydrology reconstruction at a basin-wide scale using new geophysical interpretation of borehole logs. *Journal of Hydrology*, *406*(3), 158–169. https://doi.org/https://doi.org/10.1016/j.jhydrol.2011.06.011

Lehner, B., & Grill, G. (2013). Global river hydrography and network routing: baseline data and new approaches to study the world's large river systems. *Hydrological Processes*, *27*(15), 2171–2186. https://doi.org/https://doi.org/10.1002/hyp.9740

Livshitz, Y. (1997). Chemistry of interstitial water from the Eocene chalk of Avedat aquifer, northwestern Negev, Israel. *Proceedings of the 18th International Geochemical Exploration Symposium*, *24*, 25.

Livshitz, Y., Issar, A. S., Livshitz, Y., & Issar, A. S. (2010). Applying the Conceptual-Model of Progressive Development to the Contaminated Aquifer Underlying Israel's Coastal Plain. *Journal of Water Resource and Protection*, *2*(5), 396–402. https://doi.org/10.4236/JWARP.2010.25046

Loáiciga, H. A., Pingel, T. J., & Garcia, E. S. (2012). Sea Water Intrusion by Sea-Level Rise: Scenarios for the 21st Century. *Groundwater*, *50*(1), 37–47. https://doi.org/10.1111/J.1745-6584.2011.00800.X

M. Mushtaha, A., Van Camp, M., & Walraevens, K. (2019). Evolution of runoff and groundwater recharge in the Gaza Strip over the last four decades. *Environmental Earth Sciences*, *78*(1), 1–18. https://doi.org/10.1007/S12665-018-7999-9/FIGURES/11

M. Visser, & H. Bootsma. (2021). *iMOD Python: make massive MODFLOW models - imod-python documentation.* https://deltares.gitlab.io/imod/imod-python/

Mandell, A. H., Zeitoun, D. G., & Dagan, G. (2003). Salinity sources of Kefar Uria wells in the Judea group aquifer of Israel. Part 2—quantitative identification model. *Journal of Hydrology*, *270*(1), 39–48. https://doi.org/https://doi.org/10.1016/S0022-1694(02)00217-2

Meisler, H., Leahy, P. P., & Knobel, L. L. (1984). The effect of eustatic sea-level changes on saltwater-freshwater relations in the northern Atlantic Coastal Plain. *Water Supply Paper*. https://doi.org/10.3133/WSP2255

Mercado, A. (1980). Groundwater salinity in the Yarkon Taninim Beer Sheva basin: a conceptual model of the salinity regime and its source. *TAHAL, Water Planning for Israel, Tel Aviv, Rep, 1*(80), 60.

Meyer, R., Engesgaard, P., & Sonnenborg, T. O. (2019). Origin and Dynamics of Saltwater Intrusion in a Regional Aquifer: Combining 3-D Saltwater Modeling With Geophysical and Geochemical Data. *Water Resources Research*, *55*(3), 1792–1813. https://doi.org/10.1029/2018WR023624

Michael, H. A., Russoniello, C. J., & Byron, L. A. (2013). Global assessment of vulnerability to sea-level rise in topography-limited and recharge-limited coastal groundwater systems. *Water Resources Research*, *49*(4), 2228–2240. https://doi.org/10.1002/WRCR.20213

MoEW, & UNDP. (2014). Assessment of groundwater resources of Lebanon. *Ministry of Energy and Water, Lebanon, Beirut*.

Mulder, T. (2018). *Constructing 3D variable-density groundwater flow models for six deltas using global data sets*. Utrecht University.

Musallam, I. F. A. (2021). *Simulation of groundwater system and seawater intrusion response to climate change and human activities on the coastal aquifer of Gaza Strip, Palestine*.

Nader, F. H., Browning-Stamp, P., & Lecomte, J. C. (2016). GEOLOGICAL INTERPRETATION OF 2D SEISMIC REFLECTION PROFILES ONSHORE LEBANON: IMPLICATIONS FOR PETROLEUM EXPLORATION. *Journal of Petroleum Geology*, *39*(4), 333–356. https://doi.org/10.1111/JPG.12656

Nader, F. H., Inati, L., Ghalayini, R., Hawie, N., & Daher, S. B. (2018). Key geological characteristics of the Saida-Tyr Platform along the eastern margin of the Levant Basin, offshore Lebanon: implications for hydrocarbon exploration. *Oil & Gas Science and Technology – Revue d'IFP Energies Nouvelles*, *73*, 50. https://doi.org/10.2516/OGST/2018045

Nativ, R., & Weisbrod, N. (1994). Hydraulic connections among subaquifers of the Coastal Plain aquifer, Israel. *Ground Water; (United States)*, *32:6*(6), 997–1007. https://doi.org/10.1111/J.1745-6584.1994.TB00939.X

Oude Essink, G. (2003). *Mathematical models and their application to salt water intrusion problems*. https://doi.org/10.13140/2.1.1637.4727

Oude Essink, G. H. P., Van Baaren, E. S., & De Louw, P. G. B. (2010). Effects of climate change on coastal groundwater systems: A modeling study in the Netherlands. *Water Resources Research*, *46*(10). https://doi.org/10.1029/2009WR008719

Paldor, A., Shalev, E., Katz, O., & Aharonov, E. (2019). Dynamics of saltwater intrusion and submarine groundwater discharge in confined coastal aquifers: a case study in northern Israel. *Hydrogeology Journal*, *27*(5), 1611–1625. https://doi.org/10.1007/S10040-019-01958-5/FIGURES/9

Paster, A., Dagan, G., & Guttman, J. (2006). The salt-water body in the Northern part of Yarkon-Taninim aquifer: Field data analysis, conceptual model and prediction. *Journal of Hydrology*, *323*(1), 154–167. https://doi.org/https://doi.org/10.1016/j.jhydrol.2005.08.018

Pauw, P. S., van der Zee, S. E. A. T. M., Leijnse, A., & Oude Essink, G. H. P. (2016). Saltwater Upconing Due to Cyclic Pumping by Horizontal Wells in Freshwater Lenses. *Groundwater*, *54*(4), 521–531. https://doi.org/10.1111/GWAT.12382

Pelletier, J. D., Broxton, P. D., Hazenberg, P., Zeng, X., Troch, P. A., Niu, G.-Y., Williams, Z., Brunke, M. A., & Gochis, D. (2016). A gridded global data set of soil, intact regolith, and sedimentary deposit thicknesses for regional and global land surface modeling. *Journal of Advances in Modeling Earth Systems*, *8*(1), 41–65. https://doi.org/https://doi.org/10.1002/2015MS000526

Petrolink, G., Brew, G., Barazangi, M., Al-Maleh, A. K., & Sawaf, T. (2001). *Tectonic and Geologic Evolution of Syria* (Vol. 6, Issue 4). http://pubs.geoscienceworld.org/geoarabia/article-pdf/6/4/573/5440470/brew.pdf

Ponikarov, V. P. (1966). The geological map of Syria, 1: 200.000 and explanatory notes. *Syrian Arab Republic, Ministry of Industry, Department of Geological and Mineral Research, Damascus, Syria*.

Post, & Kooi, H. (2003). Rates of salinization by free convection in high-permeability sediments: Insights from numerical modeling and application to the Dutch coastal area. *Hydrogeology Journal*, *11*(5), 549–559. https://doi.org/10.1007/S10040-003-0271-7/FIGURES/7

Post, V. (2004). *Groundwater salinization processes in the coastal area of the Netherlands due to transgressions during the Holocene* [VU University Amsterdam]. https://library.wur.nl/WebQuery/hydrotheek/1700758

Post, V., & Abarca, E. (2010). Preface: Saltwater and freshwater interactions in coastal aquifers. *Hydrogeology Journal*, *18*(1), 1–4. https://doi.org/10.1007/S10040-009-0561-9/METRICS

Post, V. E. A., Groen, J., Kooi, H., Person, M., Ge, S., & Edmunds, W. M. (2013). Offshore fresh groundwater reserves as a global phenomenon. *Nature*, *504*(7478), 71–78. https://doi.org/10.1038/nature12858

Qahman, K., & Larabi, A. (2006). Evaluation and numerical modeling of seawater intrusion in the Gaza aquifer (Palestine). *Hydrogeology Journal*, *14*(5), 713–728. https://doi.org/10.1007/S10040-005-003-2/FIGURES/14

Quba'a, R., Alameddine, I., Abou Najm, M., & El-Fadel, M. (2018). Modeling the depletion of groundwater storage over time in the Levant: lessons learned from a water-stressed region. *Environmental Earth Sciences*, *77*(13), 505. https://doi.org/10.1007/s12665-018-7677-y

Ranganathan, V., & Hanor, J. S. (1988). Density-driven groundwater flow near salt domes. *Chemical Geology*, *74*(1–2), 173–188. https://doi.org/10.1016/0009-2541(88)90152-0

Ranjan, P., Kazama, S., & Sawamoto, M. (2006). Effects of climate change on coastal fresh groundwater resources. *Global Environmental Change*, *16*(4), 388–399. https://doi.org/10.1016/J.GLOENVCHA.2006.03.006

Reeder, M. S., Stow A.V., D. A. V., & Rothwell, R. G. (2002). Late Quaternary turbidite input into the east Mediterranean basin: new radiocarbon constraints on climate and sea-level

control. *Geological Society Special Publications*, *191*, 267–278. https://doi.org/10.1144/GSL.SP.2002.191.01.18

Riccardo Biancalani, Freddy Nachtergaele, Monica Petri, & Sally Bunning. (2013). *Land degradation assessment in drylands (LADA)*.

Rodell, M., Velicogna, I., & Famiglietti, J. S. (2009). Satellite-based estimates of groundwater depletion in India. *Nature 2009 460:7258*, *460*(7258), 999–1002. https://doi.org/10.1038/nature08238

Rosenthal, E., Weinberger, G., & Kronfeld, J. (1999). Ground Water Salinization Caused by Residual Neogene and Pliocene Sea Water-An Example from the Judea Group Aquifer, Southern Israel. *Groundwater*, *37*(2), 261–270. https://doi.org/10.1111/J.1745-6584.1999.TB00982.X

Saadeh, M. (2008). Seawater Intrusion in Greater Beirut, Lebanon. *Environmental Science and Engineering*, 362–371. https://doi.org/10.1007/978-3-540-85047-2_23/COVER

Saadeh, M., Wakim, E., Saadeh, M., & Wakim, E. (2017). Deterioration of Groundwater in Beirut Due to Seawater Intrusion. *Journal of Geoscience and Environment Protection*, *5*(11), 149–159. https://doi.org/10.4236/GEP.2017.511011

Salman, M., & Mualla, W. (2004). THE UTILIZATION OF WATER RESOURCES FOR AGRICULTURE IN SYRIA: ANALYSIS OF THE CURRENT SITUATION AND FUTURE CHALLENGES. In *International Seminar on Nuclear War and Planetary Emergencies ? 30th Session* (pp. 263–274). WORLD SCIENTIFIC. https://doi.org/doi:10.1142/9789812702753_0031

Sarkar, A., Nunn, J. A., & Hanor, J. S. (1995). Free thermohaline convection beneath allochthonous salt sheets: An agent for salt dissolution and fluid flow in Gulf Coast sediments. *Journal of Geophysical Research: Solid Earth*, *100*(B9), 18085–18092. https://doi.org/10.1029/95JB01857

Schewe, J., Heinke, J., Gerten, D., Haddeland, I., Arnell, N. W., Clark, D. B., Dankers, R., Eisner, S., Fekete, B. M., Colón-González, F. J., Gosling, S. N., Kim, H., Liu, X., Masaki, Y., Portmann, F. T., Satoh, Y., Stacke, T., Tang, Q., Wada, Y., … Kabat, P. (2014). Multimodel assessment of water scarcity under climate change. *Proceedings of the National Academy of Sciences of the United States of America*, *111*(9), 3245–3250. https://doi.org/10.1073/PNAS.1222460110/-/DCSUPPLEMENTAL/SAPP.PDF

Seibert, S. L., Greskowiak, J., Bungenstock, F., Freund, H., Karle, M., Meyer, R., Essink, G. H. P. O., Engelen, J. van, & Massmann, G. (2023). Paleo-Hydrogeological Modeling to Understand Present-Day Groundwater Salinities in a Low-Lying Coastal Groundwater System (Northwestern Germany). *Water Resources Research*, *59*(4), e2022WR033151. https://doi.org/10.1029/2022WR033151

Shaban, A. (2020). *Water Resources of Lebanon*. *7*. https://doi.org/10.1007/978-3-030-48717-1

Shaban, A., & Shaban, A. (2010). Support of Space Techniques for Groundwater Exploration in Lebanon. *Journal of Water Resource and Protection*, *2*(5), 469–477. https://doi.org/10.4236/JWARP.2010.25054

Spratt, R. M., & Lisiecki, L. E. (2016). A Late Pleistocene sea level stack. *Climate of the Past*, *12*(4), 1079–1092. https://doi.org/10.5194/CP-12-1079-2016

Sutanudjaja, E. H., van Beek, R., Wanders, N., Wada, Y., Bosmans, J. H. C., Drost, N., van der Ent, R. J., de Graaf, I. E. M., Hoch, J. M., de Jong, K., Karssenberg, D., López López, P., Peßenteiner, S., Schmitz, O., Straatsma, M. W., Vannametee, E., Wisser, D., & Bierkens, M. F. P. (2018). PCR-GLOBWB 2: a 5 arcmin global hydrological and water resources model. *Geoscientific Model Development*, *11*(6), 2429–2453. https://doi.org/10.5194/gmd-11-2429-2018

Tran, L. T., Larsen, F., Pham, N. Q., Christiansen, A. V., Tran, N., Vu, H. V., Tran, L. V., Hoang, H. V., & Hinsby, K. (2012). Origin and extent of fresh groundwater, salty paleowaters and recent saltwater intrusions in Red River flood plain aquifers, Vietnam. *Hydrogeology Journal*, *20*(7), 1295–1313. https://doi.org/10.1007/S10040-012-0874-Y/FIGURES/11

van Engelen, J., Bierkens, M. F. P., Delsman, J. R., & Oude Essink, G. H. P. (2021). Factors Determining the Natural Fresh-Salt Groundwater Distribution in Deltas. *Water Resources Research*, *57*(1), e2020WR027290. https://doi.org/10.1029/2020WR027290

van Engelen, J., Oude Essink, G. H. P., Kooi, H., & Bierkens, M. F. P. (2018). On the origins of hypersaline groundwater in the Nile Delta aquifer. *Journal of Hydrology*, *560*, 301–317. https://doi.org/10.1016/J.JHYDROL.2018.03.029

Van Engelen, J., Verkaik, J., King, J., Nofal, E. R., Bierkens, M. F. P., & Oude Essink, G. H. P. (2019). A three-dimensional palaeohydrogeological reconstruction of the groundwater salinity distribution in the Nile Delta Aquifer. *Hydrology and Earth System Sciences*, *23*(12), 5175–5198. https://doi.org/10.5194/HESS-23-5175-2019

Van Pham, H., Van Geer, F. C., Bui Tran, V., Dubelaar, W., & Oude Essink, G. H. P. (2019). Paleo-hydrogeological reconstruction of the fresh-saline groundwater distribution in the Vietnamese Mekong Delta since the late Pleistocene. *Journal of Hydrology: Regional Studies*, *23*, 100594. https://doi.org/10.1016/J.EJRH.2019.100594

Van Weert, F., Van Der Gun, J., & Reckman, J. (2009). *Global Overview of Saline Groundwater Occurrence and Genesis*.

Vandenbohede, A., Luyten, K., & Lebbe, L. (2008). Effects of Global Change on Heterogeneous Coastal Aquifers: A Case Study in Belgium. *Https://Doi.Org/10.2112/05-0447.1*, *24*(sp2), 160–170. https://doi.org/10.2112/05-0447.1

Vengosh, A., Kloppmann, W., Marei, A., Livshitz, Y., Gutierrez, A., Banna, M., Guerrot, C., Pankratov, I., & Raanan, H. (2005). Sources of salinity and boron in the Gaza strip: Natural contaminant flow in the southern Mediterranean coastal aquifer. *Water Resources Research*, *41*(1), 1–19. https://doi.org/10.1029/2004WR003344

Verkaik, J., van Engelen, J., Huizer, S., Bierkens, M. F. P., Lin, H. X., & Oude Essink, G. H. P. (2021). Distributed memory parallel computing of three-dimensional variable-density groundwater flow and salt transport. *Advances in Water Resources*, *154*, 103976. https://doi.org/10.1016/J.ADVWATRES.2021.103976

Verweij, J. M. (Johanna M. (2003). *Fluid flow systems analysis on geological timescales in onshore and offshore Netherlands : with special reference to the Broad Fourteens Basin*. Netherlands Institute of Applied Geoscience TNO.

Vincent, A., & Violette, S. (2017). Why seawater intrusion has not yet occurred in the Kaluvelli-Pondicherry basin, Tamil Nadu, India. *Hydrogeology Journal*, *25*(6), 1893–1907. https://doi.org/10.1007/S10040-017-1558-4/TABLES/3

Vineis, P., Chan, Q., & Khan, A. (2011). Climate change impacts on water salinity and health. *Journal of Epidemiology and Global Health*, *1*(1), 5–10. https://doi.org/10.1016/J.JEGH.2011.09.001

Weatherall, P., Marks, K. M., Jakobsson, M., Schmitt, T., Tani, S., Arndt, J. E., Rovere, M., Chayes, D., Ferrini, V., & Wigley, R. (2015). A new digital bathymetric model of the world's oceans. *Earth and Space Science*, *2*(8), 331–345. https://doi.org/https://doi.org/10.1002/2015EA000107

Weert, F. Van, … J. V. der G.-I., & 2009, undefined. (2009). Global overview of saline groundwater occurrence and genesis. *Indiaenvironmentportal.Org.In*. http://www.indiaenvironmentportal.org.in/files/salinegroundwater.pdf

Weinberger, G., Rosenthal, E., Ben-Zvi, A., & Zeitoun, D. G. (1994). The Yarkon-Taninim groundwater basin, Israel hydrogeology: case study and critical review. *Journal of Hydrology*, *161*(1), 227–255. https://doi.org/https://doi.org/10.1016/0022-1694(94)90130-9

Werner, A. D., Bakker, M., Post, V. E. A., Vandenbohede, A., Lu, C., Ataie-Ashtiani, B., Simmons, C. T., & Barry, D. A. (2013). Seawater intrusion processes, investigation and management: Recent advances and future challenges. *Advances in Water Resources*, *51*, 3–26. https://doi.org/10.1016/J.ADVWATRES.2012.03.004

World Bank. (2009). *Making the most of scarcity : accountability for better water management in the Middle East and North Africa (English)*. http://documents.worldbank.org/curated/en/101281468278679639/Making-the-most-of-scarcity-accountability-for-better-water-management-in-the-Middle-East-and-North-Africa

World Bank. (2016). *World Development Indicators | DataBank*. https://databank.worldbank.org/reports.aspx?source=2&Topic=1

Xiao, H., Tang, Y., Li, H., Zhang, L., Ngo-Duc, T., Chen, D., & Tang, Q. (2021). Saltwater intrusion into groundwater systems in the Mekong Delta and links to global change. *Advances in Climate Change Research*, *12*(3), 342–352. https://doi.org/10.1016/J.ACCRE.2021.04.005

Yangui, H., Zouari, K., Trabelsi, R., & Rozanski, K. (2011). Recharge mode and mineralization of groundwater in a semi-arid region: Sidi Bouzid plain (central Tunisia). *Environmental Earth Sciences*, *63*(5), 969–979. https://doi.org/10.1007/S12665-010-0771-4/FIGURES/9

Yechieli, Y., Kafri, U., Wollman, S., Shalev, E., & Lyakhovsky, V. (2009). The effect of base level changes and geological structures on the location of the groundwater divide, as exhibited in the hydrological system between the Dead Sea and the Mediterranean Sea. *Journal of Hydrology*, *378*(3–4), 218–229. https://doi.org/10.1016/J.JHYDROL.2009.09.023

Yechieli, Y., & Sivan, O. (2011). The distribution of saline groundwater and its relation to the hydraulic conditions of aquifers and aquitards: Examples from Israel. *Hydrogeology Journal*, *19*(1), 71–81. https://doi.org/10.1007/S10040-010-0646-5/TABLES/2

Yechieli, Y., & Wood, W. W. (2002). Hydrogeologic processes in saline systems: Playas, sabkhas, and saline lakes. *Earth-Science Reviews*, *58*(3–4), 343–365. https://doi.org/10.1016/S0012-8252(02)00067-3

Yechieli, Y., Yokochi, R., Zilberbrand, M., Lu, Z.-T., Purtschert, R., Sueltenfuss, J., Jiang, W., Zappala, J., Mueller, P., Bernier, R., Avrahamov, N., Adar, E., Talhami, F., Livshitz, Y., & Burg, A. (2019). Recent seawater intrusion into deep aquifer determined by the radioactive noble-gas isotopes 81Kr and 39Ar. *Earth and Planetary Science Letters*, *507*, 21–29. https://doi.org/10.1016/j.epsl.2018.11.028

Zamrsky, D. (2021). *Current and future state of groundwater in coastal unconsolidated sediment systems worldwide* [Utrecht University]. https://doi.org/10.33540/867

Zamrsky, D. (2023). *How to build a large scale 3D groundwater salinity model – "3333 clicks and 33 scripts to a groundwater model" – example Tunisia*.

Zamrsky, D., Essink, G. H. P. O., Sutanudjaja, E. H., van Beek, L. P. H., & Bierkens, M. F. P. (2022). Offshore fresh groundwater in coastal unconsolidated sediment systems as a potential fresh water source in the 21st century. *Environmental Research Letters*, *17*(1), 14021. https://doi.org/10.1088/1748-9326/ac4073

Zamrsky, D., Karssenberg, M. E., Cohen, K. M., Bierkens, M. F. P., & Oude Essink, G. H. P. (2020). Geological Heterogeneity of Coastal Unconsolidated Groundwater Systems Worldwide and Its Influence on Offshore Fresh Groundwater Occurrence. *Frontiers in Earth Science*, *7*, 339. https://doi.org/10.3389/FEART.2019.00339/BIBTEX

Zamrsky, D., Oude Essink, G. H. P., & Bierkens, M. F. P. (2018). Estimating the thickness of unconsolidated coastal aquifers along the global coastline. *Earth Syst. Sci. Data*, *10*(3), 1591–1603. https://doi.org/10.5194/essd-10-1591-2018

Zilberbrand, M., Rosenthal, E., & Weinberger, G. (2014). Natural tracers in Senonian–Eocene formations for detecting interconnection between aquifers. *Applied Geochemistry*, *47*, 157–169. https://doi.org/https://doi.org/10.1016/j.apgeochem.2014.05.022

7. Appendices

A.1 Observations of Groundwater Level and Quality

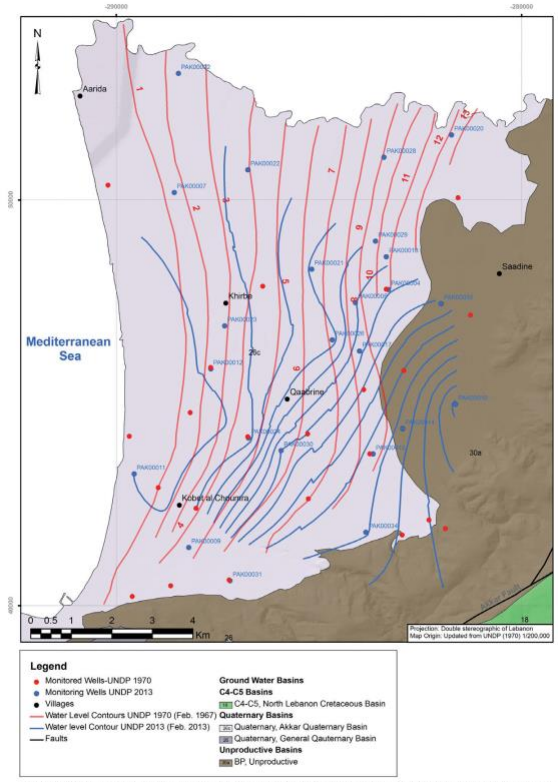

Figure 6-10 Groundwater table contour map for the Akkar Neogene-Quaternary Basin generated from February 2013 data set (blue) compared to February 1967 data sets (in Red), from UNDP 1970

(a)

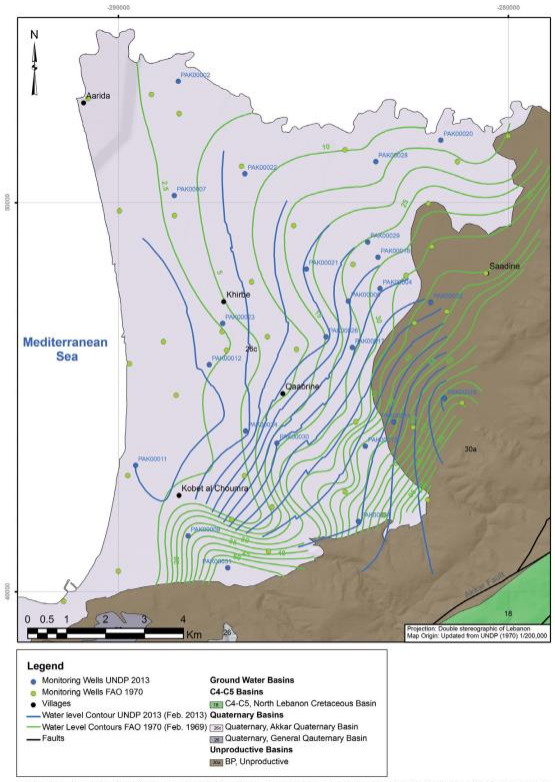

Figure 6-11 Groundwater table contour map in the Akkar Neogene-Quaternary Basin for February 2013 data set (Blue), compared to February 1969 data set (in green) obtained from FAO (1970)

(b)

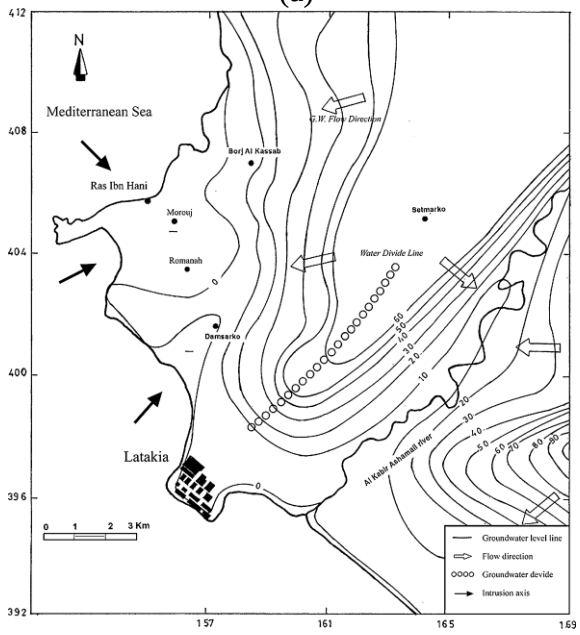

(c)

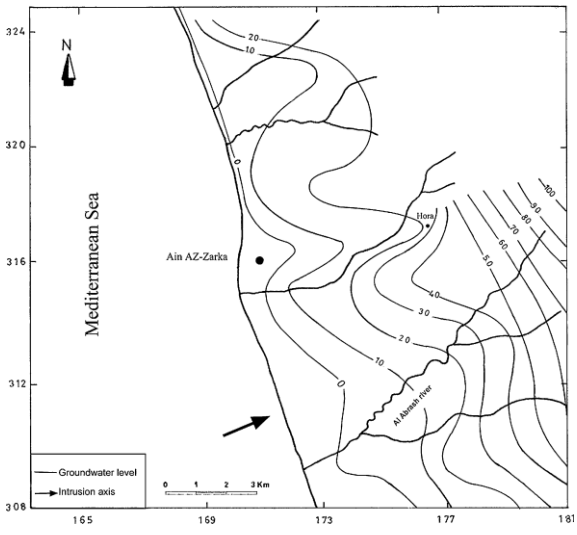

(d)

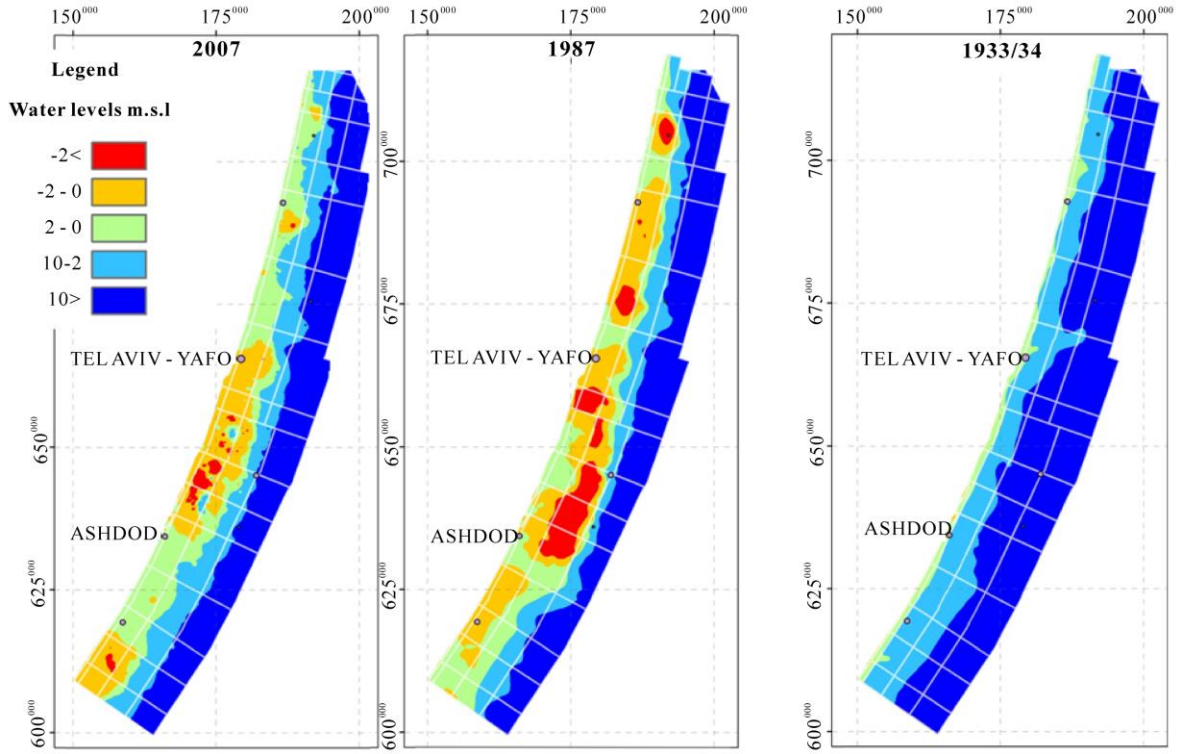

(e) (f) (g)

Figure S 1: Observation contour maps Quaternary Aquifer of the groundwater level (a), (b) Akkar in 1967 and 1969 (MoEW & UNDP, 2014), (c), (d) Latakia and Tartous in 1997 (Abou Zakhem & Hafez, 2007), (e), (f), (g) coast of Palestine and Israel (Livshitz et al., 2010)

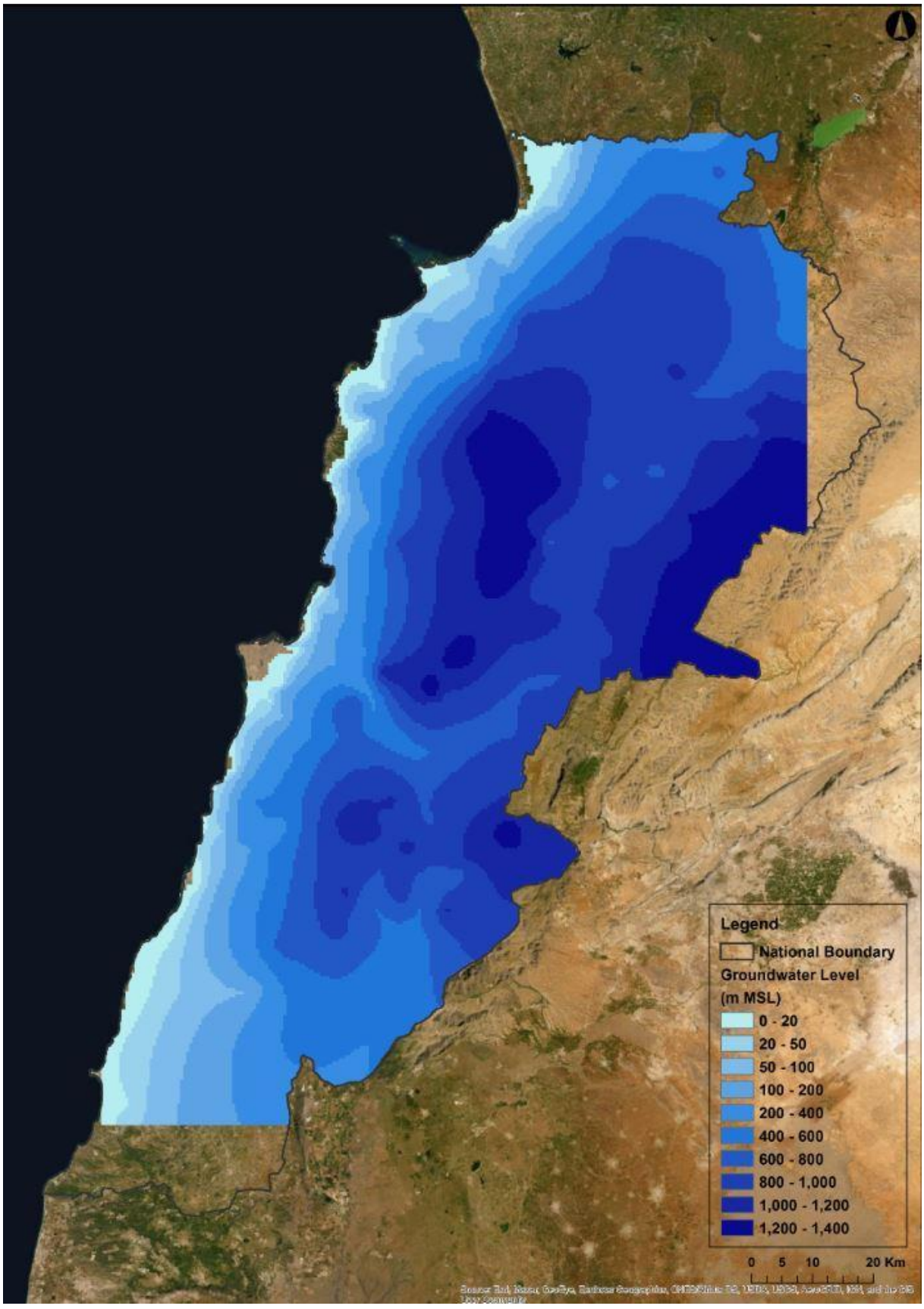

Figure S 2: Groundwater level of Lebanon (Frem & Saad, 2021)

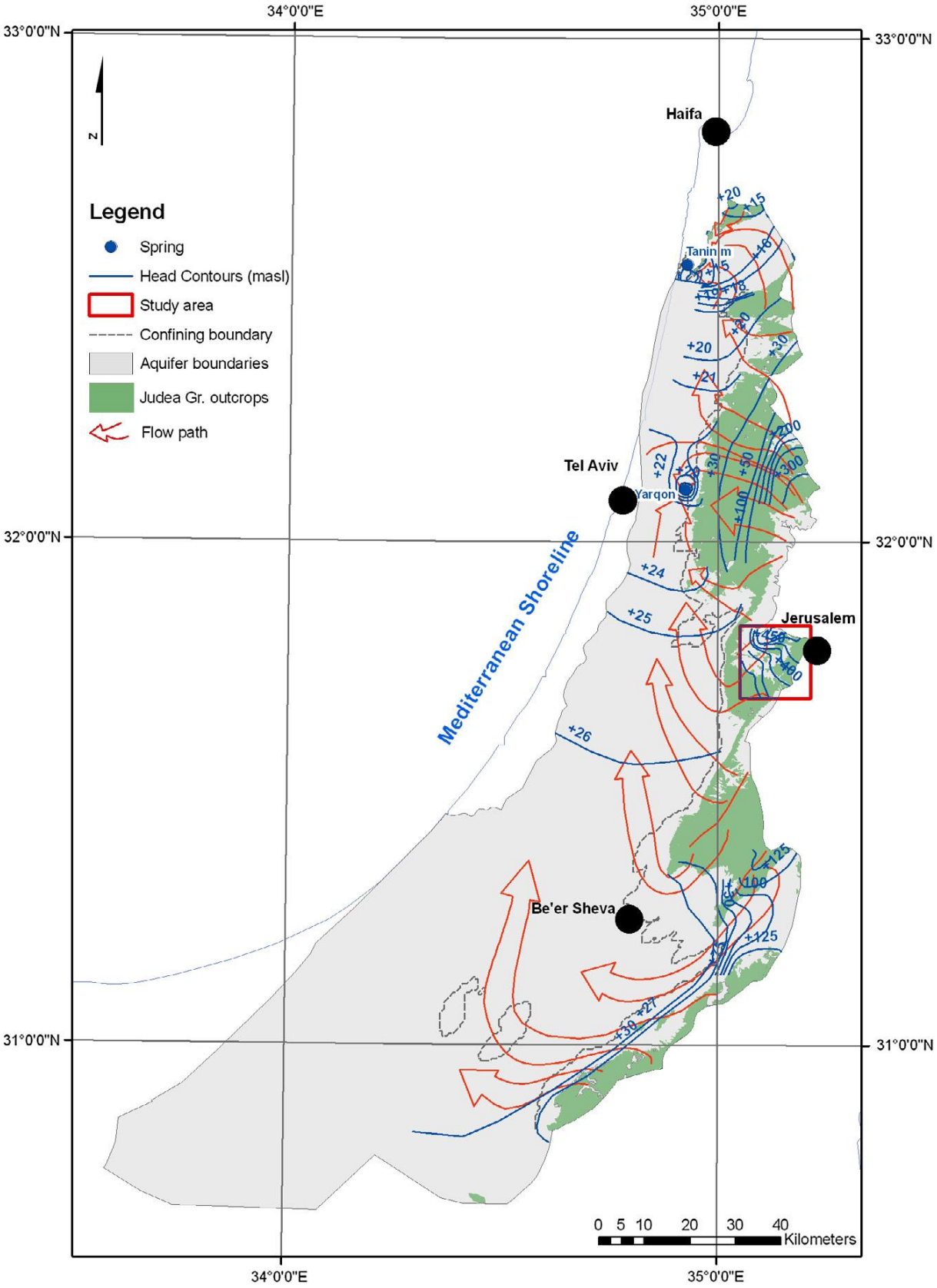

Figure S 3: Groundwater level of Cenomanian Aquifer of Palestine and Israel (Dvory et al., 2016)

A.2 Diverse

Table S 1: Summary of the global datasets used by Zamrsky et al. (2018) for aquifer thickness estimation

Dataset name	Description	Resolution	Reference
GEBCO 2014	Global topography and bathymetry	30 arcsec	(Weatherall et al., 2015)
Average soil and sedimentary deposit thickness	A gridded global dataset of soil, intact regolith, and sedimentary deposit thicknesses for regional and global land surface modelling; max. estimated depth is 50m.	30 arcsec	(Pelletier et al., 2016)
PCR-GLOBWB	Thickness of the groundwater layer from the global model (5 arcmin)	5 arcmin	(de Graaf et al., 2015)
GLIM	Global Lithological Map — Rock types of the Earth surface (16 basic classes), more than 1 200000 polygons	vector	(Hartmann and Moosdorf, 2012)
Natural Earth coastline	Global coastline	vector	(Natural-Earth, NA)

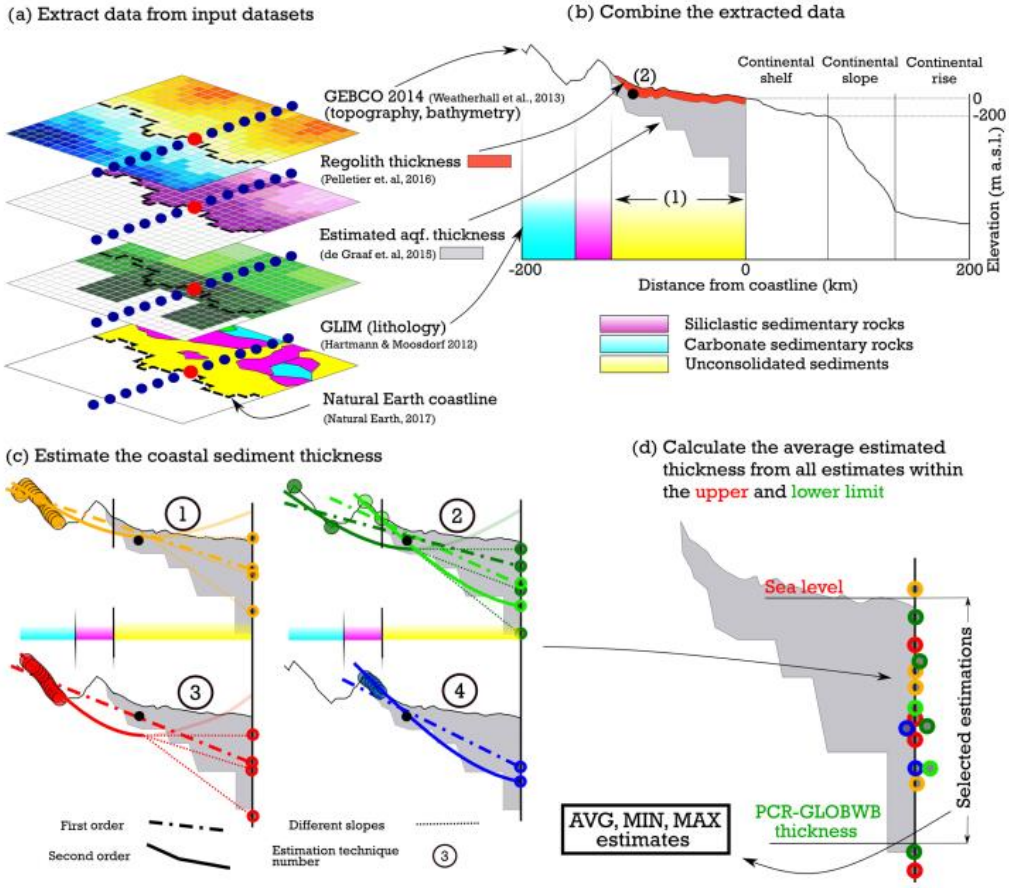

Figure 1. Schematization of the ATE method using available open-source global datasets. **(a)** Combining input datasets and extracting the values at cross-section points along a perpendicular cross section to the coastline running through a coastal point (red dot), only a few are schematized in the figure (in reality 800 per cross section). **(b)** Determine the extent of the coastal plain (1) and position of the anchor point (2). Extent of the cross section is set to 200 km landward and offshore; **(c)** the estimation is performed via topographical points selected based on the coastal plain extent, the position of the anchor points and the lithological classes from the GLIM dataset. The second-order estimation line is not used for estimation in case its minimum is reached before the coastline (transparent). **(d)** Final step of calculating the average, minimum and maximum estimated values.

Figure S 4: Cross sections schematization for estimation the aquifer thickness (after Zamrsky et al., 2018)

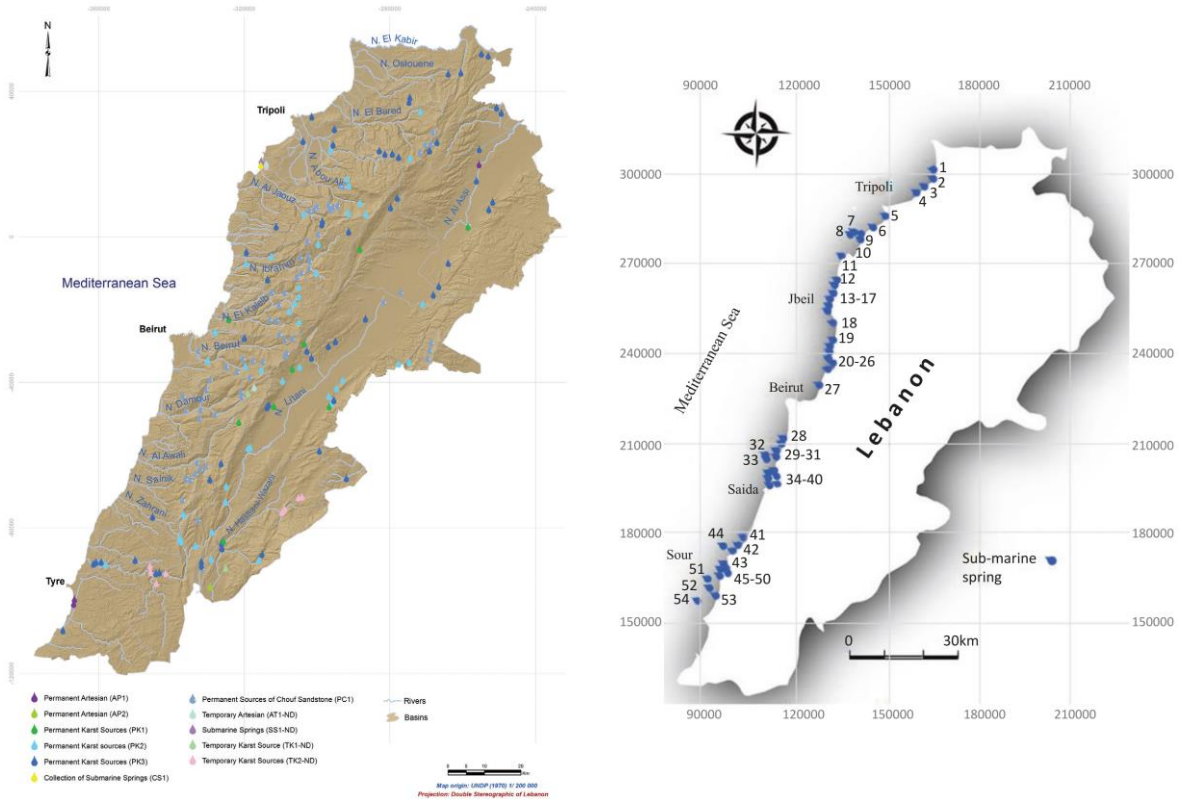

(a) (b)

Figure S 5: Location map of the (a) inland (MoEW & UNDP, 2014) and (b) submarine (Shaban, 2020) springs in Lebanon

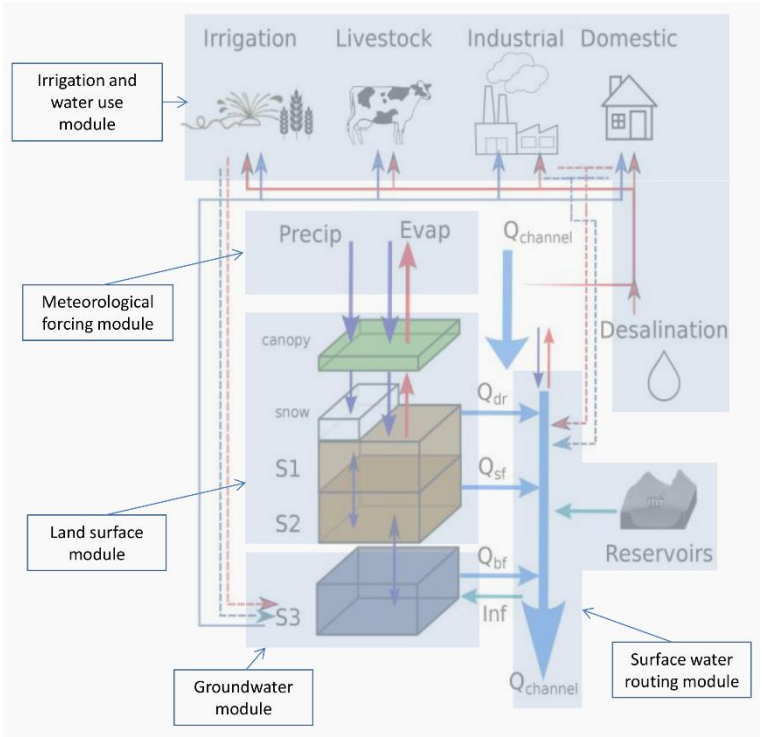

Figure S 6: Schemaization of PCR-GLOBWB cell (Sutanudjaja et al., 2018).

A.3 Lvnt 3: Model Layers Properties

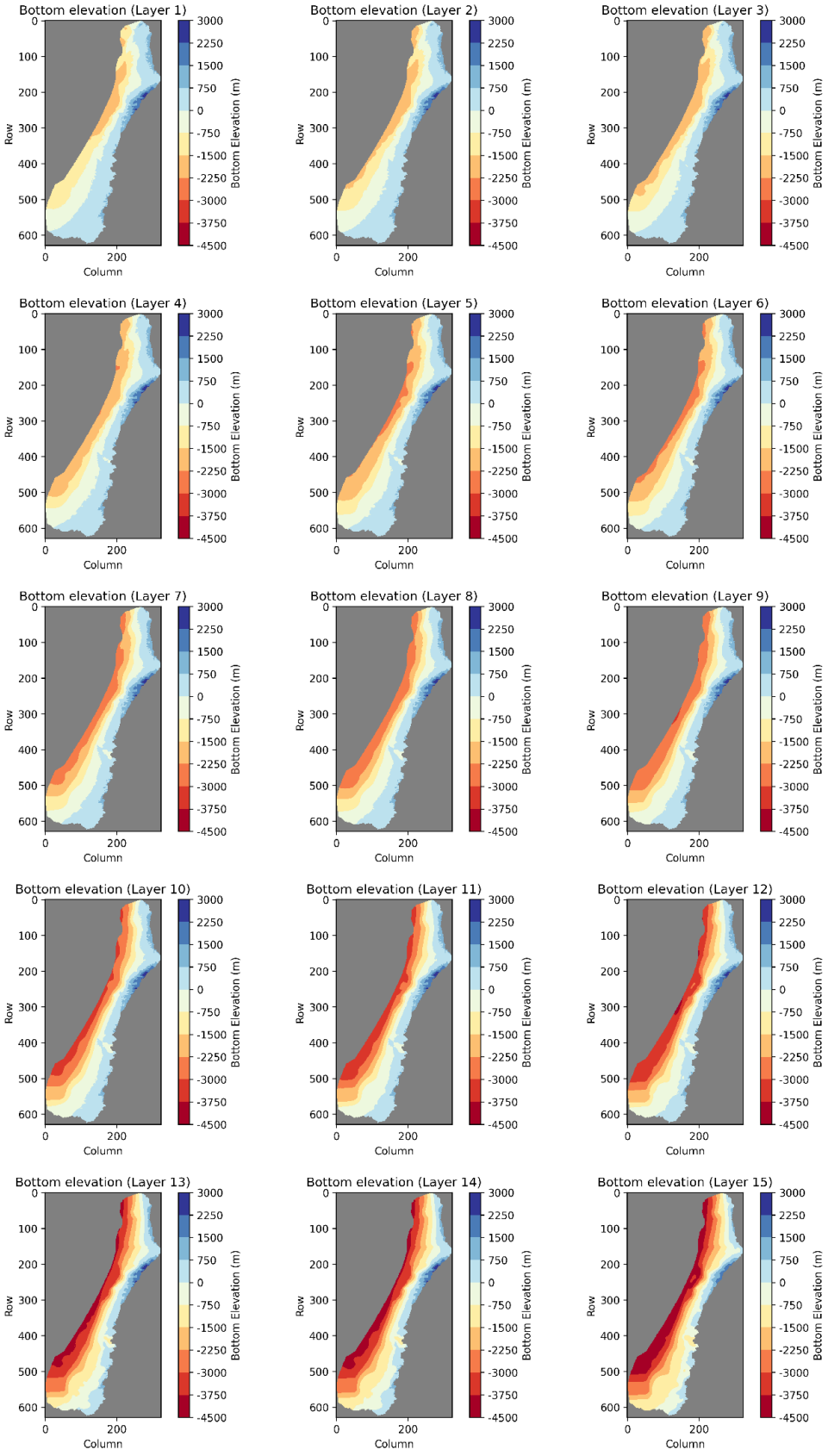

Figure S 7:Bottom elevation of Lvnt 3 layers

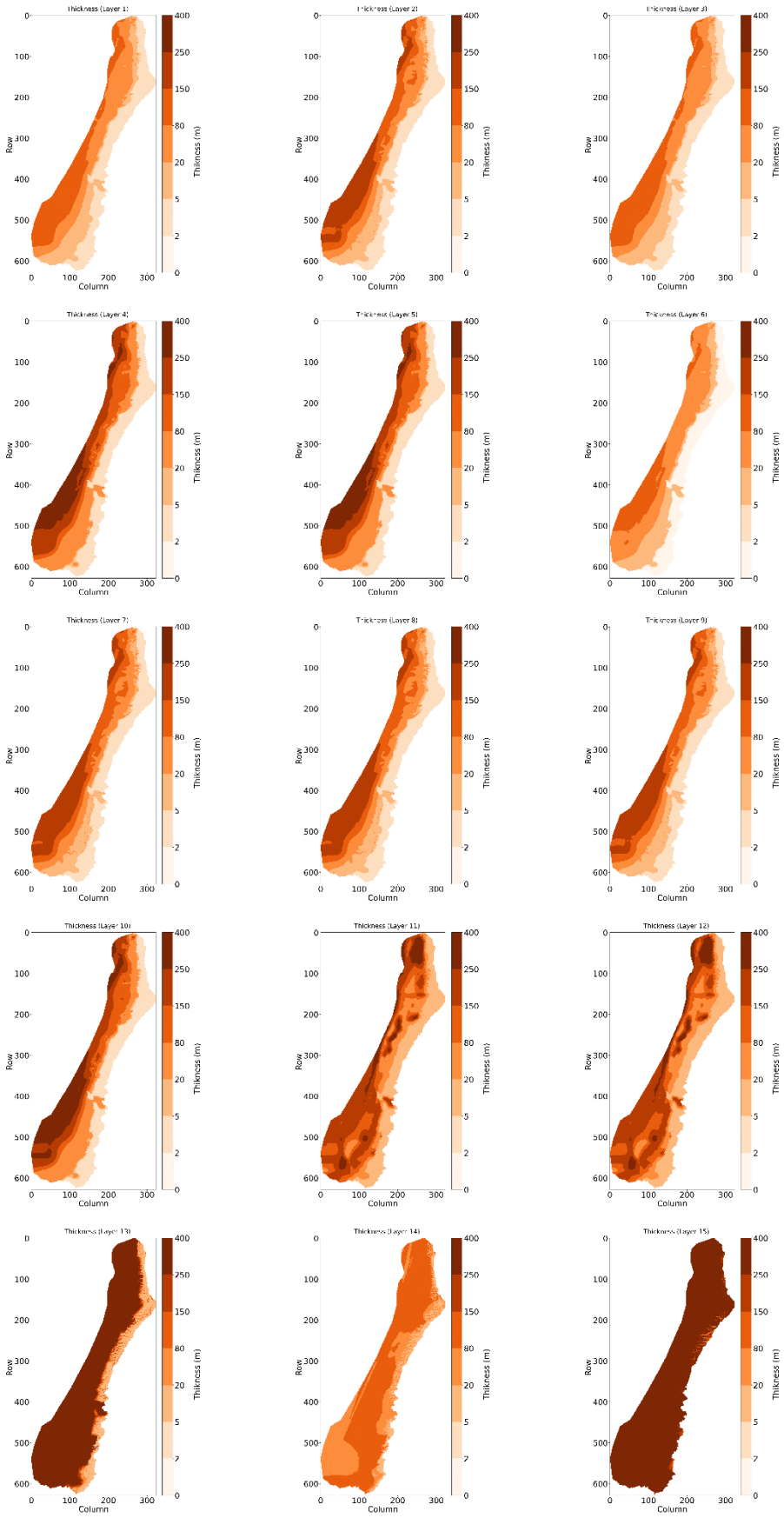

Figure S 8: Thickness of Lvnt 3 layers

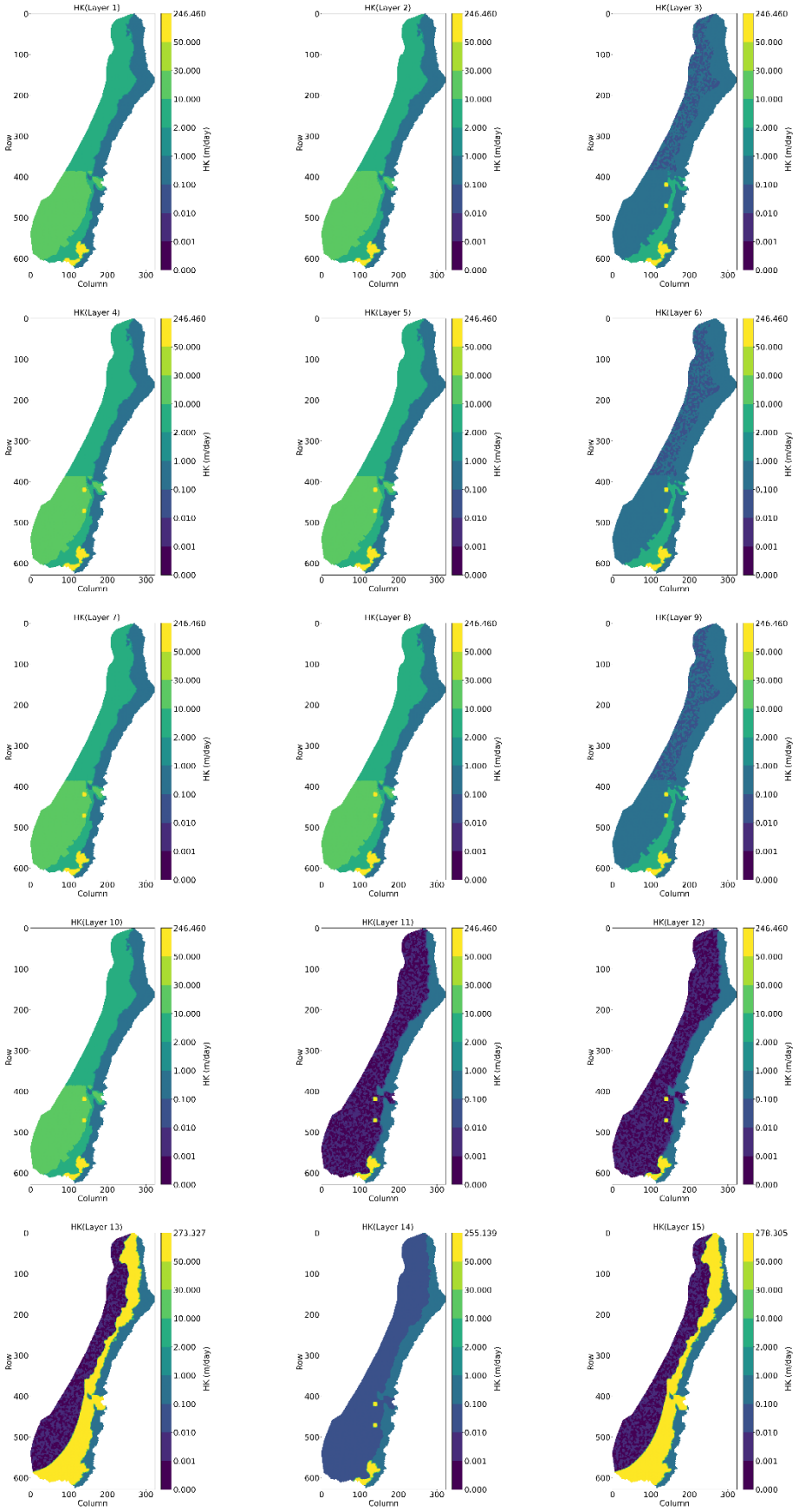

Figure S 9: Horizontal hydraulic conductivity of Lvnt 3 layers

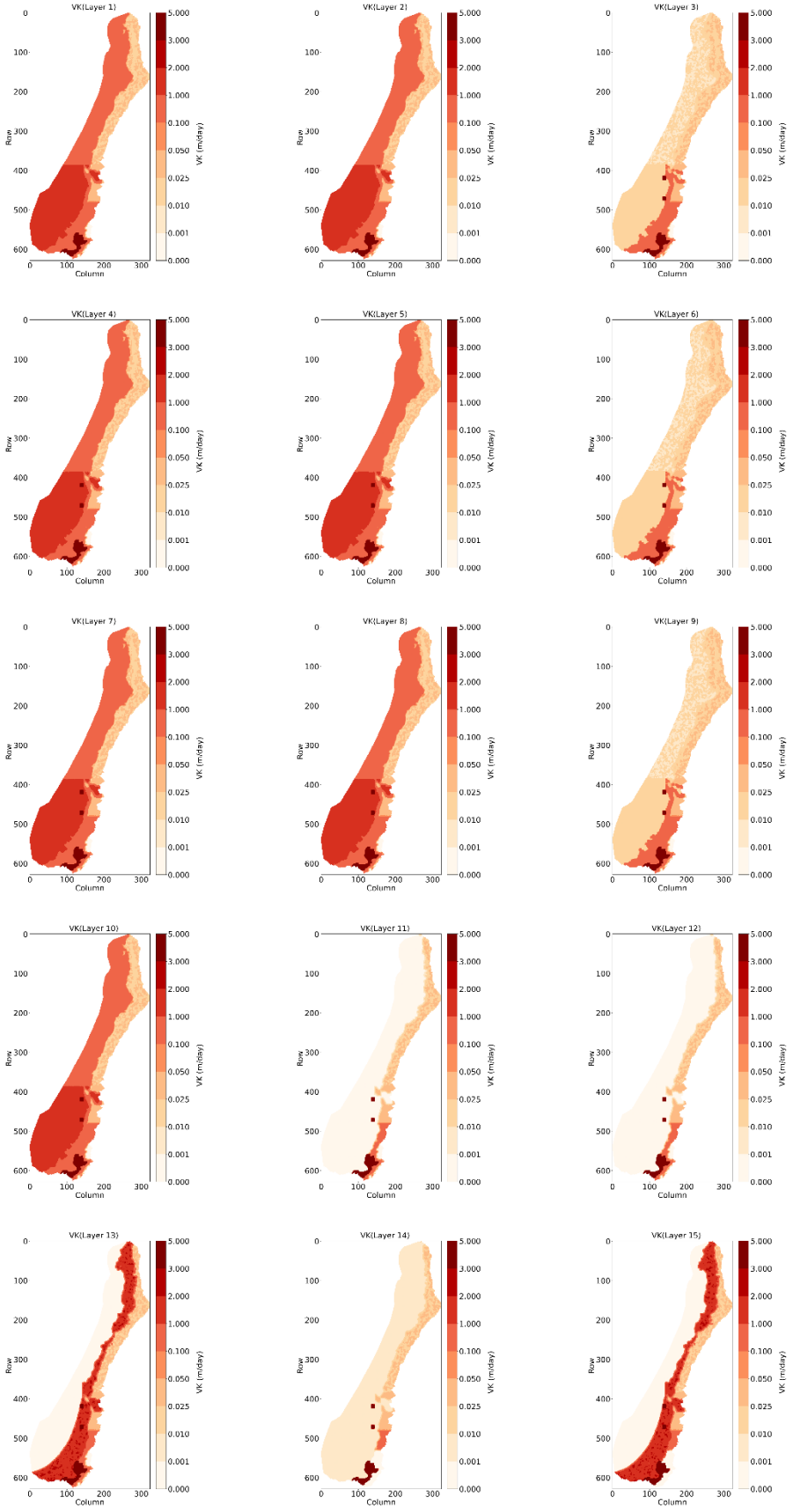

Figure S 10: Vertical hydraulic conductivity of Lvnt 3 layers

A.4 Lvnt 3: Results

Figure S 11: Water budget of Lvnt 3 throughout the paleo-reconstruction model and current status model

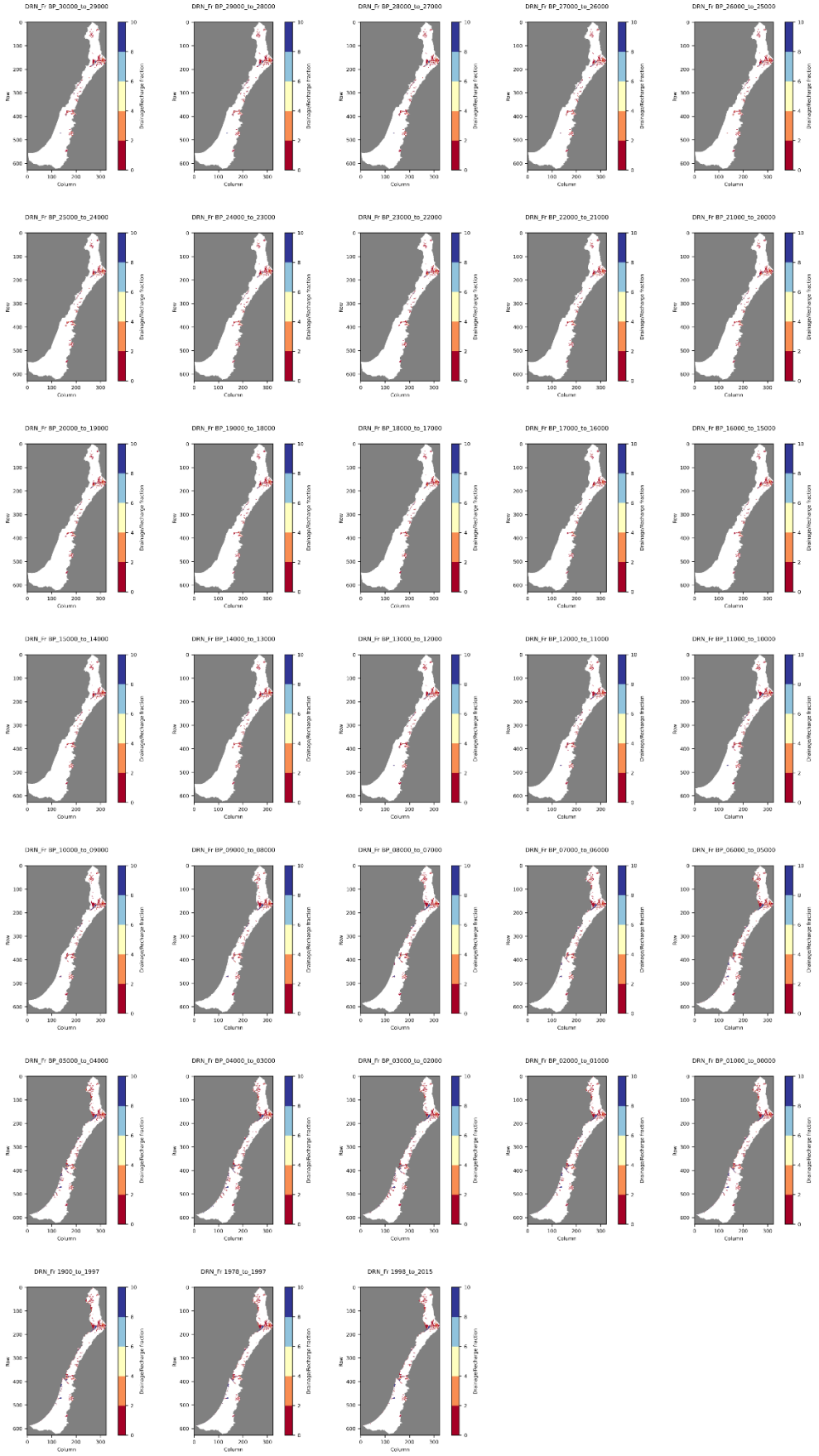

Figure S 12: Drainage/recharge fraction of Lvnt 3 (White color is zero)

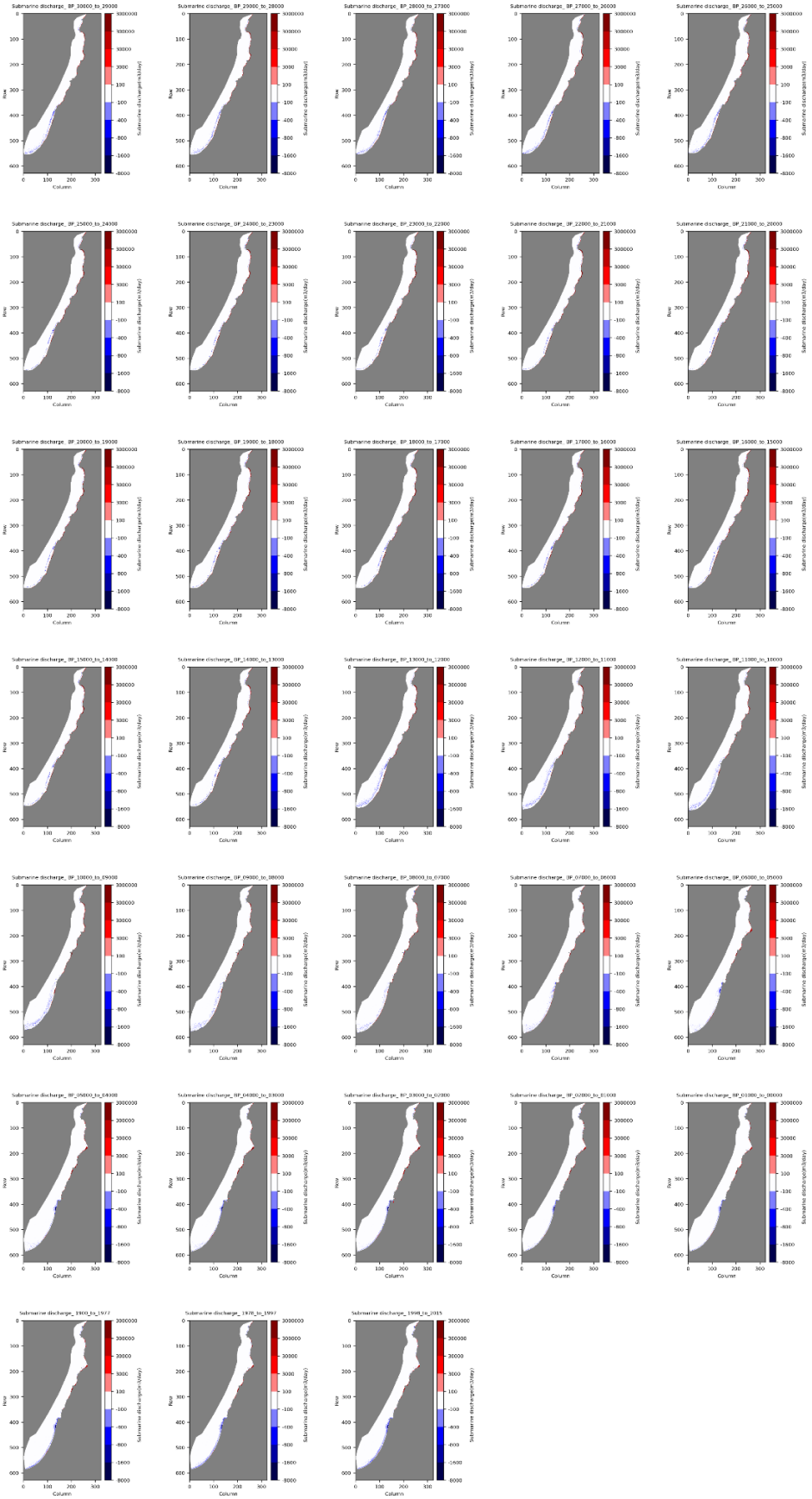

Figure S 13: Submarine groundwater discharge (m^3/day) of Lvnt 3 (positive value means out of the system flux and vice versa)

8. Annex: Observational and Modelled Data

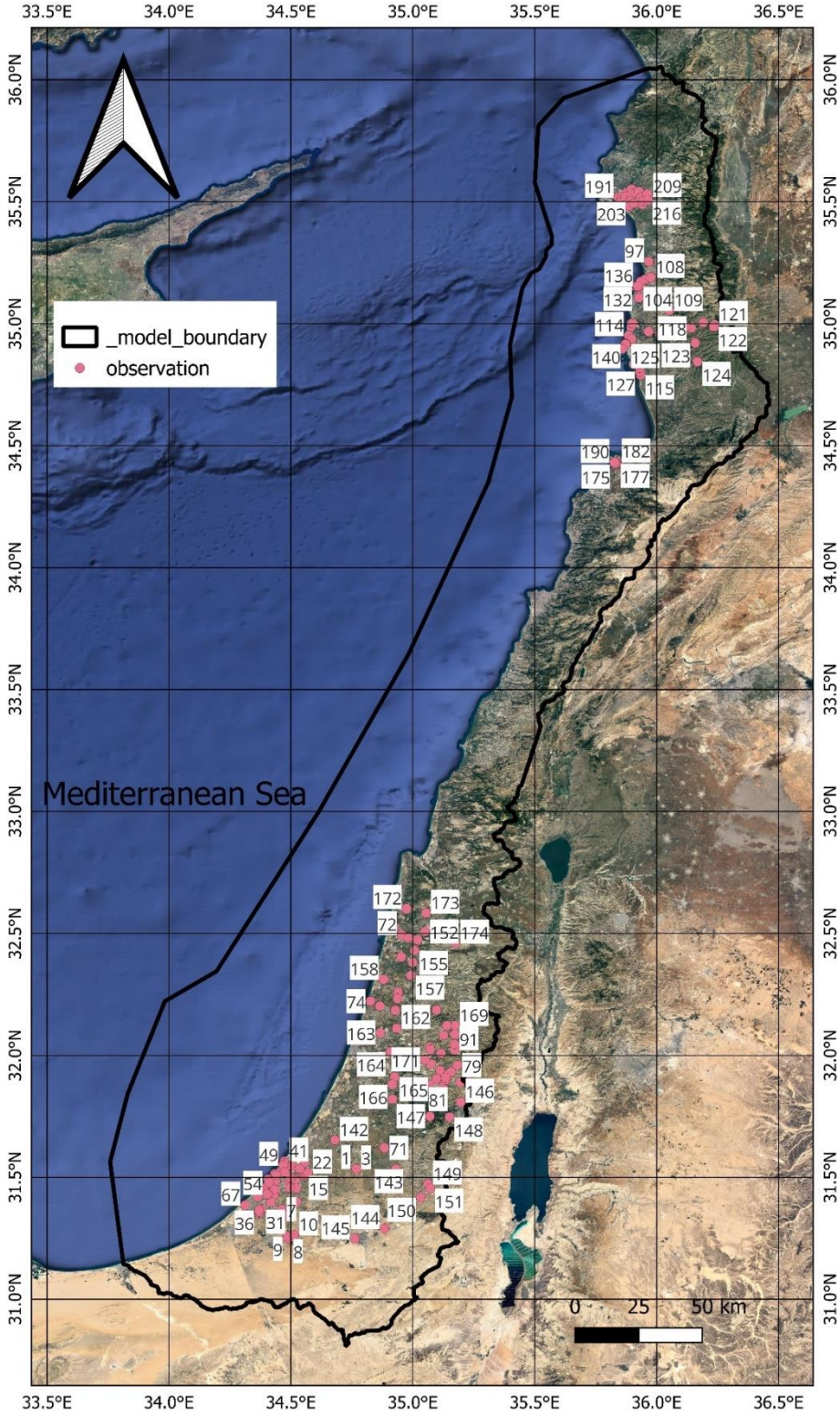

Figure S 14: Location map of the collected observation points that were used in the scatter chart in the scatter plot in the model calibration

Table 12: Observed data of groundwater level and TDS collected from published articles and modelled data

Sample No.	Date	X	Y	Z (msl	Aquifer	Observed TDS (g/l)	Modelled TDS (g/l) 1977			Observed Head (msl) 1977			Reference
							Lvnt 1	Lvnt 2	Lvnt 3	Lvnt 1	Lvnt 2	Lvnt 3	
1	1995-02-19	34.765	31.536			1.4	0.05	0.05	0.05	152.4	67.4	42.4	(Vengosh et al., 2005)
2	1995-02-19	34.769	31.535			1.3	0.05	0.05	0.05	158.7	68.5	42.6	
3	1994-07-26	34.769	31.535			1.3	0.05	0.05	0.05	158.7	68.5	42.6	
4	1999-07-07	34.463	31.369			1.8	0.05	0.05	0.05	44.0	40.0	20.3	
5	2001-08-16	34.463	31.369			1.8	0.05	0.05	0.05	44.0	40.0	20.3	
6	2001-08-16	34.463	31.369			1.9	0.05	0.05	0.05	44.0	40.0	20.3	
7	2001-08-16	34.463	31.369			1.6	0.05	0.05	0.05	44.0	40.0	20.3	
8	2001-08-16	34.49	31.248			1.9	0.05	0.05	0.05	101.2	69.7	33.9	
9	2001-08-16	34.486	31.258			2.3	0.05	0.05	0.05	97.8	68.3	33.2	
10	2001-08-16	34.514	31.264			4.4	0.05	0.05	0.05	104.2	72.0	35.2	
11	2001-10-09	34.477	31.346			4.6	0.05	0.05	0.05	56.8	48.5	24.6	
12	1999-07-07	34.508	31.497			2.9	0.05	0.05	0.05	36.9	28.1	16.4	
13	1999-07-07	34.518	31.49			3.4	0.05	0.05	0.05	42.2	31.7	18.1	
14	1999-07-14	34.492	31.482			3.3	0.05	0.05	0.05	34.7	27.7	15.4	
15	1999-09-07	34.553	31.506			1.6	0.05	0.05	0.05	50.9	35.5	21.3	
16	1999-07-07	34.499	31.49			3.4	0.05	0.05	0.05	32.9	26.0	14.8	
17	1999-08-24	34.492	31.482			3.6	0.05	0.05	0.05	34.7	27.7	15.4	
18	2001-08-16	34.518	31.49			3.3	0.05	0.05	0.05	42.2	31.7	18.1	
19	2001-09-05	34.553	31.506			1.7	0.05	0.05	0.05	50.9	35.5	21.3	
20	2001-09-05	34.555	31.513			1.1	0.05	0.05	0.05	48.5	34.1	20.8	
21	2001-09-05	34.562	31.514			1.0	0.05	0.05	0.05	51.8	35.9	21.9	
22	2001-09-05	34.57	31.518			1.1	0.05	0.05	0.05	52.3	36.3	22.6	
23	1999-06-02	34.522	31.454			2.9	0.05	0.05	0.05	49.4	37.9	20.5	
24	2001-09-10	34.522	31.454			2.9	0.05	0.05	0.05	49.4	37.9	20.5	
25	2001-09-05	34.496	31.457			4.5	0.05	0.05	0.05	39.5	32.5	17.3	
26	1998-06-25	34.432	31.429			3.4	0.05	0.05	0.05	21.9	21.8	11.7	
27	1999-08-23	34.369	31.353			2.0	0.05	0.05	0.05	26.4	24.9	11.9	
28	1999-08-17	34.432	31.429			3.6	0.05	0.05	0.05	21.9	21.8	11.7	
29	1998-06-24	34.418	31.398			1.7	0.05	0.05	0.05	27.2	26.0	13.3	
30	1999-07-07	34.369	31.353			2.0	0.05	0.05	0.05	26.4	24.9	11.9	
31	1999-08-17	34.379	31.369			4.2	0.05	0.05	0.05	24.3	23.4	11.5	
32	1998-06-01	34.369	31.365			3.4	0.05	0.05	0.05	24.5	23.4	11.3	
33	2001-11-06	34.432	31.429			3.3	0.05	0.05	0.05	21.9	21.8	11.7	
34	2001-11-06	34.369	31.353			1.9	0.05	0.05	0.05	26.4	24.9	11.9	
35	2001-10-18	34.369	31.359			2.4	0.05	0.05	0.05	24.5	23.4	11.3	
36	2001-11-06	34.369	31.365			3.2	0.05	0.05	0.05	24.5	23.4	11.3	
37	2001-09-05	34.524	31.4			4.1	0.05	0.05	0.05	62.1	49.1	25.7	
38	2001-09-10	34.418	31.398			1.8	0.05	0.05	0.05	27.2	26.0	13.3	
39	NaT	34.418	31.398			1.8	0.05	0.05	0.05	27.2	26.0	13.3	
40	2001-05-26	34.504	31.546			0.6	0.05	0.05	0.05	21.7	17.2	11.4	
41	2001-05-26	34.473	31.566			3.7	0.05	0.05	0.05	4.5	4.9	3.6	
42	2001-05-26	34.472	31.558			1.8	0.05	0.05	0.05	7.4	7.5	5.2	
43	2001-05-26	34.466	31.526			1.7	0.05	0.05	0.05	15.7	11.7	7.3	
44	2001-05-26	34.534	31.535			2.1	0.05	0.05	0.05	34.6	26.1	16.6	
45	2001-05-26	34.497	31.498			2.2	0.05	0.05	0.05	31.3	24.5	14.3	
46	2001-05-26	34.434	31.514			1.8	0.05	0.05	0.05	11.4	9.6	5.8	
47	2001-05-26	34.406	31.491			1.5	0.05	0.05	0.07	5.2	5.6	3.9	
48	2001-05-27	34.474	31.521			2.3	0.05	0.05	0.05	19.7	14.8	9.3	
49	2001-05-27	34.468	31.55			2.9	0.05	0.05	0.05	12.1	9.7	6.5	
50	2001-05-28	34.392	31.455			3.2	0.05	0.05	0.05	8.9	9.8	6.4	
51	2001-05-28	34.392	31.444			2.9	0.05	0.05	0.05	9.1	10.1	6.3	
52	2001-05-28	34.434	31.45			2.0	0.05	0.05	0.05	20.2	19.2	10.8	
53	2001-05-28	34.439	31.487			1.4	0.05	0.05	0.05	15.5	13.7	8.3	
54	2001-05-28	34.403	31.431			2.1	0.05	0.05	0.05	15.9	16.6	9.3	
55	2001-11-20	34.502	31.499			1.8	0.05	0.05	0.05	34.0	26.3	15.3	
56	2001-11-20	34.537	31.535			2.2	0.05	0.05	0.05	34.6	26.1	16.6	
57	2001-11-20	34.474	31.521			2.4	0.05	0.05	0.05	19.7	14.8	9.3	
58	2001-11-20	34.392	31.444			3.0	0.05	0.05	0.05	9.1	10.1	6.3	
59	2001-11-20	34.434	31.514			2.0	0.05	0.05	0.05	11.4	9.6	5.8	

60	2001-11-20	34.39	31.446			2.8	0.05	0.05	0.05	9.1	10.1	6.3	
61	2001-11-20	34.497	31.498			2.2	0.05	0.05	0.05	31.3	24.5	14.3	
62	2001-11-20	34.439	31.509			1.4	0.05	0.05	0.05	11.4	9.6	5.8	
63	2001-11-20	34.405	31.431			2.5	0.05	0.05	0.05	15.9	16.6	9.3	
64	2001-11-20	34.403	31.431			2.2	0.05	0.05	0.05	15.9	16.6	9.3	
65	2001-11-20	34.364	31.419			2.4	0.05	0.05	0.05	9.2	10.6	6.2	
66	2001-09-05	34.558	31.563			0.9	0.05	0.05	0.05	30.4	25.5	17.0	
67	2001-10-18	34.312	31.386			0.5	0.05	0.05	0.13	7.7	8.3	4.7	
68	2001-10-18	34.416	31.483			1.3	0.05	0.05	0.05	9.0	9.2	6.1	
69	2001-10-18	34.41	31.479			1.4	0.05	0.05	0.05	9.0	9.2	6.1	
70	1.12.2011	34.884	31.621	-170.0		14.0	0.05	0.05	0.05	183.7	66.9	37.7	(Burg & Gersman, 2016)
71	30.10.2014	34.884	31.621	-170.0		11.2	0.05	0.05	0.05	183.7	66.9	37.7	
72	2.6.14	34.954	32.494	-958.1		39.6	0.05	0.05	0.07	18.0	10.8	18.2	(Yechieli et al., 2019)
73	2.6.14	34.826	32.222	-810.0		26.3	0.05	0.05	0.07	7.1	6.2	24.8	
74	2.6.14	34.826	32.222	-1419.0		38.1	0.05	0.05	0.78	7.1	6.2	24.6	
75	15.11.15	34.953	32.404	-1051.0		33.0	0.05	0.05	0.07	18.4	14.3	22.8	
76	15.11.15	34.865	32.202	-1101.0		36.2	0.05	0.05	0.15	14.5	11.7	25.2	
77	15.11.15	34.924	32.524	-497.6		32.7	0.05	0.05	5.23	7.3	6.1	9.9	
78	2016-2017	35.195	31.89		UDCA	0.2	0.05	0.05	0.05	266.0	68.5	327.3	(Jebreen et al., 2018)
79	2016-2017	35.183	31.96			0.2	0.05	0.05	0.05	260.6	65.4	329.0	
80	2016-2017	35.069	31.879			0.3	0.05	0.05	0.05	218.2	62.2	35.0	
81	2016-2017	35.123	31.871			0.3	0.05	0.05	0.05	246.1	66.2	58.2	
82	2016-2017	35.112	31.938			0.2	0.05	0.05	0.05	233.9	62.7	35.1	
83	2016-2017	35.135	31.899			0.2	0.05	0.05	0.05	250.1	66.0	123.1	
84	2016-2017	35.126	32.082			0.3	0.05	0.05	0.05	220.4	57.3	248.6	
85	2016-2017	35.194	32.036			0.3	0.05	0.05	0.05	261.4	63.8	458.1	
86	2016-2017	35.147	31.924			0.2	0.05	0.05	0.05	250.9	65.4	161.7	
87	2016-2017	35.157	31.932			0.2	0.05	0.05	0.05	253.4	65.5	198.4	
88	2016-2017	35.135	31.909			0.2	0.05	0.05	0.05	248.5	65.4	124.0	
89	2016-2017	35.171	32.086			0.3	0.05	0.05	0.05	241.8	60.2	389.0	
90	2016-2017	35.097	31.904			0.2	0.05	0.05	0.05	229.0	63.0	35.0	
91	2016-2017	35.172	32.023			0.4	0.05	0.05	0.05	253.2	63.0	333.3	
92	2016-2017	35.171	32.045			0.2	0.05	0.05	0.05	249.4	62.0	376.3	
93	2016-2017	35.116	32.008			0.3	0.05	0.05	0.05	221.6	59.2	36.6	
94	2016-2017	35.07	32.034			0.2	0.05	0.05	0.05	187.8	53.7	31.7	
95	2016-2017	35.072	32.024			0.2	0.05	0.05	0.05	191.3	54.6	32.3	
96	2016-2017	35.074	31.965			0.3	0.05	0.05	0.05	203.0	58.0	33.7	
97	2002-2003	35.968	35.255	12.0		0.5	0.05	0.05	0.05	26.8	10.4	24.8	(Al-Charideh, 2004)
98	2002-2003	35.952	35.182	13.0		0.4	0.05	0.05	0.05	25.7	8.2	22.6	
99	2002-2003	35.931	35.167	13.0		0.4	0.05	0.05	0.05	9.1	5.1	9.1	
100	2002-2003	35.928	35.107	10.0		0.4	0.05	0.05	0.05	35.7	10.0	29.8	
101	2002-2003	35.934	35.165	24.0		0.3	0.05	0.05	0.05	18.5	6.8	17.0	
102	2002-2003	35.936	35.152	55.0		0.4	0.05	0.05	0.05	22.3	7.6	20.0	
103	2002-2003	35.927	35.146	50.0		0.4	0.05	0.05	0.05	18.7	6.6	16.8	
104	2002-2003	35.926	35.152	11.0		0.4	0.05	0.05	0.05	12.3	5.3	12.6	
105	2002-2003	35.896	34.989	29.0		0.4	0.05	0.05	0.05	11.1	5.8	15.5	
106	2002-2003	35.934	35.173	25.8		0.3	0.05	0.05	0.05	14.8	6.0	14.4	
107	2002-2003	35.934	35.173	25.7		0.3	0.05	0.05	0.05	14.8	6.0	14.4	
108	2002-2003	35.976	35.19	112.0		0.5	0.05	0.05	0.05	52.3	12.8	49.6	
109	2002-2003	36.052	35.054	185.0		0.4	0.05	0.05	0.05	154.6	28.5	67.7	
110	2002-2003	35.967	34.968	71.0		0.5	0.05	0.05	0.05	85.6	18.2	142.7	
111	2002-2003	36.013	34.957	144.0		1.1	0.05	0.05	0.05	121.0	24.2	207.5	
112	2002-2003	35.898	35.001	25.0		0.4	0.28	0.05	0.05	2.2	2.1	2.6	
113	2002-2003	35.903	35.001	11.0		0.3	0.05	0.05	0.05	12.4	5.8	16.0	
114	2002-2003	35.885	34.951	5.0		0.7	0.05	0.05	0.05	7.3	4.5	11.2	
115	2002-2003	35.935	34.79	7.0		0.4	0.05	0.05	0.05	10.0	6.0	12.0	
116	2002-2003	35.893	34.929	30.0		0.4	0.05	0.05	0.05	12.2	6.3	18.5	
117	2002-2003	35.897	34.938	15.0		0.4	0.05	0.05	0.05	12.1	6.2	18.1	
118	2002-2003	36.142	34.982	343.0		0.5	0.05	0.05	0.05	211.9	38.7	119.6	
119	2002-2003	36.121	34.987	433.0		0.4	0.05	0.05	0.05	199.4	36.6	69.4	
120	2002-2003	36.191	35.004	568.0		0.4	0.05	0.05	0.05	230.7	41.3	355.2	
121	2002-2003	36.237	34.997	790.0		0.4	0.05	0.05	0.05	245.2	44.0	596.1	
122	2002-2003	36.234	34.988	569.0		0.4	0.05	0.05	0.05	245.2	44.1	595.6	

123	2002-2003	36.158	34.922	328.0		0.6	0.05	0.05	0.05	209.7	40.1	231.7	
124	2002-2003	36.168	34.844	424.0		0.4	0.05	0.05	0.05	197.1	41.6	260.6	
125	2002-2003	35.875	34.917	0.5		0.6	1.06	0.05	0.05	2.1	2.1	2.3	
126	2002-2003	35.906	34.834	10.0		0.4	0.05	0.05	0.05	6.1	4.3	9.0	
127	2002-2003	35.931	34.804	12.0		0.4	0.05	0.05	0.05	9.7	5.8	12.1	
128	2002-2003	35.931	34.819	10.0		0.5	0.05	0.05	0.05	13.5	7.3	20.8	
129	2002-2003	35.921	34.831	14.2		0.4	0.05	0.05	0.05	11.5	6.6	18.5	
130	2002-2003	35.911	35.153	-37.0		1.9	4.45	4.77	3.08	1.2	1.0	1.3	
131	2002-2003	35.918	35.153	-14.0		15.6	1.94	0.05	0.09	0.7	0.3	0.7	
132	2002-2003	35.919	35.152	-10.0		22.9	1.94	0.05	0.09	0.7	0.3	0.7	
133	2002-2003	35.922	35.152	-10.0		38.9	1.94	0.05	0.09	0.7	0.3	0.7	
134	2002-2003	35.923	35.153	-7.0		35.3	1.77	0.05	0.09	0.4	0.3	0.7	
135	2002-2003	35.923	35.153	-7.0		30.1	1.77	0.05	0.09	0.4	0.3	0.7	
136	2002-2003	35.923	35.154	-5.0		5.0	1.77	0.05	0.09	0.4	0.3	0.7	
137	2002-2003	35.859	34.898	-14.0		27.8	1.25	5.22	4.93	1.1	0.8	1.2	
138	2002-2003	35.859	34.897	-10.0		4.9	1.25	5.22	4.93	1.1	0.8	1.2	
139	2002-2003	35.86	34.903	-15.0		8.4	6.82	4.30	3.05	0.3	0.2	0.3	
140	2002-2003	35.873	34.916	-2.0		24.1	1.06	0.05	0.05	2.1	2.1	2.3	
141	2002-2003	35.859	34.897	-12.0		25.1	1.25	5.22	4.93	1.1	0.8	1.2	
142	1965	34.681	31.652				0.05	0.05	0.05	58.0	33.2	36.6	(Abusaada, 2011)
143	1965	34.931	31.534		UDCA		0.05	0.05	0.05	266.7	87.1	38.9	
144	1965	34.884	31.29				0.05	0.05	0.05	323.7	123.5	39.5	
145	1965	34.762	31.248				0.05	0.05	0.05	239.8	116.0	38.8	
146	1965	35.196	31.808				0.05	0.05	0.05	270.8	71.1	398.6	
147	1965	35.07	31.75		LDCA		0.05	0.05	0.05	238.1	69.1	41.5	
148	1965	35.151	31.747				0.05	0.05	0.05	266.4	72.5	403.4	
149	1965	35.063	31.472		UDCA		0.05	0.05	0.05	359.2	108.0	666.8	
150	1965	35.032	31.418				0.05	0.05	0.05	367.6	114.1	451.9	
151	1965	35.071	31.454		LDCA		0.05	0.05	0.05	366.8	110.6	400.5	
152	1965	35.05	32.508				0.05	0.05	0.05	49.6	22.0	20.6	
153	1965	34.982	32.484				0.05	0.05	0.05	25.9	14.3	19.2	
154	1965	35.02	32.474				0.05	0.05	0.05	39.0	20.0	20.5	
155	1965	35.007	32.43				0.05	0.05	0.05	27.1	19.9	21.4	
156	1965	35	32.381				0.05	0.05	0.05	31.0	21.2	22.5	
157	1965	34.992	32.328				0.05	0.05	0.05	32.9	23.0	23.5	
158	1965	34.88	32.312				0.05	0.05	0.07	11.5	8.6	23.6	
159	1965	34.94	32.258		UDCA		0.05	0.05	0.05	34.6	20.7	24.5	
160	1965	34.938	32.233				0.05	0.05	0.05	38.6	22.2	24.8	
161	1965	34.928	32.184				0.05	0.05	0.05	33.9	22.9	25.1	
162	1965	34.934	32.111				0.05	0.05	0.05	30.0	27.3	25.5	
163	1965	34.867	32.093				0.05	0.05	0.05	16.9	15.1	26.3	
164	1965	34.908	32.014				0.05	0.05	0.05	41.3	31.6	29.7	
165	1965	34.925	31.911				0.05	0.05	0.05	86.6	43.3	33.0	
166	1965	34.916	31.881				0.05	0.05	0.05	95.4	43.3	33.6	
167	1965	34.917	31.821				0.05	0.05	0.05	116.2	47.6	34.8	
168	1965	35.097	32.187				0.05	0.05	0.05	165.0	47.2	48.1	
169	1965	35.173	32.122		LDCA		0.05	0.05	0.05	234.1	58.4	377.7	
170	1965	35.139	32.122				0.05	0.05	0.05	215.3	55.7	274.4	
171	1965	35.05	31.983				0.05	0.05	0.05	180.2	54.4	32.7	
172	1965	34.974	32.602		UDCA		0.05	0.05	0.08	14.3	8.3	17.2	
173	1965	35.054	32.584				0.05	0.05	0.05	38.3	17.7	20.4	
174	1965	35.175	32.46				0.05	0.05	0.05	105.4	37.6	28.4	
175	2020-06-23	35.829	34.424			0.63717	0.05	0.05	0.05	11.2	4.1	12.1	(Halwani et al., 2022)
176	2020-06-23	35.831	34.425			1.1124	0.05	0.05	0.05	7.1	3.5	7.3	
177	2020-06-23	35.833	34.427			1.3843	0.05	0.05	0.05	7.1	3.5	7.3	
178	2020-06-23	35.832	34.43			0.79522	0.05	0.05	0.05	7.1	3.5	7.3	
179	2020-06-23	35.835	34.43			0.70216	0.05	0.05	0.05	14.4	4.8	14.6	
180	2020-06-23	35.833	34.432			0.78725	0.05	0.05	0.05	7.1	3.5	7.3	
181	2020-06-23	35.832	34.433			1.10684	0.05	0.05	0.05	7.1	3.5	7.3	
182	2020-06-23	35.836	34.434			0.5963	0.05	0.05	0.05	10.9	4.0	11.9	
183	2020-06-23	35.834	34.435			0.65459	0.05	0.05	0.05	10.9	4.0	11.9	
184	2020-06-23	35.834	34.435			0.65057	0.05	0.05	0.05	10.9	4.0	11.9	
185	2020-06-23	35.83	34.43			1.1834	0.05	0.05	0.05	7.1	3.5	7.3	

186	2020-06-23	35.83	34.432			0.60568	0.05	0.05	0.05	7.1	3.5	7.3	
187	2020-06-23	35.828	34.427			2.4858	0.05	0.05	0.05	7.1	3.5	7.3	
188	2020-06-23	35.829	34.434			1.11488	0.05	0.05	0.05	6.4	3.1	7.8	
189	2020-06-23	35.831	34.427			0.73767	0.05	0.05	0.05	7.1	3.5	7.3	
190	2020-06-23	35.827	34.432			1.09277	0.05	0.05	0.05	7.1	3.5	7.3	
191	2012	35.843	35.519	8.0			0.05	0.05	0.05	8.6	7.9	12.9	(Kinan, 2015)
192	2012	35.857	35.522	5.0			0.05	0.05	0.05	10.0	8.7	16.7	
193	2012	35.88	35.539	13.0			0.05	0.05	0.05	16.6	11.8	21.2	
194	2012	35.896	35.552	16.0			0.05	0.05	0.05	23.0	14.7	27.1	
195	2012	35.854	35.506	-8.0			0.05	0.05	0.05	9.1	7.3	16.3	
196	2012	35.853	35.496	4.0			0.05	0.05	0.05	7.7	6.3	14.3	
197	2012	35.878	35.514	2.0			0.05	0.05	0.05	17.7	10.5	25.6	
198	2012	35.872	35.522	-4.0			0.05	0.05	0.05	14.8	10.2	22.0	
199	2012	35.895	35.514	9.0			0.05	0.05	0.05	24.0	12.1	31.5	
200	2012	35.9	35.533	30.0			0.05	0.05	0.05	30.6	14.0	36.0	
201	2012	35.915	35.534	4.0			0.05	0.05	0.05	36.0	15.5	39.8	
202	2012	35.927	35.543	38.0			0.05	0.05	0.05	46.7	18.0	51.2	
203	2012	35.892	35.503	13.0			0.05	0.05	0.05	23.1	11.5	30.5	
204	2012	35.918	35.501	-11.0			0.05	0.05	0.05	36.4	14.3	40.9	
205	2012	35.925	35.508	-49.0			0.05	0.05	0.05	36.4	14.3	40.7	
206	2012	35.933	35.516	-45.0			0.05	0.05	0.05	48.1	16.6	52.8	
207	2012	35.944	35.524	-41.0			0.05	0.05	0.05	55.9	18.2	61.5	
208	2012	35.956	35.524	-46.0			0.05	0.05	0.05	61.8	19.3	67.4	
209	2012	35.966	35.521	-74.0			0.05	0.05	0.05	67.9	20.3	70.9	
210	2012	35.962	35.532	83.0			0.05	0.05	0.05	69.6	20.9	78.7	
211	2012	35.883	35.477	-3.0			0.05	0.05	0.05	13.5	8.2	20.0	
212	2012	35.887	35.485	2.0			0.05	0.05	0.05	15.9	9.2	23.0	
213	2012	35.905	35.493	3.0			0.05	0.05	0.05	25.3	11.8	30.8	
214	2012	35.942	35.49	25.0			0.05	0.05	0.05	42.9	15.7	45.4	
215	2012	35.946	35.503	-19.0			0.05	0.05	0.05	49.9	17.2	52.8	
216	2012	35.964	35.506	10.0			0.05	0.05	0.05	62.9	19.3	68.2	

LDCA: Lower Deep Cretaceous Aquifer
UDCA: Upper Deep Cretaceous Aquifer